

# In silico discovery of representational relationships across visual cortex

Alessandro T. Gifford<sup>1,2,3,\*</sup> , Maya A. Jastrzębowska<sup>1</sup> ,  
Johannes J.D. Singer<sup>1</sup> , Radosław M. Cichy<sup>1,2,3,4</sup> 

<sup>1</sup> Freie Universität Berlin, Berlin, Germany

<sup>2</sup> Einstein Center for Neurosciences Berlin, Berlin, Germany

<sup>3</sup> Bernstein Center for Computational Neuroscience Berlin, Berlin, Germany

<sup>4</sup> Berlin School of Mind and Brain, Berlin, Germany

\* Correspondence: [alessandro.gifford@gmail.com](mailto:alessandro.gifford@gmail.com)

**Now published in *Nature Human Behavior***  
**doi: <https://doi.org/10.1038/s41562-025-02252-z>**

Human vision is mediated by a complex interconnected network of cortical brain areas that jointly represent visual information. While these areas are increasingly understood in isolation, their representational relationships remain elusive. Here we developed relational neural control (RNC), and used it to investigate the representational relationships for univariate and multivariate fMRI responses of areas across visual cortex. Through RNC we generated and explored in silico fMRI responses for large amounts of images, discovering controlling images that align or disentangle responses across areas, thus indicating their shared or unique representational content. This revealed a typical network-level configuration of representational relationships in which shared or unique representational content varied based on cortical distance, categorical selectivity, and position within the visual hierarchy. Closing the empirical cycle, we validated the in silico discoveries on in vivo fMRI responses from independent subjects. Together, this reveals how visual areas jointly represent the world as an interconnected network.

# Introduction

Human vision is mediated by a complex interconnected network of cortical areas that jointly represent visual information<sup>1–9</sup>. The network consists of hierarchies and loops, with each area distinctly responding to visual properties of incoming visual stimuli, resulting in idiosyncratic representations of visual phenomena<sup>10–14</sup>.

Over the last half century, taking an atomistic approach, neuroscientists have studied visual representations by characterizing each area in isolation of other areas in a hypothesis-driven fashion using small, limited sets of stimuli carefully chosen by the experimenter. Seminal work in this spirit built the foundations of modern vision neuroscience, from characterizing the role of primary visual cortex for processing of oriented edges<sup>15</sup> to the role of higher-level visual cortex for processing of complex visual categories such as faces, places and objects<sup>16</sup>.

However, assessing areas one by one does not capture the visual system as an interconnected network; it does not assess representational relationships between areas and thus remains silent about what representational content is shared between areas or unique to a specific area. While anatomical<sup>2</sup> and functional<sup>17</sup> connectivity research assess the visual system at the network level, they miss what representational content the network encodes. Compounding the situation, theories of visual representations are based on sparse neural data for small sets of experimenter-picked stimuli, risking to reproduce experimenter biases while missing important neural signals that would be available from broad sampling.

Here, we addressed these challenges by developing relational neural control (RNC), and used it to reveal representational relationships between early-, mid-, and high-level visual areas across the human visual cortical network (i.e., V1, V2, V3, V4, EBA, FFA, PPA, RSC). First, through deep-neural-network-based encoding models<sup>18–20</sup>, RNC generated these areas' in silico fMRI responses for a larger set of naturalistic images than are available in vivo. This in turn enabled the evaluation of a larger, more diverse and thus less biased hypothesis space. Next, to uncover representational relationships, RNC selected controlling images aligning or disentangling the areas' in silico fMRI responses at both their univariate (i.e., voxel average)<sup>16,21–23</sup> and multivariate (i.e., voxel population pattern)<sup>21,22,24–26</sup> response level, under the assumption that alignment or disentanglement are indicative of shared or unique representational content, respectively. Finally, we validated our in silico findings in vivo through new experiments on independent subjects, thus closing the empirical cycle and validating RNC as a powerful exploratory neural control method to investigate representational relationships.

# Results

RNC provides accurate and denoised in silico fMRI responses for thousands of images

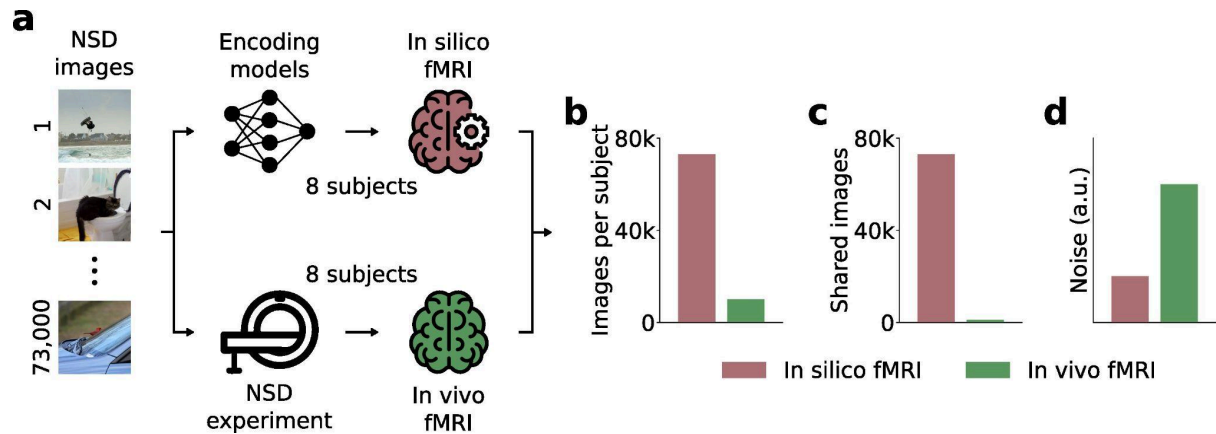


**Fig. 1 | RNC provides accurate and denoised in silico fMRI responses for thousands of images.** **a**, Through encoding models, we generated in silico fMRI responses to each of the 73,000 images and for each of the 8 subjects in the natural scenes dataset (NSD). We then compared these in silico responses with the in vivo fMRI responses from the NSD. **b**, Comparison of the number of image conditions presented to each subject, for the in silico and in vivo fMRI responses. **c**, Comparison of the number of image conditions shared across subjects, for the in silico and in vivo fMRI responses. **d**, Comparison of in silico and in vivo fMRI response noise, in arbitrary units.

Using RCN, we determined representational relationships across visual cortex, starting with human early- and mid-level visual cortical areas (V1, V2, V3, V4).

The first step was creating high-quality in silico brain responses for a large set of visual stimuli (**Fig. 1a**). For this we used the natural scenes dataset (NSD)<sup>27</sup>, a large-scale dataset of 7T fMRI responses from 8 subjects who each viewed ca. 10,000 natural scenes, for a total of 73,000 images across subjects, with 1,000 images shared across subjects. We trained subject-specific encoding models for areas V1 to V4, mapping image activations from a visual artificial deep neural network onto voxel-wise fMRI responses (**Supplementary Figure 1, Supplementary Figure 2a**). The trained encoding models accurately predicted fMRI responses not used for training, resulting in a subject-average noise-ceiling-normalized explained variance score of 78.14% for V1, 72.54% for V2, 65.07% for V3, and 53.29% for V4 (**Supplementary Figure 2b**, single-subject results shown in **Supplementary Figure 3**). We further tested the robustness of the encoding models on NSD-synthetic<sup>28</sup>, NSD's out-of-distribution companion dataset of fMRI responses to artificial images, obtaining a subject-average noise-ceiling-normalized explained variance score of 60.72% for V1, 52.22% for V2, 46.75% for V3, and 38.89% for V4 (single-subject results shown in **Supplementary Figure 3**). These results indicate that the trained encoding models generate reliable in silico fMRI responses, including for images very different from the ones on which the models were trained, therefore providing a solid foundation for in silico experiments. Using the trained encoding models, we generated in silico fMRI responses to all 73,000 NSD images for each

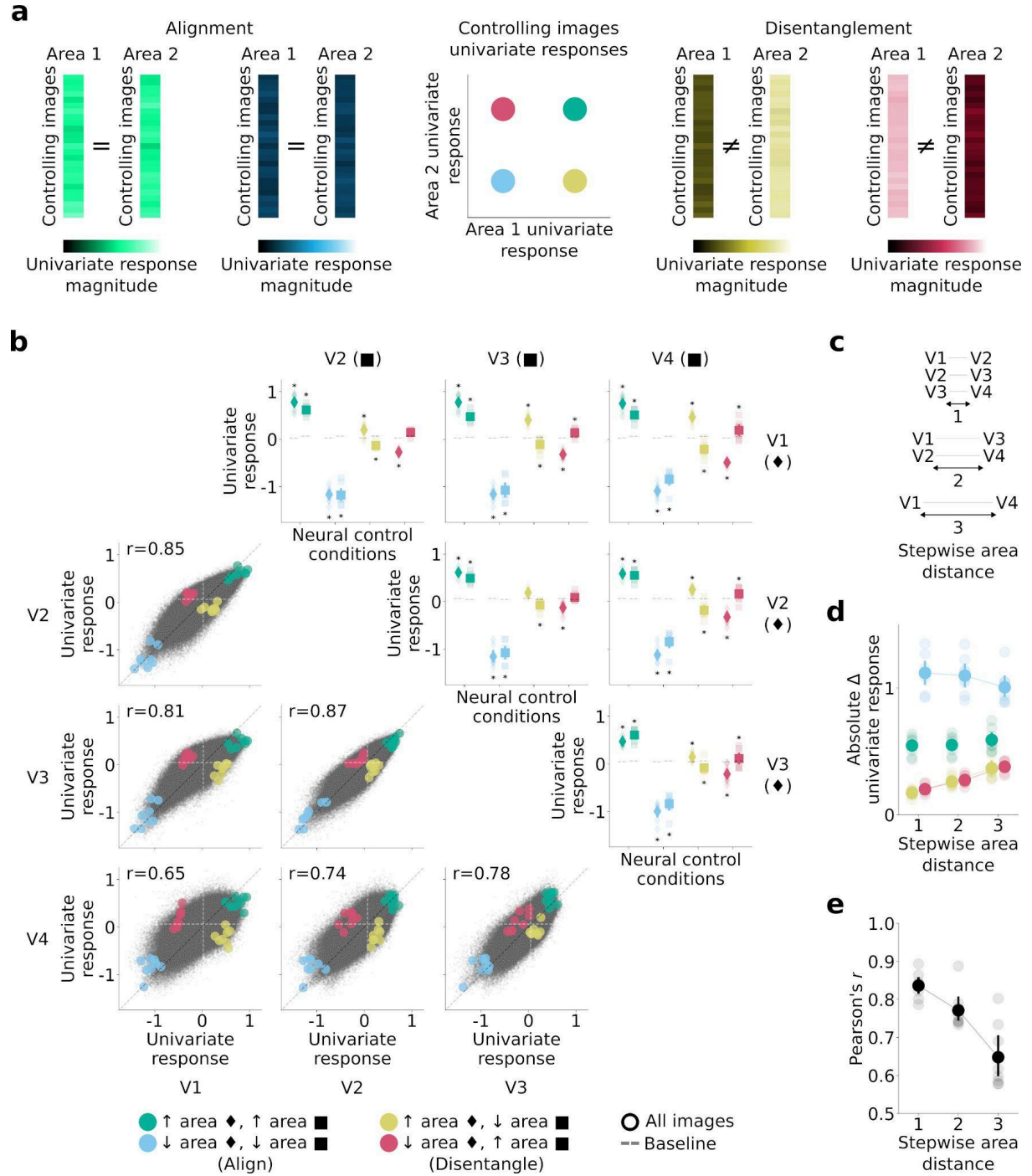
of the 8 subjects, thus increasing the number of image-specific brain responses per subject by a factor of ~7 (**Fig. 1b**).

This had three advantages. First, the large number of responses allowed for wider exploration than possible with in vivo data, thus reducing experimental biases inherent in small data sets. Second, as the in-silico-generated fMRI responses for the whole 73,000 images were present for all subjects, this allowed for more robust cross-subject validation than would be possible using the in vivo responses to only 1,000 shared images from the NSD (**Fig. 1c**), thus reducing overfitting. Finally, since neural noise is not predictable from the stimulus images, encoding models modeled the signal- and not noise-related variability of the neural response<sup>19,29</sup>, thus resulting in silico fMRI responses less affected by noise compared to the NSD responses (**Fig. 1d**; for the noise comparison see **Supplementary Figure 2c-d**).

Together, this provided the basis for revealing representational relationships.



# RNC controls in silico univariate fMRI responses across early- and mid-level visual cortical areas



areas; population prevalence test,  $p < 0.01$ , indicating within-subject significance in at least 3/8 subjects). The lower triangle of the results matrix shows the univariate response image manifolds. Colored dots indicate in silico univariate fMRI responses averaged across the controlling images of each neural control condition, and small black points indicate in silico univariate fMRI responses of all subjects for all 73,000 NSD images. Vertical and horizontal dashed lines indicate subject-average univariate response baseline for each area. **c**, Stepwise distances between areas. **d**, Absolute difference between controlling and baseline image univariate responses, averaged across all pairwise comparisons of areas with same stepwise distance. Connectors between area distances indicate a significant increasing trend (within-subject permutation test,  $p < 0.05$ , Benjamini/Hochberg corrected over 4 tests; population prevalence test,  $p < 0.001$ , indicating within-subject significance in at least 4/8 subjects). **e**, Correlation between univariate responses in two areas, averaged across pairwise comparisons of areas with same stepwise distance. Connectors between area distances indicate a significant decreasing trend (within-subject permutation test,  $p < 0.05$ ; population prevalence test,  $p < 10^{-10}$ , indicating within-subject significance in all 8 subjects). Opaque and transparent diamonds/squares/dots represent subject-average and single subject results, respectively. Error bars reflect 95% confidence intervals.

We began by investigating representational relationships for in silico univariate fMRI responses (i.e., the average activity over all voxels within an area), thus capturing visual information encoded in the strongest activation trends common across voxels<sup>16,21–23</sup>.

For each pairwise comparison of areas (V1 vs. V2, V1 vs. V3, V1 vs. V4, V2 vs. V3, V2 vs. V4, V3 vs. V4), we used univariate RNC to search, across all 73,000 NSD images, for images that would either align or disentangle (i.e., control) the in silico univariate fMRI responses of the two areas being compared, thus indicating shared or unique representational content, respectively. Alignment consisted in two neural control conditions where the univariate responses of both areas were either driven or suppressed. Disentanglement consisted in two neural control conditions where the univariate response of one area was driven while the response of the other area suppressed, or vice versa (**Fig. 2a**; the univariate RNC algorithm is visualized in **Supplementary Figure 4**). To assess the success of the neural control conditions, we compared them against a baseline of univariate responses for a set of images selected without optimization. We used cross-subject validation, thus ensuring generalization of results.

Through univariate RNC we found images that significantly drove and suppressed univariate responses of most pairwise comparisons of areas (within-subject permutation test,  $p < 0.05$ , Benjamini/Hochberg corrected over 8 tests for each pairwise comparison of areas; population prevalence test,  $p < 0.01$ , indicating within-subject significance in at least 3/8 subjects) (**Fig. 2b**, upper triangle of the results matrix). Thus, we successfully aligned or disentangled different areas at the univariate response level. For each pairwise comparison of areas, we then visualized the in silico fMRI response manifolds for all 73,000 images in univariate activity space and found their activation profiles to be highly correlated, suggesting that a large portion of representational content is shared across areas (**Fig. 2b**, lower triangle of the results matrix).

Visual areas V1 to V4 form a processing hierarchy in terms of anatomical connectivity<sup>5</sup>, response latency<sup>30</sup>, and the complexity of stimulus properties maximally driving neural

responses<sup>1</sup>. This suggests that disentanglement should increase and that alignment should decrease with increasing node distance across this hierarchy (**Fig. 2c**). We confirmed this prediction. As the stepwise distance between two areas increased, the absolute difference between the in silico univariate fMRI responses in the disentangling control condition and the baseline increased (within-subject permutation test,  $p < 0.05$ , Benjamini/Hochberg corrected over 4 tests; population prevalence test,  $p < 0.001$ , indicating within-subject significance in at least 4/8 subjects) (**Fig. 2d**, yellow and red dots). Furthermore, the absolute distance between the univariate responses in the alignment control condition suppressing both areas (but not driving them) and the baseline decreased (within-subject permutation test,  $p < 0.05$ , Benjamini/Hochberg corrected over 4 tests; population prevalence test,  $p < 10^{-9}$ , indicating within-subject significance in 7/8 subjects) (**Fig. 2d**, blue dots). This indicates that the univariate responses of areas further away from each other were less aligned and more strongly disentangled. Strengthening this finding, as the stepwise distance between two areas increased, the correlation between their univariate responses decreased (within-subject permutation test,  $p < 0.05$ ; population prevalence test,  $p < 10^{-10}$ , indicating within-subject significance in all 8 subjects) (**Fig. 2e**).

To ascertain that the demonstrated representational relationships reflect properties of visual processing, rather than biases of specific datasets, we performed two tests. First, to ensure that RNC's solutions are not biased by the visual distribution from which the controlling images are selected, we applied univariate RNC on the in silico fMRI responses for the 50,000 images from the ImageNet 2012 challenge validation split<sup>31</sup>, and for the 26,107 images from THINGS<sup>32</sup> (i.e., single objects presented centrally on natural backgrounds, as opposed to the NSD's complex natural scenes consisting of several or no objects appearing at different locations). Second, to ensure that RNC's solutions are not biased by the visual distribution of the encoding models' training data, we applied univariate RNC on the in silico fMRI responses generated from encoding models trained on the Visual Illusion Reconstruction dataset<sup>33</sup> (i.e., fMRI responses for images of diverse objects, natural scenes, and materials). Both tests replicated our previous findings (**Supplementary Figures 5-7**), demonstrating RNCs robustness and generalizability, and indicating that its solutions truly reflect properties of the brain.

Together, through univariate RNC we discovered controlling images that align or disentangle the in silico univariate fMRI responses of multiple areas, revealing that a large portion of univariate responses representational content is shared between areas, and that unique representational content increases as a function of cortical distance.

# Spatial frequency and object-like shapes determine unique representational content for V1 and V4 in silico univariate fMRI responses

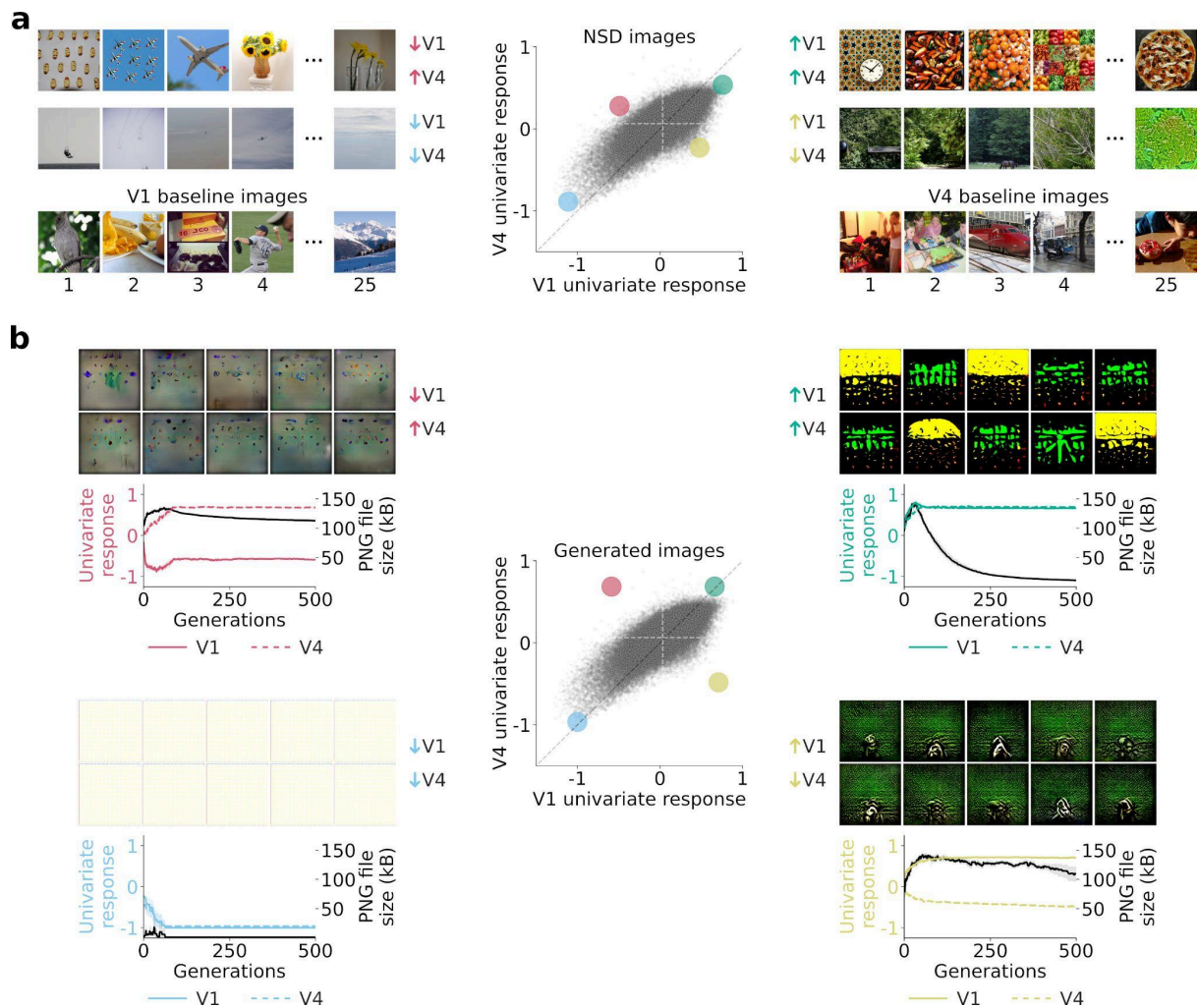


**Fig. 3 | Spatial frequency and object-like shapes determine unique representational content for V1 and V4 in silico univariate fMRI responses. a**, V1 vs. V4 neural control scores and controlling/baseline images obtained by applying univariate RNC jointly on the in silico fMRI responses of all 8 subjects for the 73,000 NSD images. **b**, Results of ten independent generative univariate RNC evolutions using in silico fMRI responses averaged across all 8 subjects. For each neural control condition, the plots show the in silico univariate fMRI responses (represented by colored lines) and the PNG compression file size (represented by black lines) for the best generated image of each genetic algorithm generation, averaged across the ten evolutions. The vertical dashed lines indicate the generation where the univariate response threshold is reached (also averaged across evolutions), after which PNG compression file size starts decreasing. On top of each plot are the optimized images from the ten evolutions.

To determine the visual features leading to aligned or disentangled responses of different areas, we visualized the controlling images that aligned and disentangled their univariate responses. Here we exemplarily focus on the V1 vs. V4 comparison (**Fig. 3a**).

The controlling images driving V1 while suppressing V4 responses contained high spatial frequency backgrounds (e.g., green vegetation), whereas the controlling images driving V4 while suppressing V1 responses contained one or multiple objects on a low spatial frequency background (e.g., a plane on a sky background). Controlling images driving or suppressing both areas simultaneously were the logical combination thereof: high spatial frequency and objects were present in controlling images driving the response of both areas (e.g., warm-color cluttered food items), whereas they were lacking in controlling images suppressing the response of both areas (e.g., empty skies). As expected, we discerned no consistent visual patterns in the baseline images. When using alternative distributions of images and of encoding model training data, the resulting controlling images also consisted of combinations of high spatial frequencies and objects (**Supplementary Figures 5-7**). However, they did not always contain green vegetation, planes on a sky background, or warm-color cluttered food items (as was the case with the NSD images in **Fig. 3a**), suggesting that these visual categories correlate with, but are not, the visual features controlling univariate responses. This showed, through large-scale exploratory analysis using naturalistic images from diverse image sets, that V1 is uniquely tuned to high spatial frequency content<sup>34,35</sup>, whereas V4 is uniquely tuned to object-like shapes<sup>36</sup>.

Naturalistic images are complex combinations of multiple visual features making it challenging to isolate, by mere visual inspection, the features leading to aligned or disentangled responses across areas. To further isolate the relevant visual features, we generated de novo controlling images that controlled univariate responses, while being as simple as possible. To this end, we combined RNC with an image generator<sup>37</sup> and genetic optimization<sup>38,39</sup> to iteratively generate images following two serial objectives. The first objective, active throughout the entire optimization procedure, was to generate images controlling (i.e., driving or suppressing) in silico univariate fMRI responses of V1 and V4 up to a threshold. Once this threshold was reached, the second objective became activated, which was to lower image complexity as measured by the images' PNG compression file size<sup>40,41</sup>, while at the same time keeping the univariate responses above threshold. This promoted the generation of controlling images (first objective) containing only the visual features strictly necessary to align or disentangle in silico univariate fMRI responses (second objective) (**Fig. 3b**; the generative univariate RNC algorithm is visualized in **Supplementary Figure 8**; for a fine-grained progression of images across generations see **Supplementary Figure 9**). For each neural control condition we ran ten independent evolutions, resulting in ten genetically optimized images for each condition.

Inspection of the genetically optimized images converged with the insights previously gained by naturalistic images. The genetically optimized images driving V1 while suppressing V4 consisted of an uniform high spatial frequency pattern, whereas the images driving V4 while suppressing V1 consisted of multiple small object-like shapes on a uniform background. The images driving or suppressing both areas were again logical combinations of the previous cases: the images driving both areas consisted of many small object-like shapes clustered together, and the images suppressing both areas consisted of a uniform white background. The fact that all ten generated images within each neural control condition were strikingly similar to each other indicates that these controlling visual features are the ones optimally aligning or disentangling V1 and V4. Further supporting this, generating images without the image complexity constraint led to images that, albeit visually more complex, still contained the same controlling visual features (**Supplementary Figure 10**).

Together, this shows that high spatial frequencies and object-like shapes are the visual features leading to unique representational content for V1 and V4 in silico univariate fMRI responses.



# RNC controls in silico multivariate fMRI responses across early- and mid-level visual cortical areas

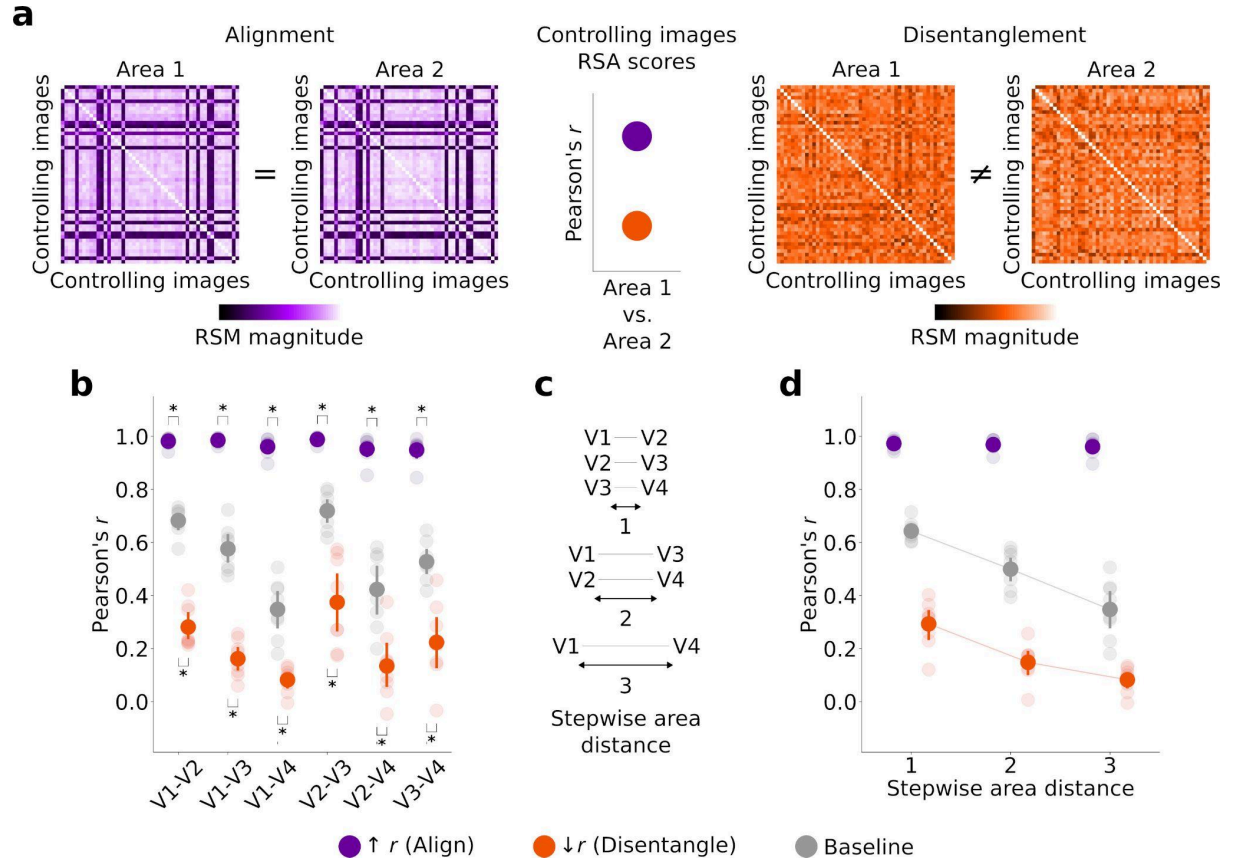


**Fig. 4 | RNC controls in silico multivariate fMRI responses across early- and mid-level visual cortical areas.** **a**, Multivariate RNC neural control conditions. **b**, Multivariate RNC results, consisting of RSA scores (Pearson's  $r$ ) for each pairwise comparison of areas. Asterisks indicate neural control conditions for which the RSA scores from the controlling images are significantly higher (alignment) or lower (disentanglement) than baseline (within-subject permutation test,  $p < 0.05$ , Benjamini/Hochberg corrected over 2 tests for each pairwise comparison of areas; population prevalence test,  $p < 10^{-9}$ , indicating within-subject significance in at least 7/8 subjects). **c**, Stepwise distances between areas. **d**, Multivariate RNC RSA scores, averaged across pairwise comparisons of areas with same stepwise distance. Connectors between area distances indicate a significant decreasing trend (within-subject permutation test,  $p < 0.05$ , Benjamini/Hochberg corrected over 3 tests; population prevalence test,  $p < 10^{-5}$ , indicating within-subject significance in at least 5/8 subjects). Opaque and transparent dots represent subject-average and single subject results, respectively. Error bars reflect 95% confidence intervals.

We next used RNC to reveal the representational relationships for visual information encoded in in silico multivariate fMRI responses (i.e., the population response patterns over all voxels within an area, rather than averaged voxel responses)<sup>21,22,24–26</sup>.

To control in silico multivariate fMRI responses across areas, their response patterns must be directly comparable to each other. We thus transformed response patterns into representational similarity matrices (RSMs), capturing the representational geometry of each

area in a common format<sup>25</sup>. For each pairwise comparison of areas, we used multivariate RNC and genetic optimization<sup>38,39,42,43</sup> to search, across all 73,000 NSD images, for controlling image batches that would either align or disentangle the RSMs of the two areas being compared. Alignment consisted in an image batch leading to a high representational similarity analysis (RSA)<sup>25</sup> correlation score (i.e., Pearson's  $r$ ) for the RSMs of the two areas. Disentanglement consisted in an image batch leading to a low absolute RSA correlation score for the RSMs of the two areas (**Fig. 4a**; the multivariate RNC algorithm is visualized in **Supplementary Figure 11**). The results were cross-subject validated and compared to a baseline RSM defined on an image batch selected without optimization.

Through multivariate RNC we found controlling image batches that significantly aligned and disentangled the RSMs of all pairwise comparisons of areas (within-subject permutation test,  $p < 0.05$ , Benjamini/Hochberg corrected over 2 tests for each pairwise comparison of areas; population prevalence test,  $p < 10^{-9}$ , indicating within-subject significance in at least 7/8 subjects) (**Fig. 4b**; for the genetic optimization curves see **Supplementary Figure 12**). Thus, we successfully aligned or disentangled different areas at the multivariate response level.

Here too we tested whether alignment of multivariate responses decreases, and disentanglement increases, with increasing node distance across the visual processing hierarchy (**Fig. 4c**). The RSA scores for the disentangling and baseline images decreased as the stepwise distance between two areas increased (within-subject permutation test,  $p < 0.05$ , Benjamini/Hochberg corrected over 3 tests; population prevalence test,  $p < 10^{-5}$ , indicating within-subject significance in at least 5/8 subjects), but the RSA scores for the aligning images did not decrease, likely due to a ceiling effect (**Fig. 4d**). Thus, the multivariate responses of areas further away from each other were more strongly disentangled.

We verified the generalizability of these representational relationships, observing quantitatively similar results when using alternative distributions of images and of encoding model training data (**Supplementary Figures 13-15**).

Together, through multivariate RNC we discovered controlling images that align or disentangle the in silico multivariate fMRI responses of multiple areas, revealing that while a large portion of representational content is shared between multivariate responses across visual areas, unique representational content increases as a function of cortical distance.



# Shared representational content for V1 and V4 in silico multivariate fMRI responses stems from similar retinotopic properties

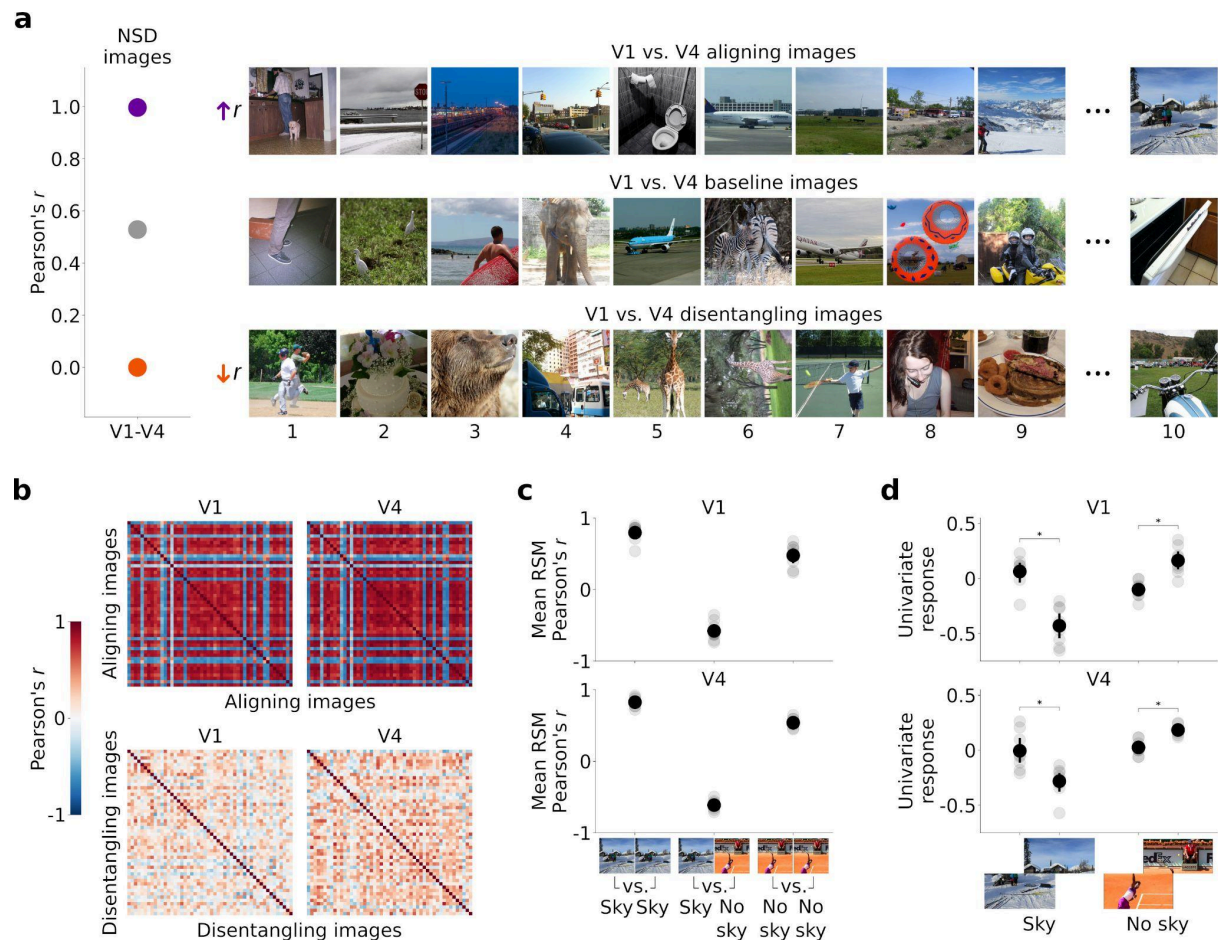


**Fig. 5 | Shared representational content for V1 and V4 in silico multivariate fMRI responses stems from similar retinotopic properties.** **a**, V1 vs. V4 neural control scores and controlling/baseline images obtained by applying multivariate RNC jointly on the in silico fMRI responses of all 8 subjects for the 73,000 NSD images. **b**, V1 and V4 subject-average RSMs for the multivariate RNC aligning and disentangling images. **c**, V1 and V4 aligning images RSMs mean Pearson's  $r$  scores across all comparisons of two sky images, two no sky images, or sky and no sky images. **d**, V1 and V4 mean univariate response for aligning images that either contain or do not contain the sky in their upper half, divided into voxels tuned to the lower and upper part of the visual field. Asterisks indicate a significant difference between the univariate responses of voxels tuned to the lower and upper part of the visual field (within-subject permutation test,  $p < 0.05$ , Benjamini/Hochberg corrected over 2 tests for each area; population prevalence test,  $p < 10^{-5}$ , indicating within-subject significance in at least 5/8 subjects). Opaque and transparent dots represent subject-average and single subject results, respectively. Error bars reflect 95% confidence intervals.

Which visual features underlie the representational relationships captured in multivariate responses? Here we focus on the V1 vs. V4 comparison (**Fig. 5a**).

The aligning images often contained uniform portions (i.e., the sky on their upper half), whereas the disentangling images did not, and the baseline images did but to a lesser extent (**Fig. 5a**). This was also the case when using alternative distributions of images and of encoding model training data (**Supplementary Figures 13-15**).

To understand the effect of image properties on the multivariate RNC scores, we visually inspected the V1 and V4 RSMs in conjunction with the controlling images (**Fig. 5b**). For both areas, RSM entries comparing different images including the sky in their upper half indicated highly positive correlations, while RSM entries comparing images with and without the sky in the upper half indicated highly negative correlations (**Fig 5c; Supplementary Figure 16a**). This similar combination of highly positive and negative correlation RSM entries led to a high RSA correlation score for V1 and V4 and thus to alignment. On the other hand, upon visual inspection the V1 and V4 RSMs for the disentangling images contained correlation scores of lower absolute magnitude and did not reveal common visual patterns (**Fig. 5b**).

Combining the insights gained from inspecting controlling images and RSMs, we stipulated that retinotopic organization determines neural alignment<sup>44</sup>: uniform regions on a spatially constrained portion of the image will lead to suppressed responses for V1 and V4 voxels tuned to the corresponding portion of the visual field, in turn leading to aligned RSMs for the two areas.

We tested this hypothesis by comparing the V1 and V4 univariate responses of voxels tuned to the upper and lower portion of the visual field, for aligning images including uniform regions (i.e., the sky) in their upper half. As predicted, for both areas the univariate response of voxels was lower for the upper than for the lower visual field (within-subject permutation test,  $p < 0.05$ , Benjamini/Hochberg corrected over 2 tests for each area; population prevalence test,  $p < 10^{-5}$ , indicating within-subject significance in at least 5/8 subjects) (**Fig. 5d**), explaining why RSM entries comparing different images including the sky in their upper half resulted in highly positive correlations (**Supplementary Figure 16b**). We observed the opposite pattern when comparing voxel responses for aligning images not including the sky in their upper half (within-subject permutation test,  $p < 0.05$ , Benjamini/Hochberg corrected over 2 tests for each area; population prevalence test,  $p < 10^{-9}$ , indicating within-subject significance in at least 7/8 subjects) (**Fig. 5d**), explaining why RSM entries comparing images with and without the sky in the upper half resulted in highly negative correlations (**Supplementary Figure 16b**).

Together, these results point to common retinotopic properties as a source of shared representational content in V1 and V4 in silico multivariate fMRI responses.

# RNC controls in silico univariate and multivariate fMRI responses across high-level visual cortical areas

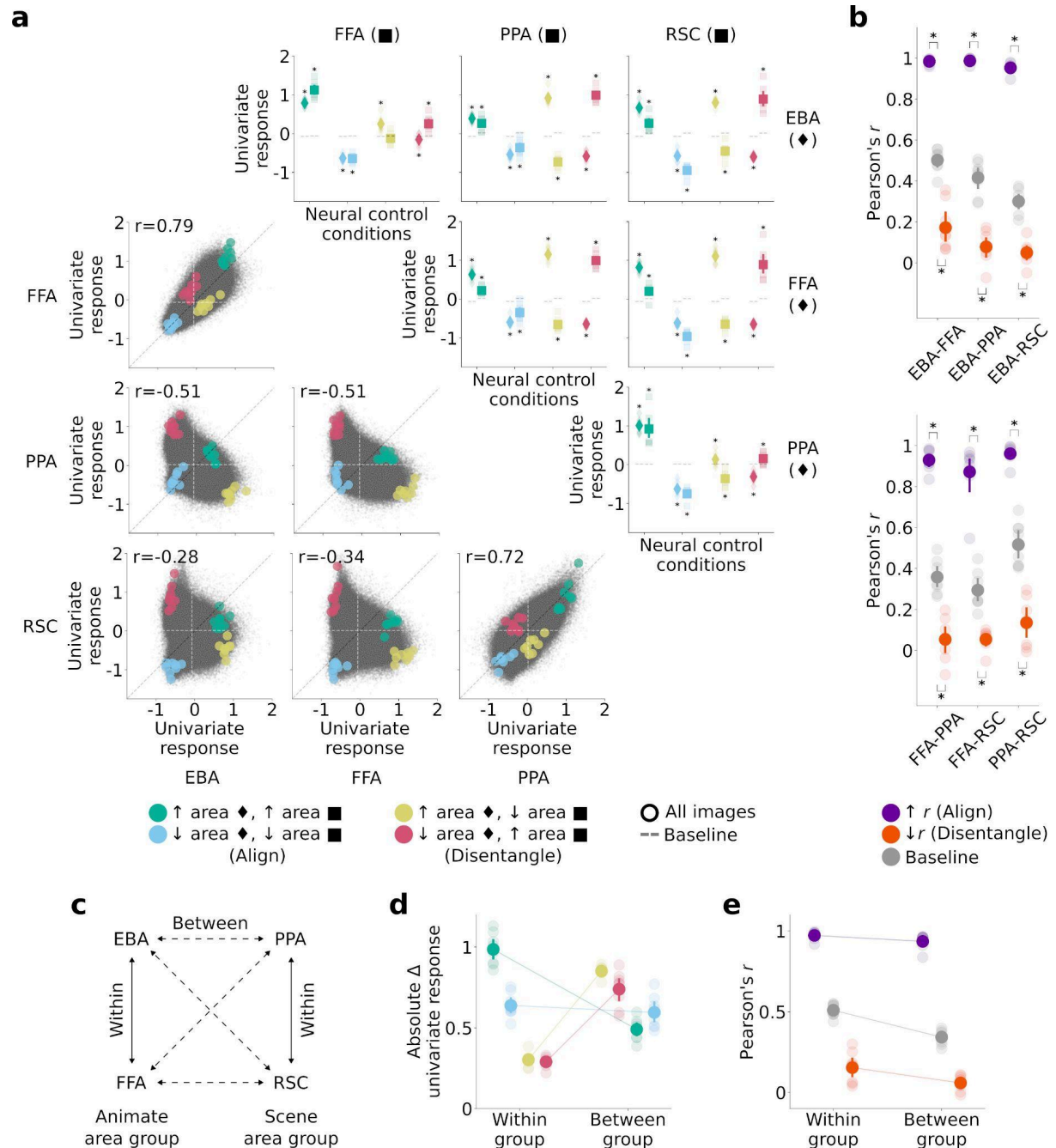


**Fig. 6 | RNC controls in silico univariate and multivariate fMRI responses across high-level visual cortical areas.** **a**, Univariate RNC results for each pairwise comparison of areas, embedded in a four-by-four matrix. The upper triangle of the results matrix shows the univariate responses for the controlling images against the baseline. Diamonds and squares indicate the univariate responses of the areas indexed by the rows and columns of the results matrix, respectively. Asterisks indicate neural control conditions for which the in silico univariate fMRI responses for the controlling images are significantly different from baseline (within-subject permutation test,  $p < 0.05$ , Benjamini/Hochberg corrected over 8 tests for each pairwise comparison of areas; population prevalence test,  $p < 0.01$ , indicating within-subject significance in at least 3/8 subjects). The lower triangle of the results matrix shows the univariate response image

manifolds. Colored dots indicate *in silico* univariate fMRI responses averaged across the controlling images of each neural control condition, and small black points indicate *in silico* univariate fMRI responses of all subjects for all 73,000 NSD images. Vertical and horizontal dashed lines indicate subject-average univariate response baseline for each area. **b**, Multivariate RNC results, consisting of RSA scores (Pearson's  $r$ ) for each pairwise comparison of areas. Asterisks indicate neural control conditions for which the RSA scores from the controlling images are significantly higher (alignment) or lower (disentanglement) than baseline (within-subject permutation test,  $p < 0.05$ , Benjamini/Hochberg corrected over 2 tests for each pairwise comparison of areas; population prevalence test,  $p < 10^{-9}$ , indicating within-subject significance in at least 7/8 subjects). **c**, Categorical selectivity groups. Solid and dashed lines represent within- and between- group area comparisons, respectively. **d**, Absolute difference between controlling and baseline image univariate responses, averaged across within- or between-group area comparisons. Connectors indicate significant differences (within-subject permutation test,  $p < 0.05$ , Benjamini/Hochberg corrected over 4 tests; population prevalence test,  $p < 0.001$ , indicating within-subject significance in at least 4/8 subjects). **e**, Multivariate RNC RSA scores, averaged across within- or between-group area comparisons. Connectors indicate significant differences (within-subject permutation test,  $p < 0.05$ , Benjamini/Hochberg corrected over 3 tests; population prevalence test,  $p < 0.01$ , indicating within-subject significance in at least 3/8 subjects). Opaque and transparent diamonds/squares/dots represent subject-average and single subject results, respectively. Error bars reflect 95% confidence intervals.

Next, we extended RNC from early- and mid- to high-level visual areas. Using NSD, we trained encoding models of high-level visual areas that play a key role in the representation of bodies (EBA<sup>45</sup>), faces (FFA<sup>23</sup>), scenes (PPA<sup>46</sup>), and in visual navigation (RSC<sup>47</sup>) (encoding accuracies are shown in **Supplementary Figure 3**). Through RNC, we found controlling images that successfully aligned or disentangled both univariate (**Fig. 6a**) and multivariate (**Fig. 6b**) *in silico* fMRI responses for the 73,000 NSD images generated through these encoding models (within-subject permutation test,  $p < 0.05$ , Benjamini/Hochberg corrected over 8 or 2 tests for each univariate or multivariate RNC pairwise comparison of areas respectively; population prevalence test,  $p < 0.01$ , indicating within-subject significance in at least 3/8 subjects) (RNC results for interactions between early-, mid-, and high-level visual areas are shown in **Supplementary Figures 17-19**). Thus, we successfully aligned or disentangled different high-level visual cortical areas at the univariate and multivariate response levels.

EBA, FFA, PPA, and RSC fall within two broader groups of categorical selectivity: animate objects (EBA and FFA), and scenes (PPA and RSC). This suggests that alignment should be higher and disentanglement lower for within-group areas than for between-group areas (**Fig. 6c**). We confirmed this prediction. For univariate RNC, the absolute difference between the *in silico* univariate fMRI responses in the control conditions and the baseline was larger for within-group areas in the case of alignment (**Fig. 6d**, green and blue dots), and larger for between-group areas in the case of disentanglement (**Fig. 6d**, yellow and red dots) (within-subject permutation test,  $p < 0.05$ , Benjamini/Hochberg corrected over 4 tests; population prevalence test,  $p < 0.001$ , indicating within-subject significance in at least 4/8 subjects). This indicates that the responses of within-group areas were more aligned and less disentangled, compared to between-group areas. Strengthening this finding, the univariate responses of within-group areas were strongly correlated, whereas the responses of between-group areas were anticorrelated (**Fig. 6a**, lower triangle of the results matrix).

Similarly, for multivariate RNC the RSA scores for the aligning, disentangling, and baseline images were higher for within-group areas (**Fig. 6e**) (within-subject permutation test,  $p < 0.05$ , Benjamini/Hochberg corrected over 3 tests; population prevalence test,  $p < 0.01$ , indicating within-subject significance in at least 3/8 subjects). We observed quantitatively similar results when using alternative distributions of images (**Supplementary Figures 20-21**).

Together, through RNC we discovered controlling images that align or disentangle the in silico univariate and multivariate fMRI responses of high-level visual areas. This demonstrated RNC's applicability across the visual cortical network, and revealed that shared representational content is higher and unique representational content lower for high-level visual areas with similar categorical selectivity.



# Representational relationships between visual areas adaptively vary around a typical network-level configuration

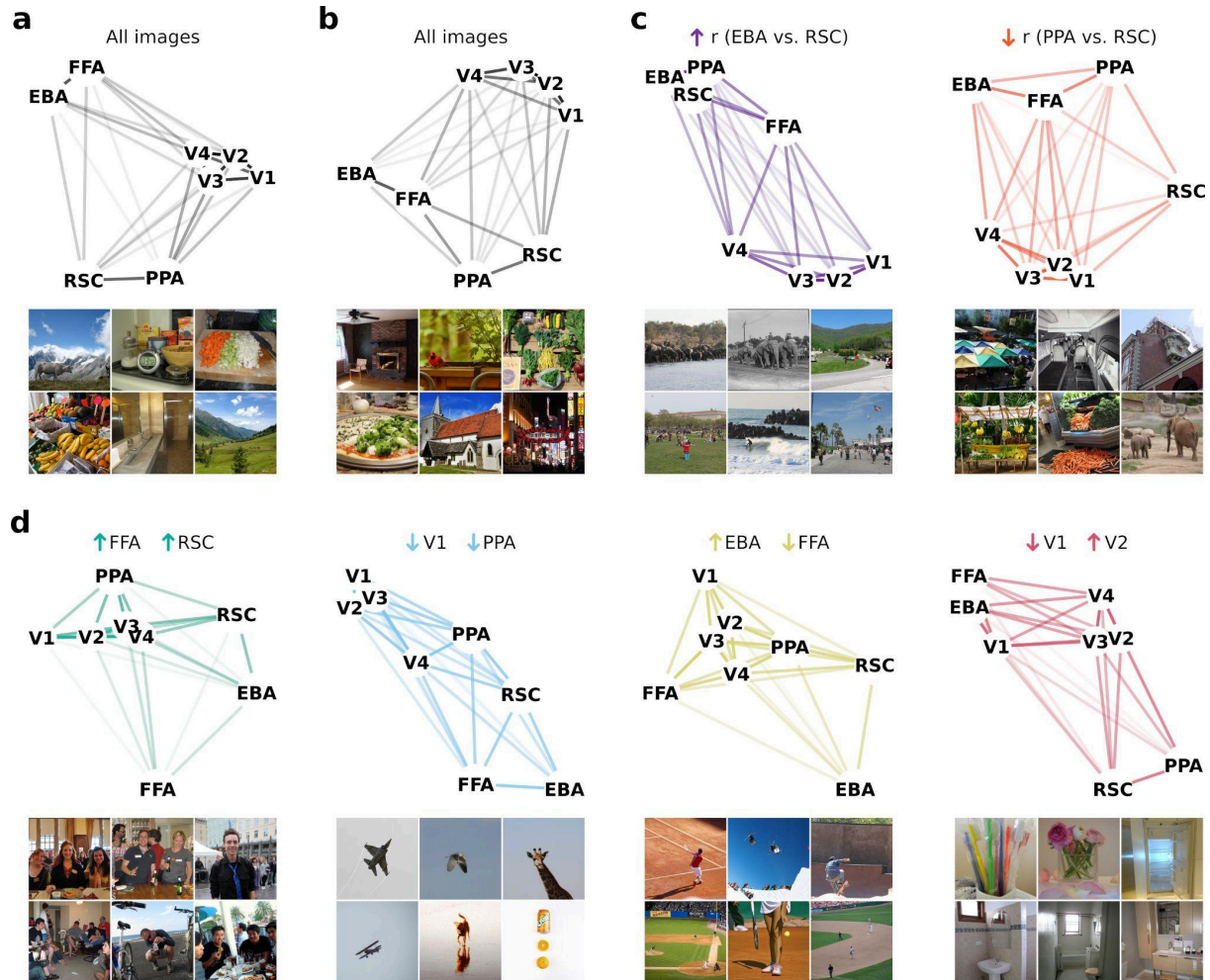


**Fig. 7 | Representational relationships between visual areas adaptively vary around a typical network-level configuration.** **a**, Multidimensional scaling (MDS) embeddings of the in silico univariate fMRI responses of early-, mid-, and high-level visual areas for all 73,000 NSD images, indicating the typical representational relationship configuration of the visual cortical network. **b**, MDS embeddings of the in silico multivariate fMRI responses for all 73,000 NSD images, indicating the typical representational relationship configuration of the visual cortical network. **c**, MDS embeddings of the in silico multivariate fMRI responses for the controlling images from two multivariate RNC control conditions: images aligning EBA and RSC (purple condition), or disentangling PPA and RSC (orange condition). **d**, MDS embeddings of the in silico univariate fMRI responses for the controlling images from four univariate RNC control conditions: images driving both FFA and RSC (green condition), suppressing both V1 and PPA (blue condition), driving EBA while suppressing FFA (yellow condition), or suppressing V1 while driving V2 (red condition). The opacity of the lines connecting each area reflects the proximity of these areas in two-dimensional embedding space (more opaque lines indicate higher proximity). A higher proximity between two areas indicates a stronger resemblance of their representational content. Six representative images are shown for each multidimensional scaling analysis.

Vision is enabled by a complex interconnected network of cortical areas that jointly represent visual information. Thus, we next moved to the network-level visualization of the representational relationships discovered for individual pairwise comparisons of areas.

We first asked what is the typical representational relationship configuration of areas within the visual cortical network. Using multidimensional scaling (MDS)<sup>48</sup>, we reduced the dimensionality of the subject-average in silico univariate or multivariate fMRI responses for all 73,000 NSD images of early-, mid-, and high-level visual areas (V1, V2, V3, V4, EBA, FFA, PPA, RSC). This resulted in two-dimensional embeddings where a higher proximity between two areas reflects a stronger resemblance of their representational content. For both univariate (**Fig. 7a**) and multivariate (**Fig. 7b**) in silico fMRI responses, these embeddings revealed three network-level properties that together defined a common, typical network-level configuration. First, that early- and mid-level visual areas' proximity in embedding space mirror their cortical distance, further supporting that unique representational content increases as a function of cortical distance. Second, that high-level visual areas cluster based on categorical selectivity for animate objects (EBA and FFA) and scenes (PPA and RSC), further supporting that shared representational content is higher and unique representational content lower for areas with similar categorical selectivity. Third, that early- and mid-level visual areas are closer to each other than they are to high-level visual areas, indicating an analogous relationship for their representational content.

Visual stimulation continuously alters the representational content of visual areas, leading to reconfigurations of these areas' representational relationships. Are these reconfigurations rigidly preserving the typical representational relationship configuration properties revealed above, or is the visual cortical network flexibly spanning any configuration? To assess this, we applied MDS on the in silico fMRI responses for the aligning or disentangling images selected through RNC. The controlling images led to representational relationship configurations that negated one, two, but not all three properties, indicating that representational relationships adaptively vary around their typical configuration (**Fig. 7c-d**). As an illustrative example, the controlling images suppressing V1 while driving V2's univariate responses moved V1 closer to V3 than to V2 thus negating the first property, and moved V1 closer to EBA/FFA than to the other early- and mid-level visual areas thus negating the third property (**Fig. 7d**, red condition; the representational relationship configurations for other RNC's pairwise area comparisons and control conditions are shown in **Supplementary Figures 22-25**).

Together, these results provide a unified picture of how visual areas jointly represent the world as an interconnected network. We showed that representational relationships between visual areas adaptively vary around a typical network-level configuration, and that RNC enables the exploration of the state space of possible network configurations.

## In-silico-discovered controlling images control in vivo fMRI responses of independent subjects

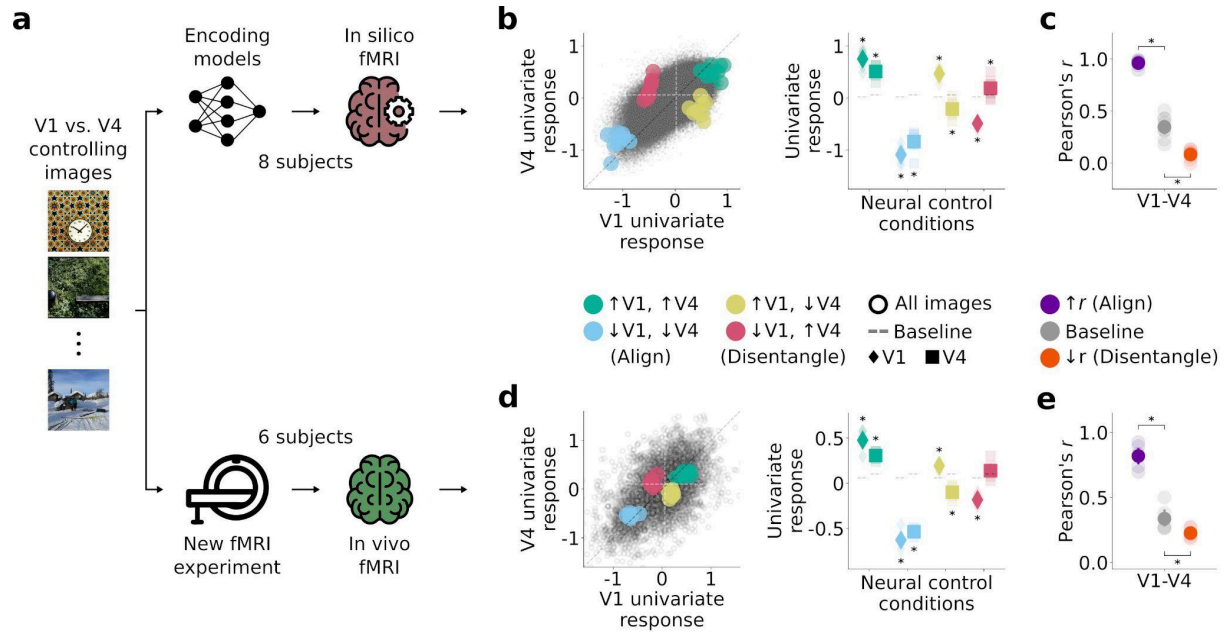


**Fig. 8 | In-silico-discovered controlling images control in vivo fMRI responses of independent subjects.** **a**, We tested whether the images controlling univariate and multivariate in silico fMRI responses for the V1 vs. V4 comparison generalized their control effect to in vivo fMRI responses of six new, independent subjects. **b**, Univariate RNC in silico results. **c**, Multivariate RNC in silico results. **d**, Univariate RNC in vivo results. Small black points indicate in vivo univariate fMRI responses of all subjects for all V1 vs. V4 univariate RNC controlling images. **e**, Multivariate RNC in vivo results. Asterisks indicate a significant effect of the controlling images with respect to baseline (within-subject permutation test,  $p < 0.05$ , Benjamini/Hochberg corrected over 8 or 2 tests for univariate or multivariate RNC respectively; population prevalence test,  $p < 10^{-4}$ , indicating within-subject significance in at least 4/6 subjects). Opaque and transparent dots/diamonds/squares represent subject-average and single subject results, respectively. Error bars reflect 95% confidence intervals.

In silico discoveries empower and accelerate empirical research, but do not replace it: these discoveries need to be validated empirically. Thus, we complemented the above results for areas V1 and V4 – which were cross-subject validated on in silico fMRI responses – with empirical validation on in vivo fMRI responses.

We conducted an fMRI experiment where we presented an independent set of subjects ( $n = 6$ ) with the univariate and multivariate RNC controlling images for the V1 vs. V4 comparison (**Fig. 8a**; for the experimental design see **Supplementary Figure 26a**). We defined V1 and V4 in the new subjects using population receptive field (pRF) mapping<sup>49</sup> (an illustration of the pRF experiment and the V1/V4 delineations are presented in **Supplementary Figure 26b-c**). We found that the controlling images aligned and disentangled both univariate (**Fig. 8d**) and multivariate (**Fig. 8e**) responses of V1 and V4 in these new subjects, (within-subject permutation test,  $p < 0.05$ , Benjamini/Hochberg corrected over 8 or 2 tests for univariate or multivariate RNC respectively; population prevalence test,  $p < 10^{-4}$ , indicating within-subject



significance in at least 4/6 subjects), except for V4's univariate response in the univariate neural control condition suppressing V1 while driving V4.

The successful generalization to in vivo fMRI responses closed the empirical cycle, confirming the in silico discoveries and validating RNC as a new exploratory neural control method for investigating representational relationships.

# Discussion

We investigated representational relationships between early-, mid-, and high-level visual areas of the human cortex using relational neural control (RNC). Through RNC, we extensively explored in silico fMRI responses for a vast collection of naturalistic images, finding controlling images that aligned or disentangled univariate and multivariate in silico fMRI responses across areas, thus indicating shared or unique representational content. Closing the empirical cycle, we validated the in silico discoveries on in vivo fMRI responses by presenting the controlling images to independent subjects.

Representations are the key concept in theories of information processing in visual cortex<sup>9,11–13,50,51</sup>, and because visual processing is supported by the concerted effort of multiple areas<sup>1–8</sup>, understanding how visual cortex works requires a joint investigation of the representational relationships between such areas. Thus, RNC invites a perspective shift from asking “What does each area represent?”, to asking “What is the *relationship* between representations in different areas?” RNC answers the latter question by applying neural control<sup>29,38,39,52–59</sup> jointly to multiple cortical areas, thus determining the causal role of specific visual input to their representational relationships<sup>53,60</sup>. Hence, RNC extends existing anatomical<sup>2</sup> and functional<sup>17</sup> connectivity research assessing the brain as a complex interconnected network with the concept of representation. Representations being the material of information processing and transfer<sup>9,13,61</sup>, our results promote the understanding of how perception and cognition emerge from the joint interaction of the representational content of multiple cortical areas.

Through RNC, we successfully controlled univariate and multivariate in silico fMRI responses jointly for areas across the visual cortical network. This confirmed representational properties known from investigating these areas in isolation, for example that V1 is tuned to high spatial frequencies<sup>34</sup>, that V4 is tuned to object-like shapes<sup>36</sup>, and that both areas are tuned to topological image properties<sup>44</sup>. Jointly controlling multiple areas additionally revealed network-level properties of how these areas represent the visual world that are not available from investigating them in isolation. First, that unique representational content of early- and mid- level visual areas increases as a function of cortical distance. This representational pattern likely reflects the decrease in anatomical connectivity with increasing distance between—areas<sup>5</sup>, as well as other gradual changes along the visual hierarchy such as increasing receptive field sizes<sup>62</sup> and increasingly complex functional specialization<sup>1</sup>. Second, that shared representational content is higher and unique representational content lower for high-level visual areas with similar categorical selectivity. The successful disentanglement of high-level visual areas with similar categorical selectivity (i.e., PPA and RSC<sup>63</sup>) demonstrates that RNC is sensitive to fine-grained representational differences. Furthermore, the successful control of RSC—an area that, beyond visual navigation, is also involved in memory and planning<sup>64</sup>—suggests that RNC could also reveal representational relationships properties of more anterior areas that contribute to visual processing, such as ventrolateral prefrontal cortex<sup>65</sup>. Third, that early- and mid-level visual areas are more similar to each other than they are to high-level visual areas in terms of representational content. Finally, that representational relationships between visual areas adaptively vary around a typical configuration defined by the previous three properties.

RNC builds on recent innovations in neural control, a paradigm used to find controlling stimuli that elicit a neural response state of interest. To increase the solution space and allow for rapid exploration, the controlling stimuli are found using large amounts of in silico neural responses generated by encoding models<sup>29,52–54,57</sup>. Next, to ensure that the controlling stimuli truly elicit the neural response state of interest, these stimuli are empirically validated on in vivo neural responses<sup>53,54,57</sup>. Finally, to elicit more complex neural response states of interest, multiple neurons or areas are jointly controlled<sup>29,53</sup>. Building on these innovations, RNC extends neural control research in two ways. First, RNC uses neural control to enable a network-level characterization of the representational relationships between visual cortical areas. Second, to investigate representational relationships at multiple brain response levels, RNC jointly applies neural control on univariate and multivariate neural responses. We found that the visual features aligning or disentangling V1 and V4’s univariate responses (i.e., spatial frequency and object-like shapes) are different from the ones aligning and disentangling their multivariate responses (i.e., topological image properties). Thus, the univariate and multivariate response levels captured complementary aspects of representational relationships between areas, suggesting that visual cortex multiplexes diverse neural codes for visual information processing<sup>9,61,66</sup> and, in turn, encouraging the integrated analysis of diverse neural response levels.

RNC embodies a research paradigm combining the advantages of in silico neural response exploration with empirical validation of findings on in vivo neural responses<sup>53,54,57,67,68</sup>. In silico exploration takes the power of recently emerging large-scale in vivo neural datasets<sup>27,69–71,33</sup> to the next level. In vivo neural responses are available in limited numbers and are expensive and slow to acquire. In contrast, after initial training on an in vivo dataset, encoding models cheaply and quickly generate in silico neural responses to any amount and type of stimuli, thus allowing for unprecedentedly large upscaling of the solution spaces on which to explore and test scientific hypotheses. Moreover, encoding models generate in silico neural responses which are less affected by noise compared to in vivo responses, thus reducing the effect of noise on results<sup>19,29</sup>. Together, this allows exploration of a much larger amount of stimuli and corresponding neural responses, effectively reducing the risk of sub-optimal or biased findings deriving from smaller and noisier samples or from experimenter’s hand-picked stimuli.

The key limitation of RNC lies in the component that empowers it: the encoding models generating the in silico neural responses do not predict all explainable neural signal, and their predictions generalize imperfectly beyond the distribution of the visual data they were trained on. Thus, to ascertain the validity of our findings we showed that our encoding models achieved high prediction accuracies when tested both in- and out-of-distribution, and also that RNC’s solutions are replicated when using alternative distributions of images and of encoding model training data. Furthermore, the current push in the development of more accurate and robust visual encoding models<sup>72–75</sup> using large in vivo data sets<sup>27,33,69–71</sup> that also include out-of-distribution components<sup>28,33,75</sup> promises increasingly accurate in silico neural responses, in turn increasing the reliability of findings from experimentation on computer-generated brain data.

The assumption of aligned or disentangled neural responses indicating shared or unique representational content is not a given. For example, for early- and mid-level visual areas we found that the assumption was correct for all multivariate RNC control conditions, for the

univariate RNC disentanglement conditions, but not for the univariate RNC alignment conditions. There, the controlling images aligning both V1 and V4 univariate fMRI responses consisted of the logical combination of the visual features disentangling them (i.e., high spatial frequency and objects), rather than of features for which the two areas are not disentangled, as would be the case if the assumption held. This might be the reason why the absolute distance between the univariate responses in the alignment control condition driving both areas and the baseline did not decrease with cortical distance (**Fig. 2d**, green dots). Together, this highlights a way to rigorously test the assumptions of RNC. Furthermore, finding the assumption to be negated is in itself scientifically interesting, as it reveals how either shared or unique representational content can lead to aligned univariate responses.

When one or few of the multiple stimulus features dominate the fMRI response magnitude, RNC primarily exploits these few features to align or disentangle the fMRI responses of two areas, resulting in images with few salient controlling visual features that are easier to interpret. As an example, the V1 vs. V4 controlling images from the multivariate RNC alignment condition contained easily interpretable visual patterns, which indicated that the shared representational content of these two areas' multivariate fMRI responses is dominated by image topological properties. When no stimulus feature dominates the fMRI response magnitude, RNC instead exploits multiple features, resulting in images with multiple controlling visual features that complicate interpretation. As an example, the multivariate RNC disentangling images for the V1 vs. V4 comparison did not reveal common patterns upon visual inspection, which suggests that the unique representational content of these two areas' multivariate fMRI responses is similarly determined by multiple non-dominating visual features. Determining the non-dominating visual features might be possible through RNC variants that isolate each of them, for example by using parameterized artificial stimuli for targeted hypothesis testing.

Feedforward and feedback connections both shape the representational content of visual areas within the cortical visual hierarchy<sup>5,76–78</sup>. Therefore, beyond feedforward processing<sup>12,50</sup>, shared and unique representational content might also be influenced by visual stimulation that either promotes (e.g., with challenging stimuli<sup>79,80</sup>) or suppresses (e.g., with visual masks<sup>81–83</sup>) feedback from higher areas to lower areas. Applying RNC on time-resolved M/EEG, ECoG, or electrophysiology data, or on cortical-layer resolved data<sup>84</sup>, is a promising avenue to isolate the respective influence of feedforward and feedback signaling on representational relationships.

In sum, using RNC we uncovered representational relationships between areas across the human visual cortex. This demonstrates the power of *in silico* exploration combined with *in vivo* validation to reveal how human cortical areas, at the level of networks, collectively represent the visual world.

# Methods

## Encoding models

The trained fMRI encoding models used to generate the in silico fMRI responses are available as part of the Neural Encoding Simulation Toolkit (NEST) (<https://github.com/gifale95/NEST>). Below we describe how these models were trained and tested.

## Data

The encoding models were trained on the Natural Scenes Dataset (NSD)<sup>27</sup>, a large-scale dataset of 7T fMRI responses from 8 subjects who each viewed up to 10,000 distinct color images of natural scenes. Out of these 10,000 images, 9,000 were subject-unique (i.e., only seen by individual subjects), and 1,000 were shared (i.e., seen by all subjects). Each image was presented up to three times, for a maximum of 30,000 trials per subject.

The fMRI data consisted of NSD's prepared fMRI responses in subject-native volume space ("func1pt8mm") from betas version 3 ("betas\_fithrf\_GLMdenoise\_RR"). To reduce session-specific noise, the responses of each voxel were z-scored across all trials of every data acquisition session. For model building, only voxels falling within areas V1, V2, V3, V4, EBA, FFA, PPA, and RSC were selected (using the area definitions provided by NSD).

To prevent results being biased towards noisy voxels (i.e., voxels with low stimulus-related signal), for all subsequent analyses we only used in silico fMRI responses for voxels with a noise ceiling signal-to-noise ratio (ncsnr) above 0.5. The ncsnr is a measure of stimulus-related signal in the fMRI responses, and its calculation is detailed below. We based the voxel selection on the ncsnr scores provided by the NSD data release. For the amount of retained voxels, see **Supplementary Tables 1-2**.

For each subject, the images and corresponding fMRI responses were split into training, validation, and testing partitions. The training partition consisted of the 9,000 subject-unique images. The testing partition consisted of the 515/1,000 shared images that were presented to all subjects three times (to maximize the reliability of the data on which the models were tested). The validation partition consisted of the remaining 485/1,000 shared images that were not presented to all subjects three times.

## Model architecture

Each encoding model predicted fMRI responses for multiple voxels (i.e., all voxels of a specific subject and area), and consisted of two components: a feature extractor shared across all voxels, and one projection head for each voxel (**Supplementary Figure 1a**).

The feature extractor is a multi-layer feedforward convolutional neural network called GNet<sup>27</sup> (**Supplementary Figure 1b**). Giving an image as input to GNet activates its layers, resulting in multiple features maps (i.e., GNet's representations of this image) (**Supplementary Figure**

**1a).** The feature extractor's weights are fully learned during model training, based on the joint loss of all voxels.

The projection head of each voxel is a feature-weighted receptive field (fwRF) that combines a spatial pooling field and feature weights<sup>27,85</sup>. The spatial pooling field determines the region of visual space (i.e., the GNet feature space which, due to the convolutional operations, preserves the topology of visual space of the input images) that drives voxel activity. After GNet's feature maps are spatially pooled, they are linearly combined by the feature weights, resulting in the voxel response prediction (**Supplementary Figure 1a**). Both the spatial pooling field and feature weights are learned during model training, independently for each voxel. This allows for the empirical determination of the optimal contribution of each model feature to each voxel based on the training data—for example, by learning the optimal hierarchical correspondence configuration between model layers and visual cortical areas<sup>86,87</sup>.

## Model training

Separate encoding models were trained for each NSD subject and area (V1, V2, V3, V4, EBA, FFA, PPA, RSC), resulting in 8 subjects × 8 areas = 64 encoding models. To reduce spurious statistical dependencies between the *in silico* (i.e., model-generated) fMRI responses from models of different subjects and areas, each model was trained starting from a different random initialization<sup>88</sup>.

Given an input image, the encoding model's objective was to minimize the mean squared error between the predicted fMRI responses (for all voxels of a given subject and area) and the corresponding target fMRI responses. During training, the mean squared error loss was backpropagated and the model weights updated (**Supplementary Figure 2a**). At each backpropagation step, the projection head weights were only optimized based on the loss of their corresponding voxel, whereas the feature extractor weights were optimized based on the loss combined over all voxels. The models were trained using single (i.e., not averaged) NSD trials.

The encoding models' weights were optimized on 75 epochs of the training data partition using batch sizes of 128 images and Pytorch's<sup>89</sup> Adam optimizer with a learning rate of 0.001, a weight decay term of 0, betas coefficients of (0.9, 0.999), and an eps term of 1e-08. The final model weights were taken from the epoch that achieved the lowest loss between the predicted and target fMRI responses, using the validation data partition.

## Model testing

We used the trained models to generate *in silico* fMRI responses for the test data partition images and compared them with the corresponding target responses, averaged across the three trials, using Pearson's correlation. We computed the correlation independently for each voxel across the 515 test images, set negative correlation coefficients to zero, and squared the resulting scores to obtain  $r^2$ , the total variance explained by the models. We then divided the  $r^2$  score of each voxel with that voxel's noise ceiling, resulting in the noise-ceiling-normalized explained variance, a measure that quantifies the portion of the explainable variance that had been accounted for by the models, given the noise in the data.

We tested the models independently for each voxel and subject, and then averaged the results across voxels belonging to the same subject and area (**Supplementary Figure 2b**, **Supplementary Figure 3**).

Following the same procedure, we additionally tested the encoding models' out-of-distribution generalization performance on NSD-synthetic<sup>28</sup>. NSD-synthetic consists of an additional scan session from the same eight NSD subjects, during which fMRI responses were measured to 284 carefully controlled synthetic (non-naturalistic) stimuli. We used NSD-synthetic's prepared fMRI responses in subject-native volume space ("func1pt8mm") from betas version 3 ("nsdsyntheticbetas\_fithrf\_GLMdenoise\_RR").

## Noise analysis

Because neural noise is not predictable from the stimulus images, encoding models model the signal- and not noise-related variability of the neural response, thus resulting in silico fMRI responses less affected by noise compared to in vivo responses<sup>19,29</sup>. To establish this empirically, we compared the noise of the in silico fMRI responses with the noise of the in vivo fMRI responses from the NSD, by comparing how much variance these two data types explained for a third, independent split of the in vivo NSD responses. Because the in silico fMRI responses did not capture all signal variance in the NSD responses (**Supplementary Figure 2b**, **Supplementary Figure 3**), the in silico fMRI responses explaining more variance than the in vivo NSD responses would be indicative of the former being less affected by noise. We carried out the comparison through three sets of predictions, using the in silico and the in vivo NSD fMRI responses for the 515 test images (**Supplementary Figure 2c**), and the same noise-ceiling-normalized explained variance metric described in the previous paragraph "Model testing". Each prediction involved explaining in vivo single response trials from the NSD experiment with a different predictor. In the first set of predictions, the predictor consisted of one of the two remaining in vivo NSD experiment response trials. We conducted six such predictions, such that each of the three in vivo NSD trials was used as the target to be explained and each of the two remaining in vivo NSD trials was used as a predictor. We then averaged the noise-ceiling-normalized explained variance scores from the six different predictions. In the second set of predictions, the predictor consisted of the average of the two remaining in vivo NSD experiment response trials. We conducted three such predictions, each time using one of the three in vivo NSD trials as the target to be explained and the average of the remaining two in vivo NSD trials as the predictor. We then averaged the noise-ceiling-normalized explained variance scores from the three different predictions. In the third set of predictions, the predictor consisted of the in silico responses from the trained encoding models. We repeated the prediction three times, each time using one of the three in vivo NSD trials as the target to be explained and the corresponding in silico responses as the predictor. We averaged the noise-ceiling-normalized explained variance scores from the three different predictions. We carried out these comparisons independently for each voxel and subject, and averaged the results across voxels belonging to the same subject and area.

## Noise ceiling derivation

We derived the noise ceiling of each voxel from its noise ceiling signal-to-noise ratio (ncsnr) score, provided by the NSD and computed on z-scored fMRI betas. For each voxel, the ncsnr quantified the ratio of the signal standard deviation over the noise standard deviation:

$$ncsnr = \frac{\hat{\sigma}_{signal}}{\hat{\sigma}_{noise}}$$

The noise standard deviation was obtained by calculating the variance of the betas across the three presentations of each image (using the unbiased estimator that normalizes by  $n-1$  where  $n$  is the sample size), averaging this variance across images, and then computing the square root of the result:

$$\hat{\sigma}_{noise} = \sqrt{\text{mean}(\beta_{\sigma}^2)}$$

where  $\beta_{\sigma}^2$  indicates the variance across the betas obtained for a given image. Given that the variance of the z-scored betas is 1, the signal standard deviation was estimated as:

$$\hat{\sigma}_{signal} = \sqrt{\left|1 - \hat{\sigma}_{noise}^2\right|_+}$$

where  $||_+$  indicates positive half-wave rectification. Finally, we used the ncsnr scores to derive the noise ceiling (NC) of each voxel as:

$$NC = 100 \times \frac{ncsnr^2}{ncsnr^2 + \frac{1}{n}}$$

where  $n$  indicates the number of trials that are averaged together. We used  $n = 3$  when evaluating the encoding models against the NSD test responses averaged across all three trials (**Supplementary Figure 2b**, **Supplementary Figure 3**), and  $n = 1$  during the noise analysis, since there we considered single trials as the target to be explained (**Supplementary Figure 2c**).

## Visual illusion reconstruction dataset

To ascertain that the RNC's solutions reflect properties of early- and mid-level visual areas, rather than biases of specific datasets, we additionally trained encoding models on the Visual Illusion Reconstruction (VIR) dataset<sup>33</sup>, fMRI responses of 7 subjects for 3,200 naturalistic images divided into 1,200 images of objects on natural backgrounds, 1,000 images of natural scenes, and 1,000 images of materials. Each of these images was presented 5 times for four of the seven subjects (for a total of 16,000 trials per subject), and 2 times for the remaining three subjects (for a total of 6,400 trials per subject). The fMRI data consisted of VIR's preprocessed fMRI responses in subject-native volume space, as provided in the data release. For model building, we selected voxels falling within areas V1, V2, V3, and V4 (using the area definitions provided by VIR). We computed the ncsnr and noise ceiling of each voxel following the procedure described above, and selected for further analyses only voxels with ncsnr above 0.5. Because area V4 of VIR subject 4 did not have voxels with ncsnr above 0.5, for this subject and area we instead lowered the ncsnr threshold to 0.4 (for the amount of retained voxels, see **Supplementary Table 3**).

For each subject, we split the images and corresponding fMRI responses into training, validation, and testing partitions. The training partition consisted of 2,500/3,200 images (900 objects, 800 scenes, and 800 materials). The validation partition consisted of 350/3,200 images (150 objects, 100 scenes, and 100 materials). The testing partition consisted of 350/3,200 images (150 objects, 100 scenes, and 100 materials). Following the procedure described above, we used this data to train and test separate encoding models for each VIR subject and area, resulting in 7 subjects  $\times$  4 areas = 28 encoding models. We additionally



tested the encoding models' out-of-distribution generalization performance on fMRI responses from the same 7 VIR subjects for 38 artificially created visual illusion images (the encoding accuracies are presented in **Supplementary Figure 3**).

## In silico fMRI responses generation

We used the trained encoding models of each NSD subject and area to generate in silico fMRI responses for the 73,000 images from NSD (depicting complex natural scenes consisting of several or no objects appearing at different locations), as well as for the 50,000 images from the ImageNet 2012 challenge validation split<sup>31</sup> and for the 26,107 images from THINGS<sup>32</sup> (depicting single objects presented centrally on natural backgrounds).

We used the trained encoding models of each VIR subject and area to generate in silico fMRI responses for the 73,000 images from NSD. Since VIR does not include EBA and RSC area definitions, we did not use VIR for the RNC analyses on high-level visual areas.

## Univariate RNC

The goal of univariate relational neural control (RNC) was to search the 73,000 NSD images for images that controlled (i.e., aligned or disentangled) the in silico univariate fMRI responses – that is, averaged responses across all voxels of a given given area – of each pairwise comparison of areas.

### Univariate RNC baseline

For each area, we randomly selected a batch of 25 images (out of all 73,000 NSD images), fed them into the given area's encoding model, and averaged the corresponding in silico univariate fMRI responses across the 25 images, resulting in a single score corresponding to the mean fMRI response for that image batch. By repeating this step 1 million times, we created the univariate RNC null distribution and selected the 25 images from the batch with scores closest to the null distribution mean. The mean univariate response score across these 25 images provided the area-wise univariate response baseline against which we tested the neural control scores from the controlling images selected through univariate RNC.

### Univariate RNC algorithm

We fed the 73,000 NSD images to the trained encoding models of two areas, and averaged the resulting in silico fMRI responses across voxels, obtaining a one-dimensional univariate response vector of length 73,000 for each of the two areas. We then either summed (alignment) or subtracted (disentanglement) the univariate response vectors of the two areas and ranked the resulting sum/difference scores. Finally, we kept the 25 controlling images that yielded the highest or lowest (depending on the neural control condition) scores and, at the same time, resulted in in silico univariate fMRI responses higher or lower than the areas' univariate response baselines by a margin of at least 0.04.

This resulted in four sets of 25 controlling images, each set corresponding to a different neural control condition. The controlling images from the sum vector led to two neural control

conditions in which the two areas have aligned univariate responses (i.e., images that either drive or suppress the responses of both areas), whereas the controlling images from the difference vector led to two neural control conditions in which the two areas have disentangled univariate responses (i.e., images that drive the responses of one area while suppressing the responses of the other area, or vice versa) (the univariate RNC algorithm is visualized in **Supplementary Figure 4**).

To ascertain that the resulting representational relationships reflect properties of visual processing, rather than biases of specific datasets, we additionally performed two tests. First, we applied univariate RNC on the 50,000 ImageNet or 26,107 THINGS images and corresponding in silico fMRI responses, generated through encoding models trained on NSD. Second, we applied univariate RNC on the 73,000 NSD images and corresponding in silico fMRI responses, generated through encoding models trained on VIR.

### Subject-wise cross-validation

We used subject-wise leave-one-out cross-validation to evaluate the univariate RNC solutions (as well as the baseline) by selecting the controlling images based on the in silico univariate fMRI responses averaged across seven subjects and evaluating them on the in silico univariate fMRI responses of the left out subject. We repeated cross-validation for each unique set of seven subjects, resulting in eight cross-validated solutions.

### Univariate RNC multidimensional scaling analysis

We applied multidimensional scaling (MDS)<sup>48</sup> on the in silico univariate fMRI responses of eight early-, mid-, and high-level visual areas (V1, V2, V3, V4, EBA, FFA, PPA, RSC). We started by computing the in silico fMRI univariate responses of each subject and area for  $N$  images (where  $N$  corresponds to all 73,000 NDS images, or to the 25 controlling images from a chosen univariate RNC control condition). Next, we averaged these univariate responses across subjects, resulting in an array of shape (8 areas  $\times$   $N$  images). Finally, we reduced the dimensionality of this array with MDS, resulting in a reduced array of shape (8 areas  $\times$  2 dimensions). We used scikit-learn's<sup>90</sup> MDS implementation with `n_components=2`, `metric=True`, `n_init=10`, `max_iter=1000`, `verbose=0`, `eps=0.001`, `n_jobs=None`, `dissimilarity='euclidean'`.

### Generative univariate RNC

Generative univariate RNC used an image generator and genetic optimization to generate stimulus images leading to aligned or disentangled in silico univariate fMRI responses for V1 and V4, while at the same time being as simple as possible, thus isolating the controlling visual features of interest.

We began by creating 1,000 random latent vectors from a standard normal distribution (each vector being 4,096-dimensional). We gave the latent vectors as input to DeePSiM<sup>37</sup>, a pre-trained generative adversarial network (GAN), which used them to generate 1,000 images, and clamped the output image pixel values to the valid RGB range [0 255]. We stored the PNG compression file sizes of these images, as well as their latent vectors, for later use during the genetic optimization.

We then fed the generated images to the V1 and V4 trained encoding models of all subjects, and averaged the resulting *in silico* fMRI responses across both voxels and subjects, obtaining a one-dimensional univariate response vector of length 1,000, for both V1 and V4. We stored the univariate responses of both areas for later use during the genetic optimization. Depending on the univariate RNC neural control condition being optimized, we then either summed or subtracted the univariate response vectors of the two areas and stored these sum or difference scores.

Next, we fed the latent vectors, the PNG compression file sizes, the V1 and V4 univariate responses, and the sum/difference scores to a genetic optimization algorithm<sup>38,39</sup>, which used these inputs to create a new generation of latent vectors. Optimization consisted of two phases. At first, the objective of the genetic optimization was to create new latent vectors leading to images more likely to result in univariate responses closer to threshold level. Once the univariate response threshold was reached, the objective switched to creating new latent vectors leading to images more likely to have lower PNG compression file sizes, while at the same time keeping the univariate responses above threshold.

This resulted in a new batch of 1,000 latent vectors, which we fed to the GAN for the second optimization generation, repeating the same steps. After 500 genetic optimization generations, we obtained a single image (i.e., the best performing image from the last genetic optimization generation) that optimally controlled univariate neural responses following one of four univariate RNC neural control conditions, while at the same time being as simple as possible (i.e., having a low PNG compression file size). We optimized the images for the four neural control conditions independently of each other (the generative univariate RNC algorithm is visualized in **Supplementary Figure 8**).

For each neural control condition we ran 10 independent evolutions, each based on a different random seed. The random seed determined the initial latent vectors, as well as the new latent vectors produced by the genetic optimization, resulting in 10 genetically optimized images for each control condition.

For each area, the univariate response threshold consisted in the area's univariate response baseline plus a margin of 0.6 (for control conditions driving the area's response) or -0.6 (for control conditions suppressing the area's response).

### Genetic optimization algorithm

The genetic optimization assigned a global score to each latent vector. If a latent vector led to univariate responses below threshold level for at least one of the two areas, its global score consisted in the corresponding sum/difference score, plus a large penalty ( $10^{10}$ ). If a latent vector led to univariate responses above threshold level for both V1 and V4, its global score consisted in the PNG compression file size of the corresponding image. Since the penalty value was constant, the global scores of several latent vectors leading to below-threshold univariate responses were ranked based on the corresponding sum/difference scores of these vectors. Thus, until the threshold was reached, the latent vectors were optimized to result in better sum/difference scores. Because the sum/difference scores were based on the univariate responses, this in turn led to univariate responses progressively closer to threshold level. Furthermore, since the penalty was always larger than the PNG file sizes, the global

scores of latent vectors leading to above-threshold univariate responses always ranked better than the global scores of latent vectors leading to below-threshold univariate responses. This ensured that the optimization would favor latent vectors leading to univariate responses above threshold.

We transformed the global scores of all latent vectors into probabilities through z-scoring, scaling by a factor of 0.5, and passing the resulting values through a softmax function. The genetic optimization algorithm used these probabilities to create a new generation of latent vectors, while balancing exploitation and exploration. Exploitation involved keeping (untouched) the 250 latent vectors with highest probability scores (i.e., the latent vectors leading to either univariate responses closest to threshold or lowest PNG compression file sizes). Exploration involved creating 750 new children latent vectors from recombinations between two parent latent vectors from the current generation, where the likelihood of each latent vector being a parent was determined by its probability score. The two parents contributed unevenly to any one child: 75%/25% of the child latent vector came from the parent latent vector with highest/lowest probability scores, respectively. Finally, during recombination, each of the 4,096 components of a child latent vector had a 0.25 probability of being mutated, with mutations drawn from a 0-centered Gaussian with standard deviation 0.75.

## Multivariate RNC

The goal of multivariate relational neural control (RNC) was to search the 73,000 NSD images for images that controlled (i.e., aligned or disentangled) the in silico multivariate fMRI responses – that is, the population response pattern of all voxels of a given area – of each pairwise comparison of areas.

### Multivariate RNC baseline

For each pairwise comparison of areas, we randomly selected a batch of 50 images (out of all 73,000 NSD images), used the encoding models to generate the corresponding in silico fMRI responses, transformed these in silico responses into RSMs, and used representational similarity analysis (RSA)<sup>25</sup> to compare the RSMs of the two areas (using Pearson's correlation), resulting in one score for the image batch. By repeating this step 1 million times, we created the multivariate RNC null distribution, and selected the 50 images from the batch with scores closest to the null distribution mean. The RSA score of these 50 images provided the baseline against which we tested the neural control scores from multivariate RNC.

### Multivariate RNC algorithm

The multivariate RNC was based on a genetic optimization<sup>38,39,42,43</sup> which, through 2,000 generations, selected images that best aligned or disentangled the in silico multivariate fMRI responses.

We started by creating 2,400 random batches of 50 images from the 73,000 NSD images, with no repeating image within each batch. We fed these image batches to the trained encoding models of two given areas, and transformed the resulting in silico fMRI responses

into representational similarity matrices (RSMs)<sup>25</sup>, resulting in one 50 × 50 image RSM for each of the 2,400 image batches, and each of the two areas. We then compared the RSMs of each image batch between the two areas using Pearson's correlation, obtained one correlation score (*r*) for each image batch, and ranked these correlation scores. To align the two areas, we kept the 200 image batches with highest correlation scores (i.e., images most similarly represented by the two areas), whereas to disentangle them, we kept the 200 image batches with lowest absolute correlation scores (i.e., images most differently represented by the two areas). Finally, we used these 200 highest/lowest ranked image batches as input to a genetic optimization algorithm, which used them to create 2,400 image batches, while balancing exploitation and exploration. Exploitation involved creating five mutated versions for each of the 200 image batches. In each version, a different number of images (1, 5, 12, 25, and 38) was randomly replaced with other images out of the 73,000 NSD images, while ensuring that no image repeated within the same batch. This increased the image batches to 1,200 (200 best batches + 200 best batches × 5 mutated versions = 1,200 batches). Exploration involved creating another 1,200 new random batches which, together with the 1,200 batches from the exploitation step, amounted to 2,400 batches of 50 images. During the second optimization generation, we once again fed these 2,400 image batches to the encoding models and repeated the same steps.

We ran 2,000 genetic optimization generations and selected the best performing image batch from the last generation. This resulted in one of two sets of 50 controlling images, each set corresponding to a different neural control condition (the image batches from the two neural control conditions were optimized independently of each other). The controlling images from the ranked correlation vector led to an alignment of multivariate responses in the two areas (i.e., images leading to high Pearson's *r* scores for the two areas), whereas the controlling images from the absolute ranked correlation vector led to a disentanglement of multivariate responses in the two areas (i.e., images leading to low absolute Pearson's *r* scores for the two areas) (the multivariate RNC algorithm is visualized in **Supplementary Figure 11**).

To ascertain that the resulting representational relationships reflect properties of visual processing, rather than biases of specific datasets, we additionally performed two tests. First, we applied multivariate RNC on the 50,000 ImageNet or 26,107 THINGS images and corresponding in silico fMRI responses, generated through encoding models trained on NSD. Second, we applied multivariate RNC on the 73,000 NSD images and corresponding in silico fMRI responses, generated through encoding models trained on VIR.

## Subject-wise cross-validation

We used subject-wise leave-one-out cross-validation to evaluate the multivariate RNC solutions (as well as the baseline) by selecting the controlling images based on the in silico fMRI RSMs averaged across seven subjects, and evaluating them on the in silico fMRI RSM of the left out subject. We repeated cross-validation for each unique set of seven subjects, resulting in eight cross-validated solutions.

## Multivariate RNC multidimensional scaling analysis

We applied multidimensional scaling (MDS)<sup>48</sup> on the in silico multivariate fMRI responses of eight early-, mid-, and high-level visual areas (V1, V2, V3, V4, EBA, FFA, PPA, RSC). We started by computing the in silico fMRI RSMs of each subject and area for  $N$  images (where  $N$  corresponds to all 73,000 NDS images, or to the 50 controlling images from a chosen multivariate RNC control condition). Next, we averaged these RSMs across subjects, and vectorized the lower triangle entries of the averaged RSMs, resulting in an array of shape (8 areas  $\times$   $M$  RSM lower triangle entries). Finally, we reduced the dimensionality of this array with MDS, resulting in a reduced array of shape (8 areas  $\times$  2 dimensions). We used scikit-learn's<sup>90</sup> MDS implementation with `n_components=2`, `metric=True`, `n_init=10`, `max_iter=1000`, `verbose=0`, `eps=0.001`, `n_jobs=None`, `dissimilarity='euclidean'`.

## Definition of lower and upper visual field voxels

For area V1, we selected voxels tuned to the lower and upper portions of the visual field based on the V1d (i.e., V1 dorsal) and V1v (i.e., V1 ventral) NSD delineations, respectively. For area V4, we used the polar angle maps from the NSD population receptive field (pRF) experiment to manually divide the area into voxels tuned to the lower and upper portions of the visual field.

## fMRI experiments

### Participants

Six healthy adults (mean age 25.83 years, SD = 4.67; 4 female, 2 male) participated; all had normal or corrected-to-normal vision. No statistical methods were used to pre-determine sample sizes but our sample sizes are similar to those reported in previous publications<sup>27,57</sup>. All subjects provided written informed consent and received monetary reimbursement (at the university rate of 12 euros per hour). Procedures were approved by the ethical committee of the Department of Education and Psychology at Freie Universität Berlin and were in accordance with the Declaration of Helsinki.

### Stimuli

During the fMRI experiments, we presented subjects with 150 images from the V1 vs. V4 univariate RNC solutions (25 images from each of the two aligning conditions, 25 images from each of the two disentangling conditions, 25 images from V1's baseline, and 25 images from V4's baseline) (**Fig. 3a**), and 150 images from the V1 vs. V4 multivariate RNC solutions (50 images from aligning condition, 50 images from disentangling condition, and 50 images from the baseline) (**Fig. 5a**). All images were sized 425 pixels  $\times$  425 pixels  $\times$  3 RGB channels.

To prevent confounds driven by luminance, we matched each image's mean luminance (i.e., its luminance across all pixels) to the luminance of the stimuli presentation screen background (a uniform gray screen with an RGB value of [127 127 127]), using the "ImageEnhance" function from the Pillow Python package (<https://python-pillow.org/>).

## Experimental paradigm

### Main experiment

Each subject underwent two fMRI data collection sessions. Each session consisted of multiple four-second trials, where an image was presented for two seconds, followed by two seconds of gray screen inter-stimulus interval (**Supplementary Figure 26a**). To ensure that subjects paid attention, we presented the RNC controlling images within an orthogonal target detection task where we asked subjects to report, through a button press, whenever a catch image containing the fictional character Buzz Lightyear appeared on the screen.

During the first session, we presented the 150 controlling images from univariate RNC, across 10 runs. Each run consisted of 109 four-second trials: it started with 3 blank trials (i.e., a gray screen where no image was presented), continued with a pseudo-randomized order of 90 univariate RNC image trials, 8 blank trials, and 4 catch trials (i.e., images containing Buzz Lightyear), and ended with 4 blank trials. Across all 10 runs, this resulted in 6 presentation repeats for each of the 150 univariate RNC controlling images.

During the second session, we presented the 150 controlling images from multivariate RNC, across 12 runs. Each run consisted of 121 four-second trials: it started with 3 blank trials, continued with a pseudo-randomized order of 100 multivariate RNC image trials, 9 blank trials, and 5 catch trials (i.e., images containing Buzz Lightyear), and ended with 4 blank trials. Across all 12 runs, this resulted in 8 presentation repeats for each of the 150 multivariate RNC controlling images.

All images were presented centrally, with a horizontal and vertical visual angle of  $8.4^\circ$ , against a gray background with an RGB value of [127, 127, 127]. A small semi-transparent red fixation dot with a black border ( $0.2^\circ \times 0.2^\circ$ , 50% opacity) was present at the center of the images throughout the entirety of both sessions, and we asked subjects to maintain central fixation throughout the experiment. We controlled stimulus presentation using the Psychtoolbox<sup>91</sup>, and recorded fMRI responses during both experimental sessions.

### pRF experiment

We ran the 'multibar' pRF experiment used in the NSD<sup>27</sup>, which is an adaptation of the pRF experiment used in the Human Connectome Project 7T Retinotopy Dataset<sup>49</sup>. Stimuli consisted of slowly moving apertures filled with a dynamic colorful texture, and involved bars sweeping in multiple directions (same as RETBAR in the Human Connectome Project 7T Retinotopy Dataset) (**Supplementary Figure 26b**). Apertures and textures were updated at a rate of 16 Hz. Stimuli filled a circular region with diameter  $12^\circ$ . Each run lasted 300 seconds, and included blank periods. Throughout stimulus presentation, a small semi-transparent dot (with diameter  $0.2^\circ$ ) was present at the center of the stimuli. The color of the central dot switched randomly to one of three colors (black, white or red) every 1 to 5 seconds. Subjects were instructed to maintain fixation on the dot and to press a button whenever the dot changed color. To further aid fixation, a semi-transparent fixation grid was superimposed on the stimuli and was present throughout the experiment<sup>92</sup>. For each subject, we collected three runs of the pRF experiment, at the beginning of the first fMRI session.

## fMRI

### Acquisition

We collected MRI data using a Siemens Magnetom Prisma Fit 3T system (Siemens Medical Solutions, Erlangen, Germany) with a 64-channel head coil.

Anatomical scans were acquired during each recording session using a standard T1-weighted sequence (TR = 1.9 s, TE = 3.22 ms, number of slices 176, FOV = 225 mm, voxel size 1.0 mm isotropic, flip angle 8°).

Functional images were acquired using gradient-echo EPI at 2.5 mm isotropic resolution with partial brain coverage (TR = 1 s, TE = 33 ms, number of axial slices 39, matrix size 82 × 82, FOV = 205 mm, flip angle 70°, acquisition order interleaved, inter-slice gap 0.25 mm, multi-band slice acceleration factor 3). The acquisition volume fully covered the occipital lobe.

Dual-echo fieldmaps were acquired during each recording session (TR = 0.4 s, TE<sub>1</sub> = 4.92 ms, TE<sub>2</sub> = 7.38 ms, number of slices 38, voxel size 3 mm isotropic, matrix size = 66 × 66, FOV = 198 mm, flip angle 60°).

### Preprocessing

We preprocessed the fMRI data using SPM12 (<https://www.fil.ion.ucl.ac.uk/spm/software/spm12/>). Preprocessing steps included realigning all functional images to the first image of each run, slice-time correction, field map correction, and co-registration of the functional images to the anatomical image of the first recording session.

### pRF mapping

The population receptive field (pRF) mapping analysis was run using the prf-workflow package (<https://github.com/mayajas/prf-workflow>), with the model fitting done with the pRFpy package (v0.1.0; <https://github.com/VU-Cog-Sci/prfpy>). The preprocessed functional data of the three pRF runs were projected to the Freesurfer reconstruction of the white matter cortical surface of the given subject. The surface-projected signals at each surface mesh vertex were detrended to account for linear drifts, bandpass filtered (0.01 to 0.1 Hz) and z-scored over time. The signals from the three pRF runs were then averaged together. We fit an isotropic 2D Gaussian pRF model to the data at each cortical surface vertex, with an initial coarse grid fit followed by a fine iterative fit, to optimize the parameters that define pRF size and the location (x, y) in Cartesian coordinates in visual space that the underlying population of neurons responds to.

The optimized location parameters were transformed to eccentricities and polar angle maps, which we then used to manually delineate visual regions of interest (ROIs) V1 and V4. Delineations were constrained to the maximum stimulus eccentricity of the controlling images (i.e., 8.4° of visual angle) based on the eccentricity map, while the visual areas were identified based on reversals in the polar angle map. To ensure specificity the visual area delineations were drawn conservatively, with the dorsal/ventral boundaries drawn just ventrally/dorsally of the corresponding polar angle reversal (**Supplementary Fig 26c**).



## GLM

We used GLMsingle<sup>93</sup> to estimate single-trial beta responses (i.e., BOLD response amplitudes evoked by each image trial) of the preprocessed fMRI data from the main experiment. GLMsingle provides single-trial beta estimates following three steps. First, for each voxel, a custom hemodynamic response function (HRF) is identified from a library of candidate functions. Second, cross-validation is used to derive a set of noise regressors from voxels that have negligible amounts of BOLD variance related to the experiment (using an  $R^2$  threshold). Third, to improve the stability of beta estimates for closely spaced trials, betas are regularized on a voxel-wise basis using ridge regression. The resulting betas indicate the percent of BOLD signal change evoked by single image trials, with respect to a baseline corresponding to the absence of a stimulus (i.e., a gray screen with no image presented). We applied GLMsingle with default parameters, independently to the preprocessed fMRI responses of each subject, session, and area (i.e., independently for the voxels of V1 and V4).

## Z-scoring and voxel selection

For consistency with the in silico fMRI data, here too we z-scored the beta responses (from GLMsingle) of each voxel across all trials of each session and computed the noise ceiling signal-to-noise ratio (ncsnr) of each voxel. For further analyses, we retained only those voxels with ncsnr scores above 0.4. The more liberal ncsnr threshold (compared to the in silico fMRI data analyses) comes from the fact that not all recorded subjects and areas consisted in voxels with ncsnr scores above 0.5. We computed the ncsnr independently for the data of the two recording sessions, that is, independently for the fMRI responses for the univariate and multivariate RNC images. This resulted in a different amount of retained voxels between the two experimental sessions, which can be seen in **Supplementary Tables 4-5**.

## Statistical testing

We assessed statistical significance using population prevalence testing<sup>94,95</sup>, which is well suited to determine significance of an effect at the level of the population when analyzing small samples of intensely scanned subjects. Population prevalence testing is a two-level procedure. At the first level, significance is established independently within each subject. At the second level, the binary results from the first level (i.e., the counts of significant subjects) are used to estimate the probability of this happening by chance, under the null hypothesis of no effect in any member of the population, thus providing a population-level inference. Following we describe these two levels in detail.

At the first level, we established significance independently within each subject using non-parametric permutation tests. Each test consisted in: computing the statistic of interest (i.e., the observed statistic); creating the null distribution of the observed statistic by recomputing it using 100,000 different random permutations of the data; quantifying the  $p$ -value as the proportion of permutations where the randomized statistic is as extreme or more extreme than the observed statistic; controlling familywise error rate by applying (non-negative) Benjamini/Hochberg correction<sup>96</sup> to the resulting  $p$ -values; assigning significance to subjects with corrected  $p$ -values below 0.05. In the encoding models noise analysis tests the null hypothesis was that the noise-ceiling-normalized explained variance

scores of the different predictors were equal, we permuted the encoding accuracy scores over fMRI voxels and predictors, and we corrected the  $p$ -values over 2 tests for each area. In the univariate RNC analysis tests the null hypothesis was that the univariate responses for the controlling and baseline images were equal, we permuted the univariate responses across image conditions, and we corrected the  $p$ -values over 8 tests for each pairwise comparison of areas. In the univariate RNC cortical distance analysis tests the null hypothesis was that the absolute differences between the baseline univariate responses and the univariate responses for controlling images from different stepwise area distances were equal, we permuted the univariate responses across areas, and we corrected the  $p$ -values over 4 tests (one for each neural control condition). In the multivariate RNC analysis tests the null hypothesis was that the RSA scores for the controlling and baseline images were equal, we permuted the multivariate responses across image conditions, and we corrected the  $p$ -values over 2 tests for each pairwise comparison of areas. In the multivariate RNC cortical distance analysis tests the null hypothesis was that the absolute differences between the baseline RSA scores and the RSA scores for controlling images from different stepwise area distances were equal, we permuted the multivariate responses across areas and image conditions, and we corrected the  $p$ -values over 2 tests (one for each neural control condition). In the multivariate RNC retinotopy analysis tests the null hypothesis was that the univariate responses of voxels tuned to the lower and upper portions of the visual field were equal, we permuted the data across ventral and dorsal voxels, and we corrected the  $p$ -values over 2 tests for each area. In the univariate RNC categorical selectivity analysis tests the null hypothesis was that the absolute differences between the baseline univariate responses and the univariate responses for controlling images from areas within or between categorical selectivity groups were equal, we permuted the univariate responses across areas, and we corrected the  $p$ -values over 4 tests (one for each neural control condition). In the multivariate RNC categorical selectivity analysis tests the null hypothesis was that the absolute differences between the baseline RSA scores and the RSA scores for controlling images from areas within or between categorical selectivity groups were equal, we permuted the univariate responses across areas and image conditions, and we corrected the  $p$ -values over 2 tests (one for each neural control condition).

At the second level, we used the cumulative density function of the binomial distribution of within-participant significance to estimate the probability of observing significant subjects by chance, if there was no effect in any member of the population:

$$p = 1 - CDF(k, n, a = 0.05)$$

where  $CDF$  is the cumulative density function of the binomial distribution,  $k$  is the number of significant subjects,  $n$  is the total number of subjects (8 or 7 subjects for tests on the in silico fMRI responses from encoding models trained on NSD and VIR, respectively; 6 subjects for tests on the in vivo fMRI responses from the fMRI experiments), and  $a$  is the probability of success in each trial under the null hypothesis. Finally, we assigned statistical significance at the population-level for probabilities of  $p < 0.05$ .

To calculate the confidence intervals of each statistic, we created 100,000 bootstrapped samples by sampling the subject-specific results with replacement. This yielded empirical distributions of the results, from which we derived the 95% confidence intervals.

## Data availability

The univariate and multivariate RNC algorithms were applied on in silico fMRI responses generated using the Neural Encoding Simulation Toolkit (<https://github.com/gifale95/NEST>).

The controlling images for all pairwise comparisons of areas, along with the in vivo fMRI responses for the V1 vs. V4 comparison controlling images, are available on OpenNeuro (<https://openneuro.org/datasets/ds005503>).

## Code availability

The code to reproduce all the paper results is available on GitHub (<https://github.com/gifale95/RNC>). To promote RNC adoption, the GitHub repository also includes Colab tutorials where users can interactively implement univariate and multivariate RNC on in silico fMRI responses of areas spanning the entire visual cortex for ~150,000 naturalistic images.

## Acknowledgments

A.T.G. is supported by a PhD fellowship of the Einstein Center for Neurosciences. M.A.J. is supported by the Horizon Europe Framework Programme (HORIZON-MSCA-2021-PF-01, grant number: 101064539). R.M.C. is supported by German Research Council (DFG) grants (CI 241/1-1, CI 241/1-3, CI 241/1-7, INST 272/297-1), the European Research Council (ERC) starting grant (ERC-StG-2018-803370), and the ERC Consolidator grant (ERC-CoG-2024101123101). We thank the HPC Service of FUB-IT, Freie Universität Berlin, for computing time (DOI: <http://dx.doi.org/10.17169/refubium-26754>). We thank Kendrick Kay for helpful feedback, and Ian Charest for help with the Natural Scenes Dataset.

## Author contributions

A.T.G. and R.M.C. designed research. A.T.G., J.J.D.S. and M.A.J. acquired fMRI data. A.T.G. and J.J.D.S. preprocessed fMRI data. A.T.G. and M.A.J. performed population receptive field analyses. A.T.G. modeled and analyzed data. A.T.G. and R.M.C. interpreted results. A.T.G. prepared figures. A.T.G. drafted the manuscript. A.T.G., J.J.D.S., M.J. and R.M.C. edited and revised the manuscript. All authors approved the final version of the manuscript.

## Competing interests

The authors declare no competing interests.

# References

1. Grill-Spector, K. & Malach, R. The Human visual Cortex. *Annu. Rev. Neurosci.* **27**, 649–677 (2004).
2. Van Essen, D. C., Anderson, C. H. & Felleman, D. J. Information Processing in the Primate Visual System: An Integrated Systems Perspective. *Science* **255**, 419–423 (1992).
3. Barlow, H. B. Why have multiple cortical areas? *Vision Res.* **26**, 81–90 (1986).
4. Bullier, J. Integrated model of visual processing. *Brain Res. Rev.* **36**, 96–107 (2001).
5. Felleman, D. J. & Van Essen, D. C. Distributed hierarchical processing in the primate cerebral cortex. *Cereb. Cortex N. Y. N* **1991** **1**, 1–47 (1991).
6. Kravitz, D. J., Saleem, K. S., Baker, C. I. & Mishkin, M. A new neural framework for visuospatial processing. *Nat. Rev. Neurosci.* **12**, 217–230 (2011).
7. Maunsell, J. H. R. & Newsome, W. T. Visual Processing in Monkey Extrastriate Cortex. *Annu. Rev. Neurosci.* **10**, 363–401 (1987).
8. Milner, A. D. & Goodale, M. A. Two visual systems re-viewed. *Neuropsychologia* **46**, 774–785 (2008).
9. deCharms, R. C. & Zador, A. Neural Representation and the Cortical Code. *Annu. Rev. Neurosci.* **23**, 613–647 (2000).
10. Ballard, D. H. On the Function of Visual Representation. in *Vision and Mind* (eds. Noë, A. & Thompson, E.) 459–480 (The MIT Press, 2002). doi:10.7551/mitpress/7111.003.0020.
11. Barack, D. L. & Krakauer, J. W. Two views on the cognitive brain. *Nat. Rev. Neurosci.* **22**, 359–371 (2021).
12. DiCarlo, J. J., Zoccolan, D. & Rust, N. C. How Does the Brain Solve Visual Object Recognition? *Neuron* **73**, 415–434 (2012).
13. Kriegeskorte, N. & Diedrichsen, J. Peeling the Onion of Brain Representations. *Annu. Rev. Neurosci.* **42**, 407–432 (2019).
14. Martin, K. A. C. A Brief History of the “Feature Detector”. *Cereb. Cortex* **4**, 1–7 (1994).
15. Hubel, D. H. & Wiesel, T. N. Receptive fields and functional architecture of monkey striate cortex. *J. Physiol.* **195**, 215–243 (1968).
16. Kanwisher, N. Functional specificity in the human brain: A window into the functional architecture of the mind. *Proc. Natl. Acad. Sci.* **107**, 11163–11170 (2010).
17. Van Den Heuvel, M. P. & Hulshoff Pol, H. E. Exploring the brain network: A review on resting-state fMRI functional connectivity. *Eur. Neuropsychopharmacol.* **20**, 519–534 (2010).
18. Naselaris, T., Kay, K. N., Nishimoto, S. & Gallant, J. L. Encoding and decoding in fMRI. *NeuroImage* **56**, 400–410 (2011).
19. Wu, M. C.-K., David, S. V. & Gallant, J. L. Complete Functional Characterization Of Sensory Neurons By System Identification. *Annu. Rev. Neurosci.* **29**, 477–505 (2006).
20. Yamins, D. L. K. & DiCarlo, J. J. Using goal-driven deep learning models to understand sensory cortex. *Nat. Neurosci.* **19**, 356–365 (2016).
21. Davis, T. *et al.* What do differences between multi-voxel and univariate analysis mean? How subject-, voxel-, and trial-level variance impact fMRI analysis. *NeuroImage* **97**, 271–283 (2014).
22. Hebart, M. N. & Baker, C. I. Deconstructing multivariate decoding for the study of brain function. *NeuroImage* **180**, 4–18 (2018).
23. Kanwisher, N., McDermott, J. & Chun, M. M. The Fusiform Face Area: A Module in

- Human Extrastriate Cortex Specialized for Face Perception. *J. Neurosci.* **17**, 4302–4311 (1997).
24. Haynes, J.-D. & Rees, G. Decoding mental states from brain activity in humans. *Nat. Rev. Neurosci.* **7**, 523–534 (2006).
  25. Kriegeskorte, N., Mur, M. & Bandettini, P. A. Representational similarity analysis - connecting the branches of systems neuroscience. *Front. Syst. Neurosci.* **2**, (2008).
  26. Mur, M., Bandettini, P. A. & Kriegeskorte, N. Revealing representational content with pattern-information fMRI—an introductory guide. *Soc. Cogn. Affect. Neurosci.* **4**, 101–109 (2009).
  27. Allen, E. J. *et al.* A massive 7T fMRI dataset to bridge cognitive neuroscience and artificial intelligence. *Nat. Neurosci.* **25**, 116–126 (2022).
  28. Gifford, A. T., Cichy, R. M., Naselaris, T. & Kay, K. A 7T fMRI dataset of synthetic images for out-of-distribution modeling of vision. Preprint at <https://doi.org/10.48550/ARXIV.2503.06286> (2025).
  29. Gu, Z. *et al.* NeuroGen: Activation optimized image synthesis for discovery neuroscience. *NeuroImage* **247**, 118812 (2022).
  30. Schmolesky, M. T. *et al.* Signal Timing Across the Macaque Visual System. *J. Neurophysiol.* **79**, 3272–3278 (1998).
  31. Russakovsky, O. *et al.* ImageNet Large Scale Visual Recognition Challenge. *Int. J. Comput. Vis.* **115**, 211–252 (2015).
  32. Hebart, M. N. *et al.* THINGS: A database of 1,854 object concepts and more than 26,000 naturalistic object images. *PLOS ONE* **14**, e0223792 (2019).
  33. Cheng, F. L. *et al.* Reconstructing visual illusory experiences from human brain activity. *Sci. Adv.* **9**, eadj3906 (2023).
  34. Foster, K. H., Gaska, J. P., Nagler, M. & Pollen, D. A. Spatial and temporal frequency selectivity of neurones in visual cortical areas V1 and V2 of the macaque monkey. *J. Physiol.* **365**, 331–363 (1985).
  35. Kay, K. N., Naselaris, T., Prenger, R. J. & Gallant, J. L. Identifying natural images from human brain activity. *Nature* **452**, 352–355 (2008).
  36. Kobatake, E. & Tanaka, K. Neuronal selectivities to complex object features in the ventral visual pathway of the macaque cerebral cortex. *J. Neurophysiol.* **71**, 856–867 (1994).
  37. Dosovitskiy, A. & Brox, T. Generating Images with Perceptual Similarity Metrics based on Deep Networks. in *Advances in Neural Information Processing Systems* vol. 29 (Curran Associates, Inc., 2016).
  38. Ponce, C. R. *et al.* Evolving Images for Visual Neurons Using a Deep Generative Network Reveals Coding Principles and Neuronal Preferences. *Cell* **177**, 999–1009.e10 (2019).
  39. Xiao, W. & Kreiman, G. XDream: Finding preferred stimuli for visual neurons using generative networks and gradient-free optimization. *PLOS Comput. Biol.* **16**, e1007973 (2020).
  40. Marin, M. M. & Leder, H. Examining Complexity across Domains: Relating Subjective and Objective Measures of Affective Environmental Scenes, Paintings and Music. *PLoS ONE* **8**, e72412 (2013).
  41. Mayer, S. & Landwehr, J. R. Quantifying visual aesthetics based on processing fluency theory: Four algorithmic measures for antecedents of aesthetic preferences. *Psychol. Aesthet. Creat. Arts* **12**, 399–431 (2018).
  42. Vaziri, S., Carlson, E. T., Wang, Z. & Connor, C. E. A Channel for 3D Environmental Shape in Anterior Inferotemporal Cortex. *Neuron* **84**, 55–62 (2014).

43. Yamane, Y., Carlson, E. T., Bowman, K. C., Wang, Z. & Connor, C. E. A neural code for three-dimensional object shape in macaque inferotemporal cortex. *Nat. Neurosci.* **11**, 1352–1360 (2008).
44. Wandell, B. A. & Winawer, J. Imaging retinotopic maps in the human brain. *Vision Res.* **51**, 718–737 (2011).
45. Downing, P. E., Jiang, Y., Shuman, M. & Kanwisher, N. A Cortical Area Selective for Visual Processing of the Human Body. *Science* **293**, 2470–2473 (2001).
46. Epstein, R. & Kanwisher, N. A cortical representation of the local visual environment. *Nature* **392**, 598–601 (1998).
47. Maguire, E. The retrosplenial contribution to human navigation: A review of lesion and neuroimaging findings. *Scand. J. Psychol.* **42**, 225–238 (2001).
48. Hout, M. C., Papesh, M. H. & Goldinger, S. D. Multidimensional scaling. *WIREs Cogn. Sci.* **4**, 93–103 (2013).
49. Benson, N. C. *et al.* The Human Connectome Project 7 Tesla retinotopy dataset: Description and population receptive field analysis. *J. Vis.* **18**, 23 (2018).
50. DiCarlo, J. J. & Cox, D. D. Untangling invariant object recognition. *Trends Cogn. Sci.* **11**, 333–341 (2007).
51. Marr, D. Visual information processing: the structure and creation of visual representations. *Philos. Trans. R. Soc. Lond. B Biol. Sci.* **290**, 199–218 (1980).
52. Lehky, S. R., Sejnowski, T. J. & Desimone, R. Predicting responses of nonlinear neurons in monkey striate cortex to complex patterns. *J. Neurosci.* **12**, 3568–3581 (1992).
53. Bashivan, P., Kar, K. & DiCarlo, J. J. Neural population control via deep image synthesis. *Science* **364**, eaav9436 (2019).
54. Walker, E. Y. *et al.* Inception loops discover what excites neurons most using deep predictive models. *Nat. Neurosci.* **22**, 2060–2065 (2019).
55. Ratan Murty, N. A., Bashivan, P., Abate, A., DiCarlo, J. J. & Kanwisher, N. Computational models of category-selective brain regions enable high-throughput tests of selectivity. *Nat. Commun.* **12**, 5540 (2021).
56. Wang, B. & Ponce, C. R. Tuning landscapes of the ventral stream. *Cell Rep.* **41**, 111595 (2022).
57. Gu, Z., Jamison, K., Sabuncu, M. R. & Kuceyeski, A. Human brain responses are modulated when exposed to optimized natural images or synthetically generated images. *Commun. Biol.* **6**, 1076 (2023).
58. Wang, T. *et al.* Large-scale calcium imaging reveals a systematic V4 map for encoding natural scenes. *Nat. Commun.* **15**, 6401 (2024).
59. Tuckute, G. *et al.* Driving and suppressing the human language network using large language models. *Nat. Hum. Behav.* 1–18 (2024) doi:10.1038/s41562-023-01783-7.
60. Jazayeri, M. & Afraz, A. Navigating the Neural Space in Search of the Neural Code. *Neuron* **93**, 1003–1014 (2017).
61. Perkel, D. H. & Bullock, T. H. Neural coding. *Neurosci. Res. Program Bull.* **6**, 221–348 (1968).
62. Dumoulin, S. O. & Wandell, B. A. Population receptive field estimates in human visual cortex. *NeuroImage* **39**, 647–660 (2008).
63. Park, S. & Chun, M. M. Different roles of the parahippocampal place area (PPA) and retrosplenial cortex (RSC) in panoramic scene perception. *NeuroImage* **47**, 1747–1756 (2009).
64. Vann, S. D., Aggleton, J. P. & Maguire, E. A. What does the retrosplenial cortex do? *Nat. Rev. Neurosci.* **10**, 792–802 (2009).




65. Rose, O. & Ponce, C. R. A concentration of visual cortex-like neurons in prefrontal cortex. *Nat. Commun.* **15**, 7002 (2024).
66. Xie, W. *et al.* Neuronal sequences in population bursts encode information in human cortex. *Nature* (2024) doi:10.1038/s41586-024-08075-8.
67. Jain, S., Vo, V. A., Wehbe, L. & Huth, A. G. Computational Language Modeling and the Promise of In Silico Experimentation. *Neurobiol. Lang.* **5**, 80–106 (2024).
68. Mathis, M. W., Perez Rotondo, A., Chang, E. F., Tolias, A. S. & Mathis, A. Decoding the brain: From neural representations to mechanistic models. *Cell* **187**, 5814–5832 (2024).
69. Gifford, A. T., Dwivedi, K., Roig, G. & Cichy, R. M. A large and rich EEG dataset for modeling human visual object recognition. *NeuroImage* **264**, 119754 (2022).
70. Hebart, M. N. *et al.* THINGS-data, a multimodal collection of large-scale datasets for investigating object representations in human brain and behavior. *eLife* **12**, e82580 (2023).
71. Lahner, B. *et al.* BOLD Moments: modeling short visual events through a video fMRI dataset and metadata. Preprint at <https://doi.org/10.1101/2023.03.12.530887> (2023).
72. Gifford, A. T. *et al.* The Algonauts Project 2023 Challenge: How the Human Brain Makes Sense of Natural Scenes. Preprint at <https://doi.org/10.48550/ARXIV.2301.03198> (2023).
73. Schrimpf, M. *et al.* Brain-Score: Which Artificial Neural Network for Object Recognition is most Brain-Like? Preprint at <https://doi.org/10.1101/407007> (2018).
74. Willeke, K. F. *et al.* The Sensorium competition on predicting large-scale mouse primary visual cortex activity. Preprint at <https://doi.org/10.48550/ARXIV.2206.08666> (2022).
75. Gifford, A. T. *et al.* The Algonauts Project 2025 Challenge: How the Human Brain Makes Sense of Multimodal Movies. Preprint at <https://doi.org/10.48550/ARXIV.2501.00504> (2025).
76. Markov, N. T. *et al.* Anatomy of hierarchy: Feedforward and feedback pathways in macaque visual cortex. *J. Comp. Neurol.* **522**, 225–259 (2014).
77. Lamme, V. A. F. & Roelfsema, P. R. The distinct modes of vision offered by feedforward and recurrent processing. *Trends Neurosci.* **23**, 571–579 (2000).
78. Gilbert, C. D. & Li, W. Top-down influences on visual processing. *Nat. Rev. Neurosci.* **14**, 350–363 (2013).
79. Groen, I. I. A. *et al.* Scene complexity modulates degree of feedback activity during object detection in natural scenes. *PLOS Comput. Biol.* **14**, e1006690 (2018).
80. Kar, K., Kubilius, J., Schmidt, K., Issa, E. B. & DiCarlo, J. J. Evidence that recurrent circuits are critical to the ventral stream’s execution of core object recognition behavior. *Nat. Neurosci.* **22**, 974–983 (2019).
81. Breitmeyer, B. G. & Ogmen, H. Recent models and findings in visual backward masking: A comparison, review, and update. *Percept. Psychophys.* **62**, 1572–1595 (2000).
82. Fahrenfort, J. J., Scholte, H. S. & Lamme, V. A. F. Masking Disrupts Reentrant Processing in Human Visual Cortex. *J. Cogn. Neurosci.* **19**, 1488–1497 (2007).
83. Maguire, J. F. & Howe, P. D. L. Failure to detect meaning in RSVP at 27 ms per picture. *Atten. Percept. Psychophys.* **78**, 1405–1413 (2016).
84. Lawrence, S. J., Norris, D. G. & De Lange, F. P. Dissociable laminar profiles of concurrent bottom-up and top-down modulation in the human visual cortex. *eLife* **8**, e44422 (2019).
85. St-Yves, G. & Naselaris, T. The feature-weighted receptive field: an interpretable encoding model for complex feature spaces. *NeuroImage* **180**, 188–202 (2018).
86. Guclu, U. & Van Gerven, M. A. J. Deep Neural Networks Reveal a Gradient in the Complexity of Neural Representations across the Ventral Stream. *J. Neurosci.* **35**,

- 10005–10014 (2015).
87. Horikawa, T. & Kamitani, Y. Generic decoding of seen and imagined objects using hierarchical visual features. *Nat. Commun.* **8**, 15037 (2017).
  88. Mehrer, J., Spoerer, C. J., Kriegeskorte, N. & Kietzmann, T. C. Individual differences among deep neural network models. *Nat. Commun.* **11**, 5725 (2020).
  89. Paszke, A. *et al.* PyTorch: An Imperative Style, High-Performance Deep Learning Library. Preprint at <https://doi.org/10.48550/ARXIV.1912.01703> (2019).
  90. Pedregosa, F. *et al.* Scikit-learn: Machine Learning in Python. (2012) doi:10.48550/ARXIV.1201.0490.
  91. Brainard, D. H. The Psychophysics Toolbox. *Spat. Vis.* **10**, 433–436 (1997).
  92. Schira, M. M., Tyler, C. W., Breakspear, M. & Spehar, B. The Foveal Confluence in Human Visual Cortex. *J. Neurosci.* **29**, 9050–9058 (2009).
  93. Prince, J. S. *et al.* Improving the accuracy of single-trial fMRI response estimates using GLMsingl. *eLife* **11**, e77599 (2022).
  94. Ince, R. A., Paton, A. T., Kay, J. W. & Schyns, P. G. Bayesian inference of population prevalence. *eLife* **10**, e62461 (2021).
  95. Ince, R. A. A., Kay, J. W. & Schyns, P. G. Within-participant statistics for cognitive science. *Trends Cogn. Sci.* **26**, 626–630 (2022).
  96. Benjamini, Y. & Hochberg, Y. Controlling the False Discovery Rate: A Practical and Powerful Approach to Multiple Testing. *J. R. Stat. Soc. Ser. B Stat. Methodol.* **57**, 289–300 (1995).



## Supplementary information

### In silico discovery of representational relationships across visual cortex

Alessandro T. Gifford<sup>1,2,3,\*</sup> , Maya A. Jastrzębowska<sup>1</sup> ,  
Johannes J.D. Singer<sup>1</sup> , Radosław M. Cichy<sup>1,2,3,4</sup> 

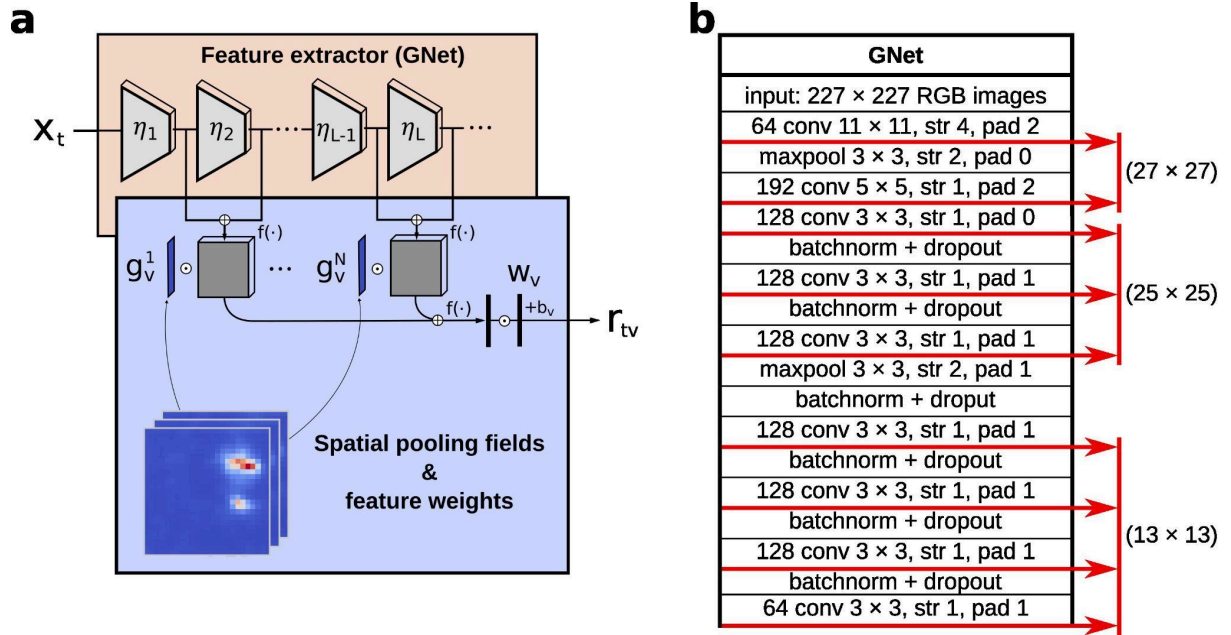
<sup>1</sup> Freie Universität Berlin, Berlin, Germany

<sup>2</sup> Einstein Center for Neurosciences Berlin, Berlin, Germany

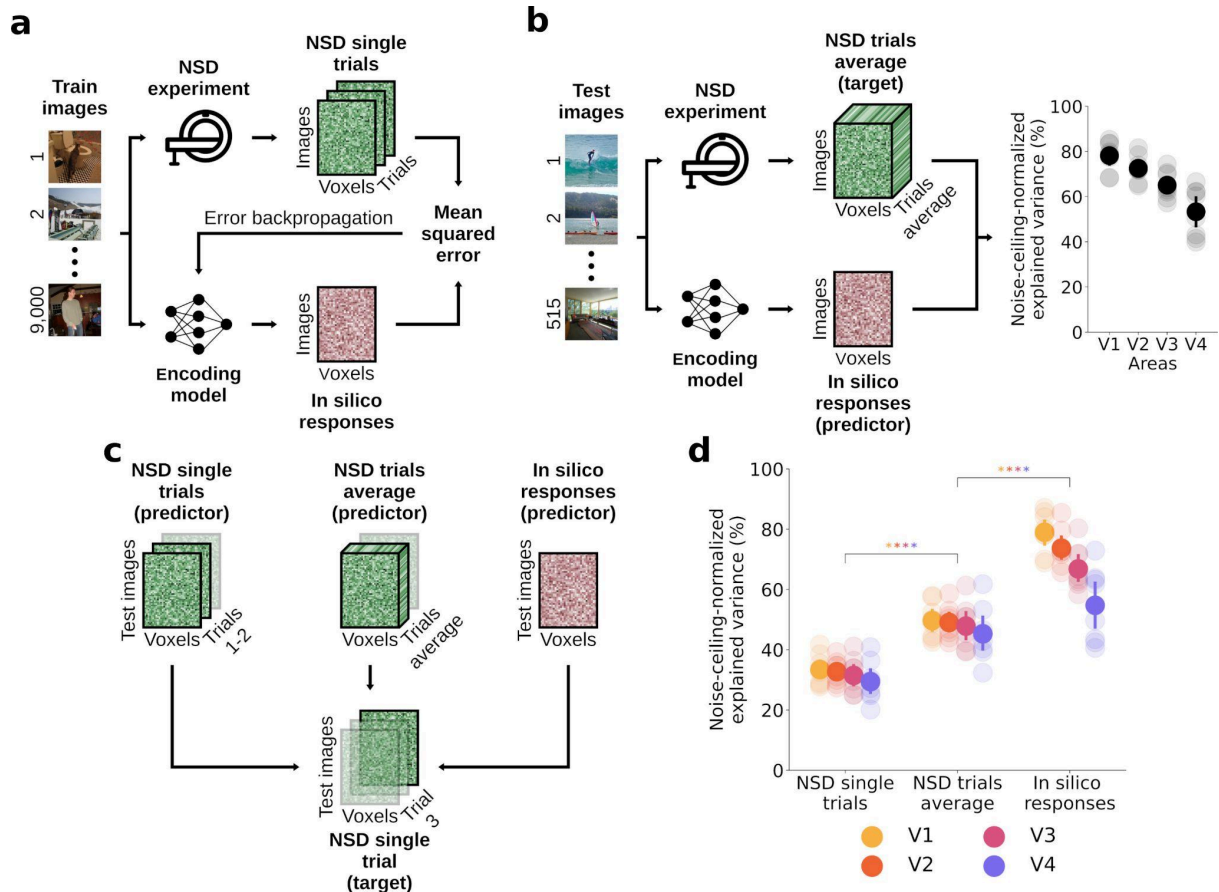
<sup>3</sup> Bernstein Center for Computational Neuroscience Berlin, Berlin, Germany

<sup>4</sup> Berlin School of Mind and Brain, Berlin, Germany

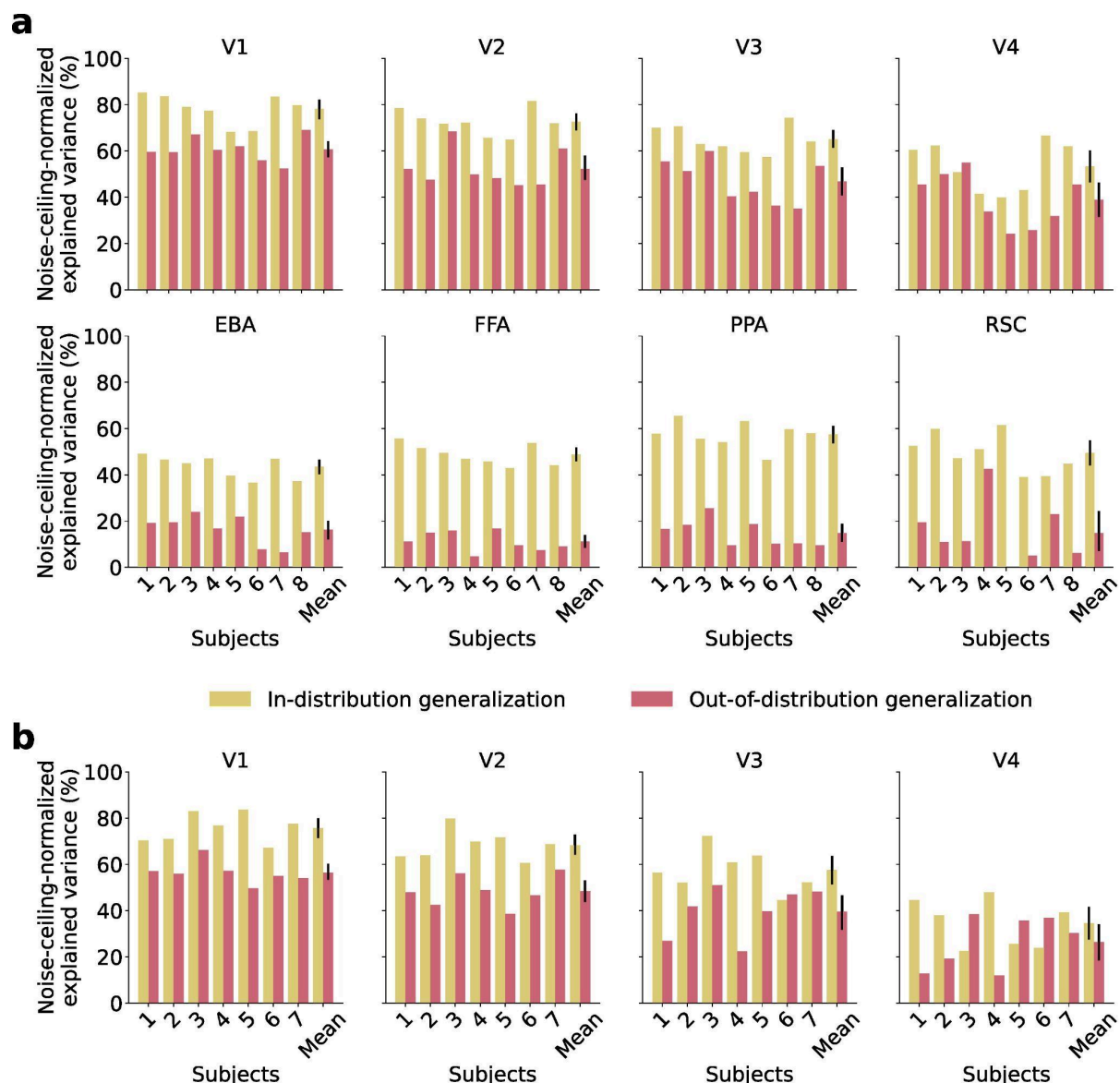
\* Correspondence: [alessandro.gifford@gmail.com](mailto:alessandro.gifford@gmail.com)



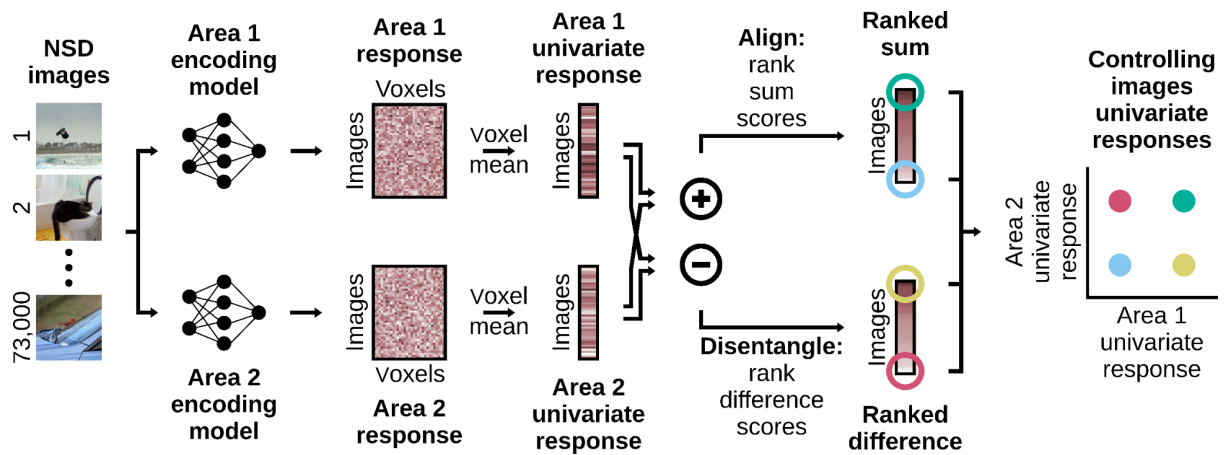
**Supplementary Figure 1 | Encoding model architecture (adapted from Allen et al., 2022<sup>1</sup>).** **a**, Illustration of an encoding model that predicts brain activity in a given voxel ( $r_{tv}$ ) in response to images ( $x_t$ ). Images are passed to nonlinear feature extractors (i.e., GNet),  $\eta_i$  (trapezoids), that output feature maps (grey cuboids). Feature maps are grouped, passed through an element-wise nonlinearity,  $f(\cdot)$ , and then multiplied pixel-wise by a spatial pooling field ( $g^1, \dots, g^N$  where superscripts index distinct groups of feature maps) that determines the region of visual space that drives voxel activity. The weighted pixel values in each feature map are then summed, reducing each feature map to a scalar value. These scalar values are concatenated across all feature maps, forming a single feature vector that is passed through another element-wise nonlinearity (left black rectangle) and then weighted by a set of feature weights,  $w$  (right black rectangle), to yield predicted voxel activity. The feature extractors  $\eta_i$  (i.e., GNet), the spatial pooling fields  $g^1, \dots, g^N$ , and the feature weights  $w$  are all optimized while training the encoding model to predict brain responses. **b**, GNet's architecture. GNet is a deep convolutional neural network consisting of convolutional layers (rows labeled 'conv'; values indicate feature depth and convolutional filter resolution; 'str' = filter stride, 'pad' = convolutional padding), max-pooling layers ('maxpool'), batch-normalization and weight-dropout layers ('batchnorm + dropout'). Feature maps in the convolutional layers (indicated by red arrows; resolution of the feature maps in parentheses) are used as predictors of brain activity in the context of an encoding model.



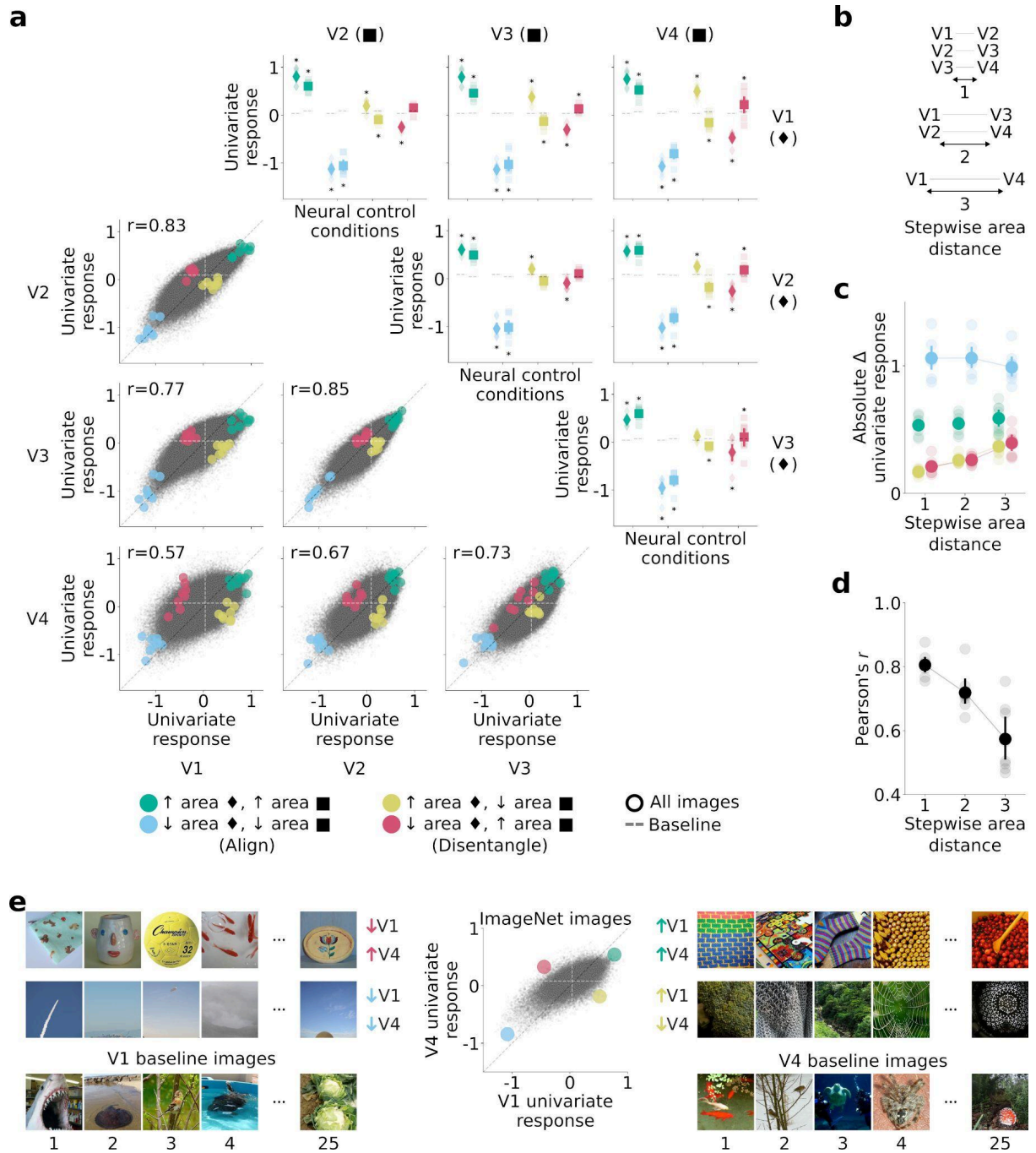
**Supplementary Figure 2 | Encoding models training and testing.** **a**, Encoding models training. For each subject and area, we trained end-to-end encoding models that take images as input and predict the corresponding fMRI responses, using the single-trial NSD responses for the 9,000 subject-unique images. During training, the model predictions were compared to the single-trial target fMRI responses, and the resulting error was backpropagated to update the encoding model weights. **b**, We tested the encoding models on an independent portion of the NSD data not used for training, consisting of fMRI responses for 515 images seen three times by all subjects, averaged across the three trials. **c**, We compared the noise of the in silico fMRI responses with the noise of the in vivo fMRI responses from the NSD, by comparing how much variance these two data types explained for a third, independent split of the in vivo NSD responses. Because the in silico fMRI responses did not capture all signal variance in the NSD responses, the in silico fMRI responses explaining more variance than the in vivo NSD responses would be indicative of the former being less affected by noise<sup>2,3</sup>. We carried out the comparison through three sets of predictions, using the in silico and the in vivo NSD fMRI responses for the 515 test images. Each prediction involved explaining in vivo single response trials from the NSD experiment with a different predictor. In the first set of predictions, the predictor consisted of one of the two remaining in vivo NSD experiment response trials. In the second set of predictions, the predictor consisted of the average of the two remaining in vivo NSD experiment response trials. In the third set of predictions, the predictor consisted of the in silico responses from the trained encoding models. **d**, Single NSD response trials noise-ceiling-normalized explained variance, for the three predictors of the noise analysis. The variance explained by the in silico responses is higher than the variance explained by both single and averaged NSD trials, indicating that the in silico fMRI responses are less affected by noise compared to the NSD responses. Colored asterisks indicate significant difference between the noise-ceiling-normalized explained variance scores of two predictors (within-subject permutation test,  $p < 0.05$ , Benjamini/Hochberg corrected over 2 tests for each area; population prevalence test,  $p < 10^{-10}$ , indicating within-subject significance in all 8 subjects), for each area. Error bars reflect 95% confidence intervals.



**Supplementary Figure 3 | Encoding models in-distribution and out-of-distribution noise-ceiling-normalized explained variance scores, averaged across all voxels within each area.** **a**, Noise-ceiling-normalized explained variance for encoding models trained on NSD. The in-distribution generalization scores reflect tests on a set of 515 images and fMRI responses not used for training. The out-of-distribution generalization scores reflect tests on the 284 NSD-synthetic images and fMRI responses<sup>4</sup>. **b**, Noise-ceiling-normalized explained variance for encoding models trained on the Visual Illusion Reconstruction Dataset<sup>5</sup>. The in-distribution generalization scores reflect tests on a set of 350 images and fMRI responses not used for training. The out-of-distribution generalization scores reflect tests on the 38 visual illusion images from the same dataset.

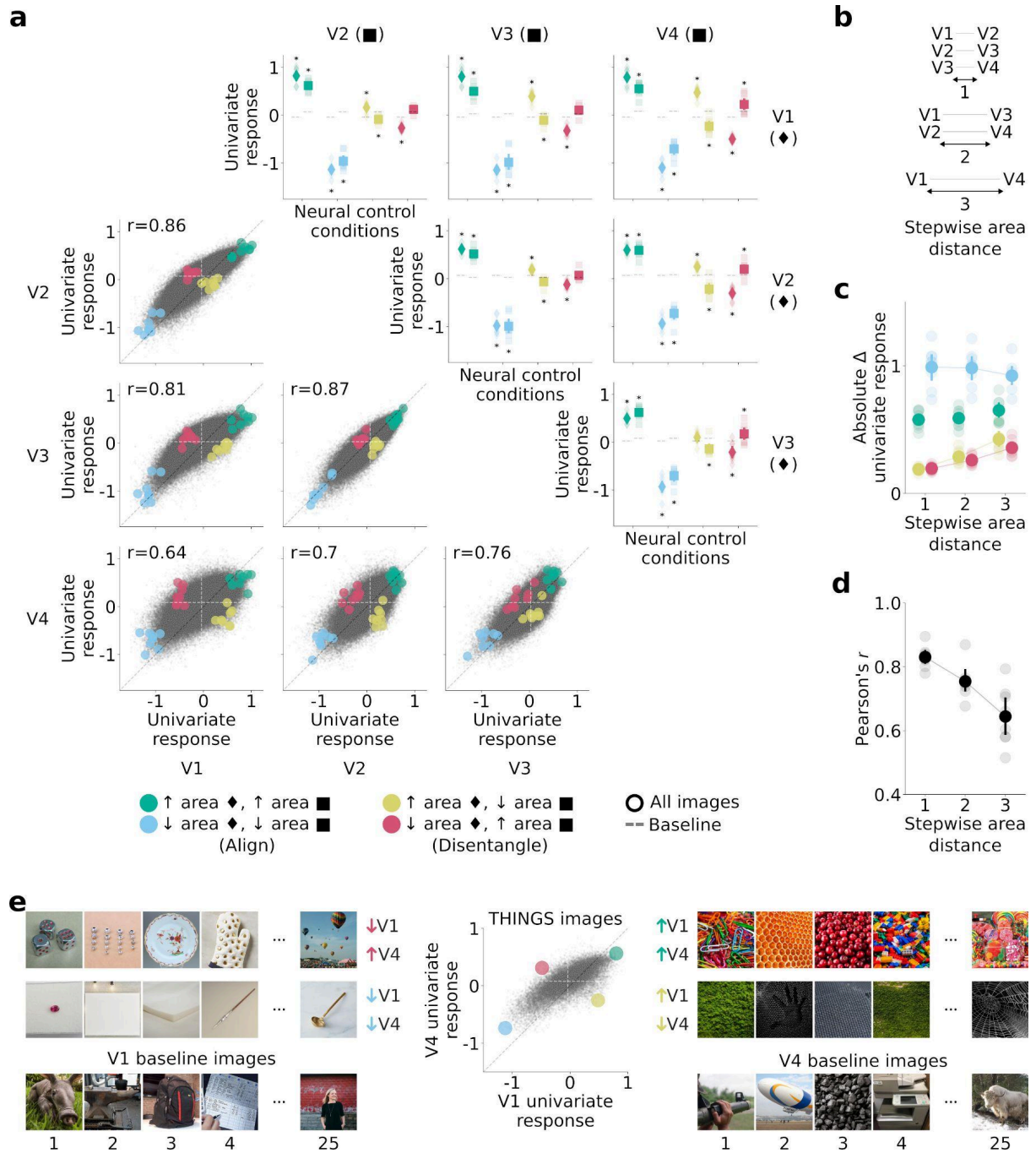


**Supplementary Figure 4 | Univariate RNC algorithm.** Univariate RNC searches for images leading to aligned or disentangled in silico univariate fMRI responses of two visual areas. The 73,000 NSD images are fed to the trained encoding models of two areas, and the resulting in silico fMRI responses averaged across voxels, obtaining a one-dimensional univariate response vector of length 73,000, for each area. The univariate response vectors of the two areas are either summed (alignment) or subtracted (disentanglement), the sum/difference scores ranked, and the controlling images leading to highest and lowest scores are kept. This results in four sets of controlling images, each set corresponding to a different neural control condition. The controlling images from the sum vector lead to two neural control conditions in which both areas have aligned univariate responses (i.e., images that either drive or suppress the responses of both areas), whereas the controlling images from the difference vector lead to two neural control conditions in which both areas have disentangled univariate responses (i.e. images that drive the responses of one area while suppressing the responses of the other area, and vice versa).

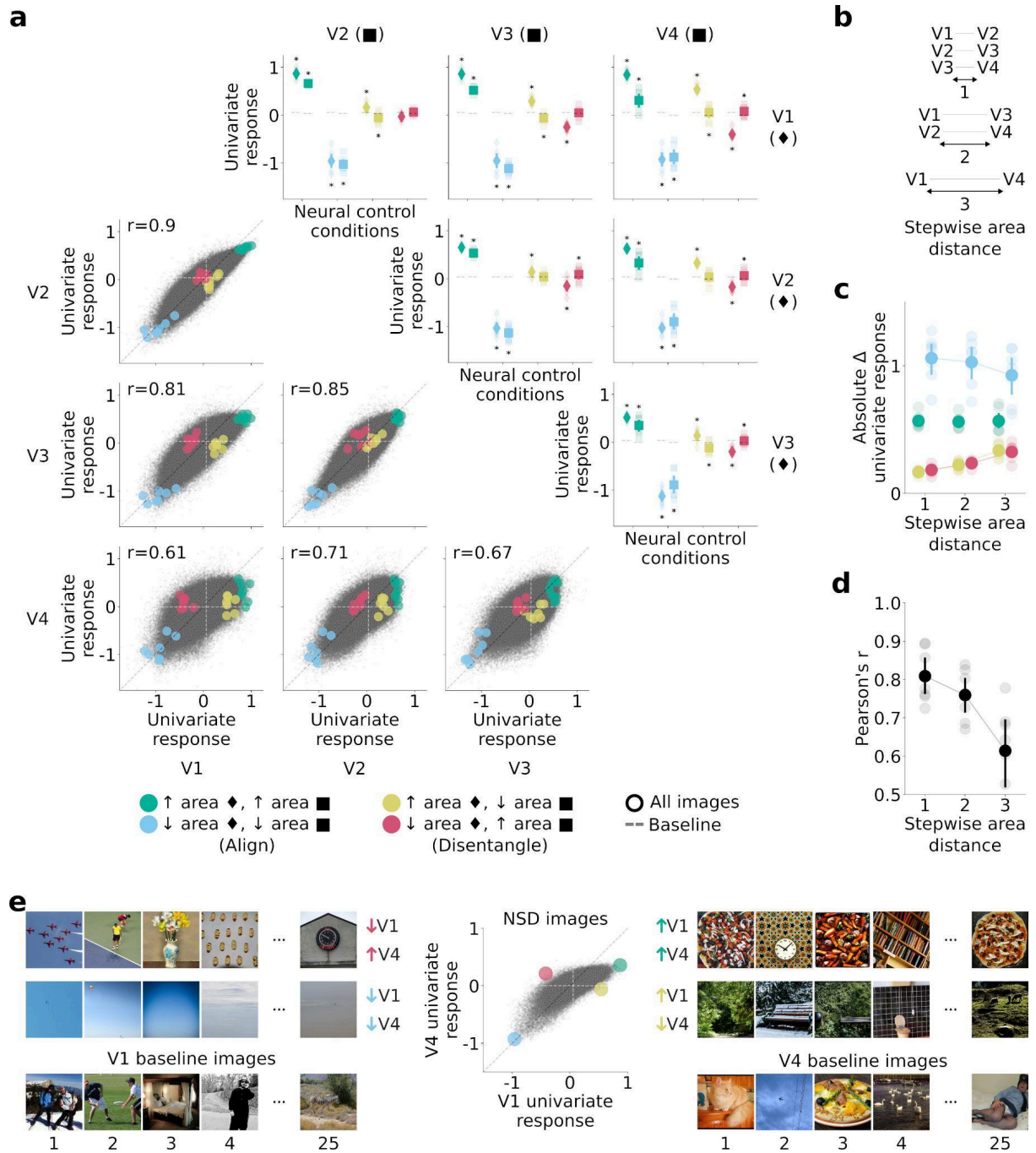


**Supplementary Figure 5 | Results of univariate RNC applied on the in silico fMRI responses for the 50,000 ImageNet images, generated through encoding models trained on NSD. a**, Univariate RNC quantitative results (univariate response magnitudes), embedded in a four-by-four matrix. **b**, Stepwise distance between areas. **c**, Absolute difference between controlling and baseline image univariate responses, averaged across all pairwise comparisons of areas with same stepwise distance. **d**, Correlation between the univariate responses of two areas, averaged across pairwise comparisons of areas with same stepwise distance. **e**, Univariate RNC controlling and baseline images for the V1 vs. V4 comparison.



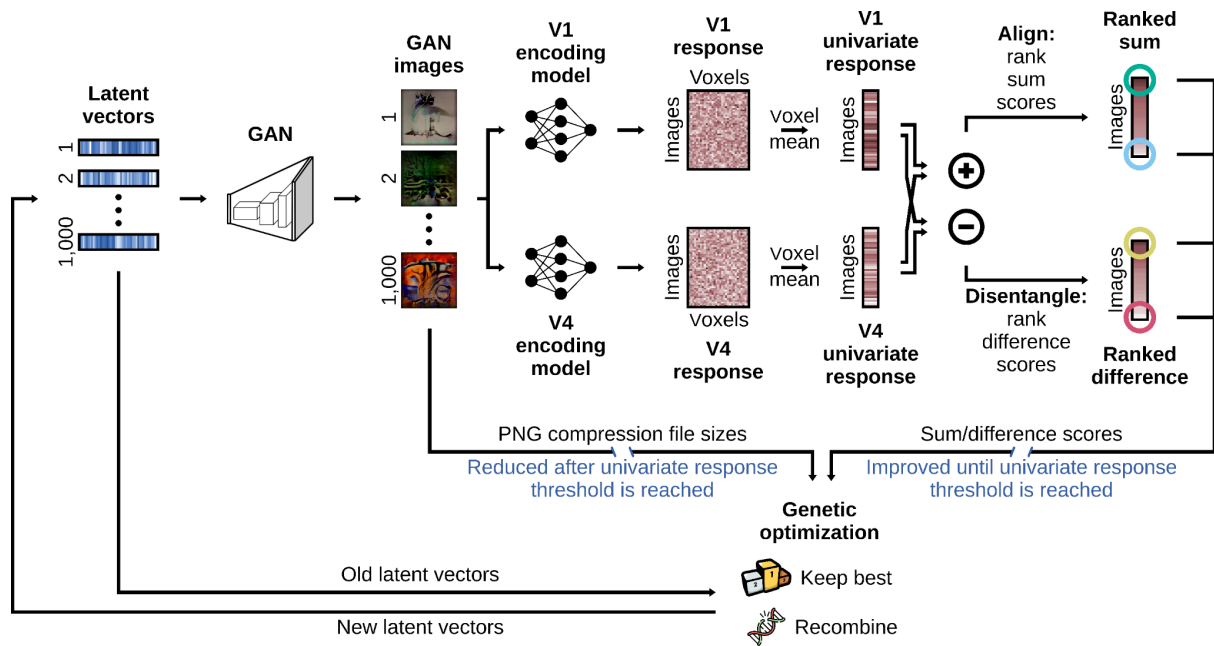


**Supplementary Figure 6 | Results of univariate RNC applied on the in silico fMRI responses for the 26,107 THINGS images, generated through encoding models trained on NSD. a**, Univariate RNC quantitative results (univariate response magnitudes), embedded in a four-by-four matrix. **b**, Stepwise distance between areas. **c**, Absolute difference between controlling and baseline image univariate responses, averaged across all pairwise comparisons of areas with same stepwise distance. **d**, Correlation between the univariate responses of two areas, averaged across pairwise comparisons of areas with same stepwise distance. **e**, Univariate RNC controlling and baseline images for the V1 vs. V4 comparison.

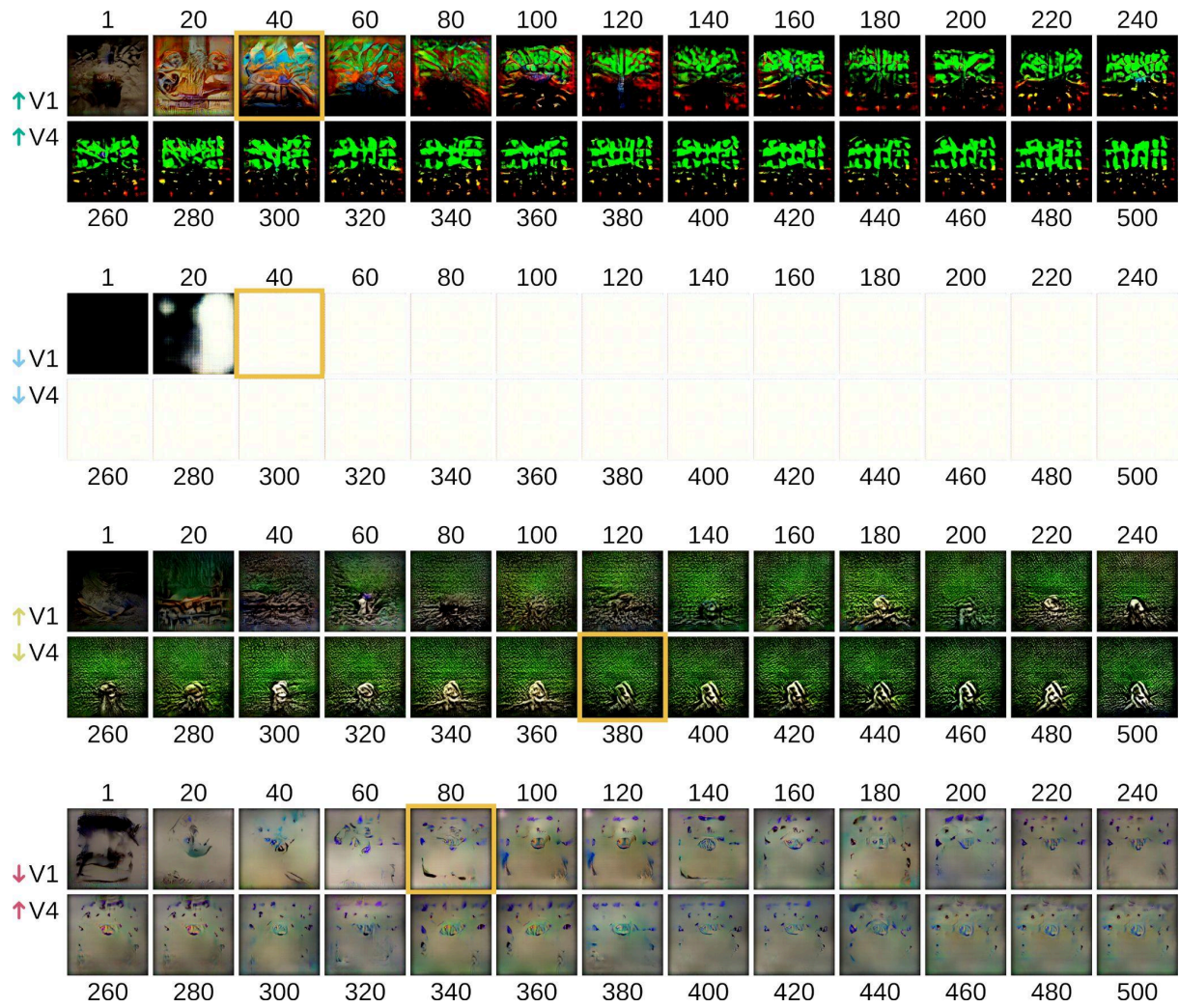


**Supplementary Figure 7 | Results of univariate RNC applied on the in silico fMRI responses for the 73,000 NSD images, generated through encoding models trained on the Visual Illusion Reconstruction dataset.** **a**, Univariate RNC quantitative results (univariate response magnitudes), embedded in a four-by-four matrix. **b**, Stepwise distance between areas. **c**, Absolute difference between controlling and baseline image univariate responses, averaged across all pairwise comparisons of areas with same stepwise distance. **d**, Correlation between the univariate responses of two areas, averaged across pairwise comparisons of areas with same stepwise distance. **e**, Univariate RNC controlling and baseline images for the V1 vs. V4 comparison.

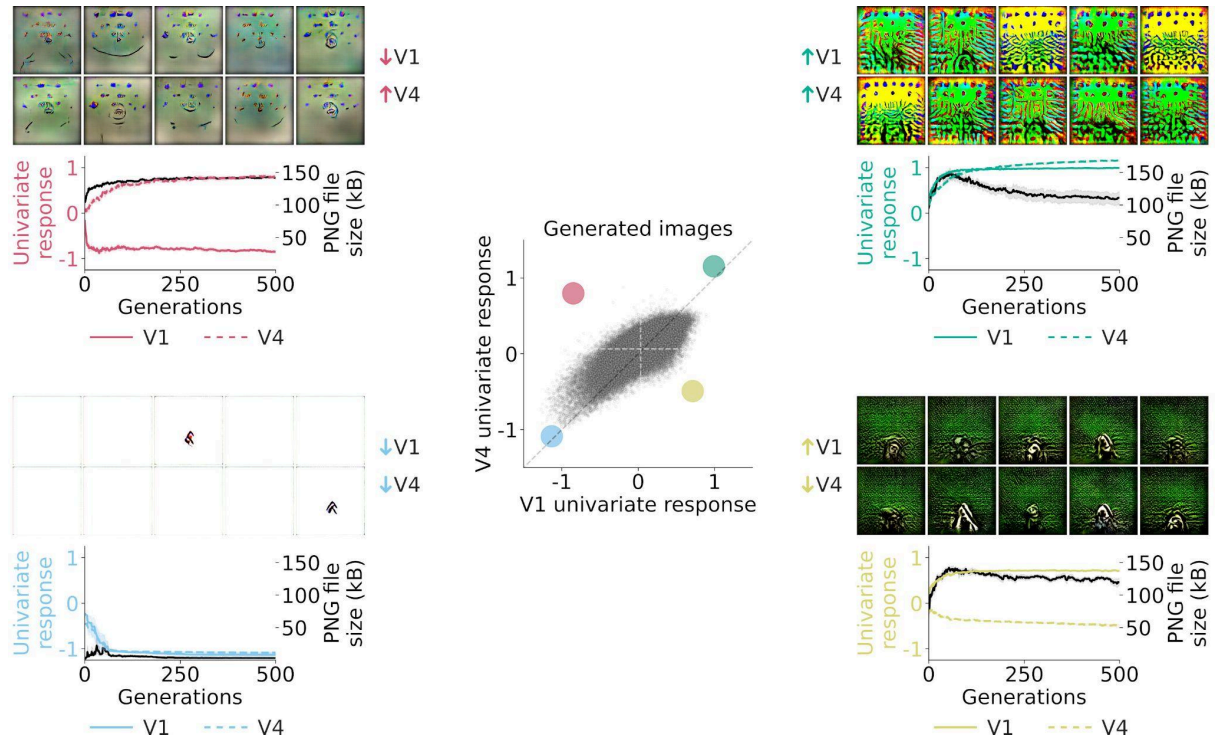




**Supplementary Figure 8 | Generative univariate RNC algorithm.** Generative univariate RNC generates stimulus images leading to aligned or disentangled in silico univariate fMRI responses for V1 and V4, while at the same time being as simple as possible. A batch of 1,000 random latent vectors is given as input to a GAN<sup>6</sup>, which uses them to generate 1,000 images, and the PNG compression file size of these images is calculated. Next, these images are fed to the trained encoding models of V1 and V4, and the resulting in silico fMRI responses averaged across voxels, obtaining a one-dimensional univariate response vector of length 1,000, for each area. The univariate response vectors of the two areas are either summed or subtracted, based on the neural control condition univariate RNC is optimizing for, thus obtaining sum/difference scores. The latent vectors, PNG compression file sizes, univariate responses, and sum/difference scores are then fed to a genetic optimization algorithm<sup>7,8</sup>, which uses them to create a new generation of latent vectors (by keeping the 250 best performing latent vectors, and recombining the remaining 750 latent vectors). At first the latent vectors are optimized using the sum/difference scores, so to result in images leading to in silico univariate fMRI responses for V1 and V4 closer to a threshold level. After this threshold is reached, the latent vectors are optimized using the PNG compression file sizes, so to result in images that are as simple as possible (while keeping the in silico univariate fMRI responses over the threshold). Finally, the new latent vectors are once again fed to the GAN, and the same steps are repeated over a new generation. After several genetic algorithm optimizations, this results in an image (i.e., the best performing image from the last genetic optimization generation) that well controls neural responses following one of the four univariate RNC neural control conditions (i.e., two alignment conditions where the in silico univariate fMRI responses of both areas are either driven or suppressed, and two disentanglement conditions where the in silico univariate fMRI response of one area is driven while the response of the other area is suppressed, and vice versa), while at the same time being as simple as possible. The images for the four neural control conditions are optimized independently of each other.

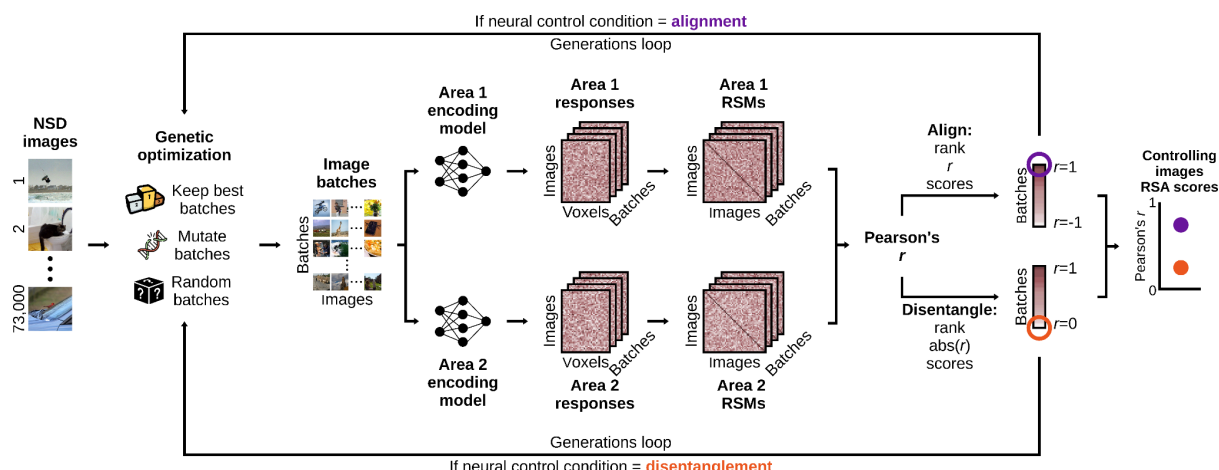


**Supplementary Figure 9 | Generative univariate RNC image solutions across generations, for one evolution.** For each neural control condition, the generated images from the 500 genetic optimization generations are shown in intervals of 20 generations. Generation numbers are added above or below the images. Only the best performing image from each generation is displayed (out of all 1,000 images tested in each generation). The images are optimized to control univariate responses up to a threshold, after which they are optimized to reduce their PNG compression file sizes. The univariate response threshold is reached at generation 35 for the neural control condition driving both V1 and V4, at generation 32 for the neural control condition suppressing both V1 and V4, at generation 372 for the neural control condition driving V1 while suppressing V4, and at generation 76 for the neural control condition suppressing V1 while driving V4. For each neural control condition, the first post-threshold generation image is surrounded by a golden box.



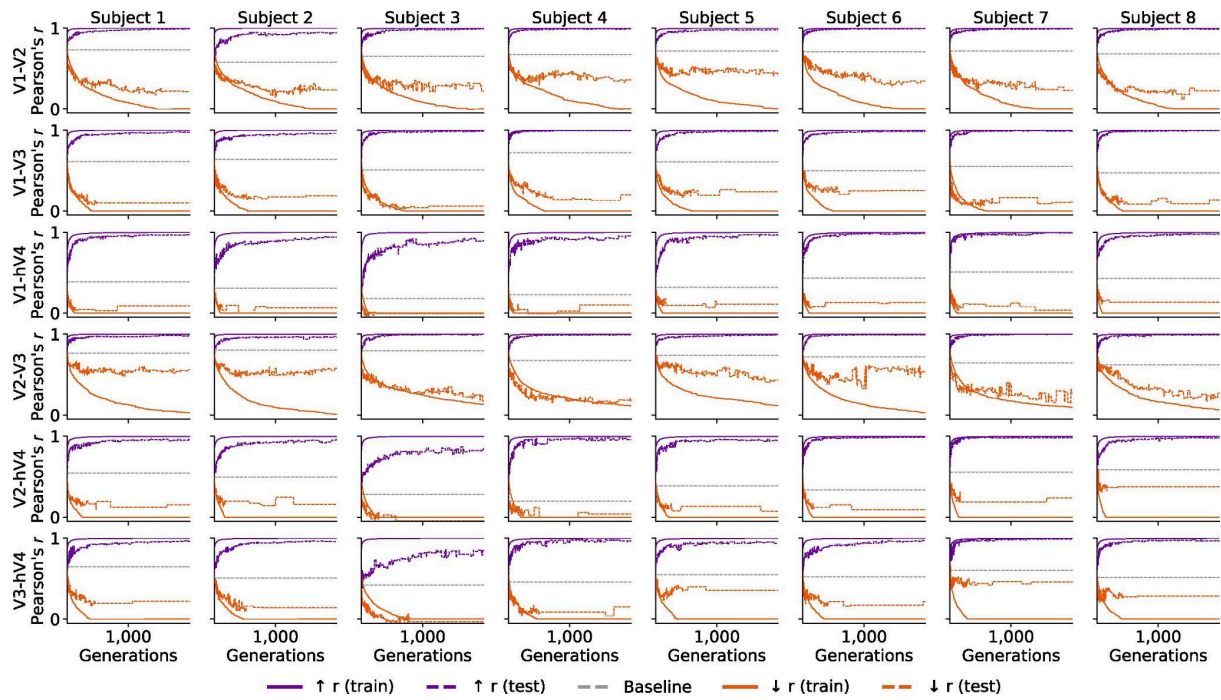
### Supplementary Figure 10 | Generative univariate RNC without image complexity reduction.

Results of ten independent generative univariate RNC evolutions using in silico fMRI responses averaged across all 8 subjects. Across the 500 genetic algorithm generations, the images are only optimized to improve the neural control scores (i.e., the PNG compression file size is not reduced). For each neural control condition, the plots show the in silico univariate fMRI responses (represented by colored lines) and the PNG compression file size (represented by black lines) for the best GAN-generated image of each genetic algorithm generation, averaged across evolutions. On top of each plot are the optimized images from the ten evolutions.

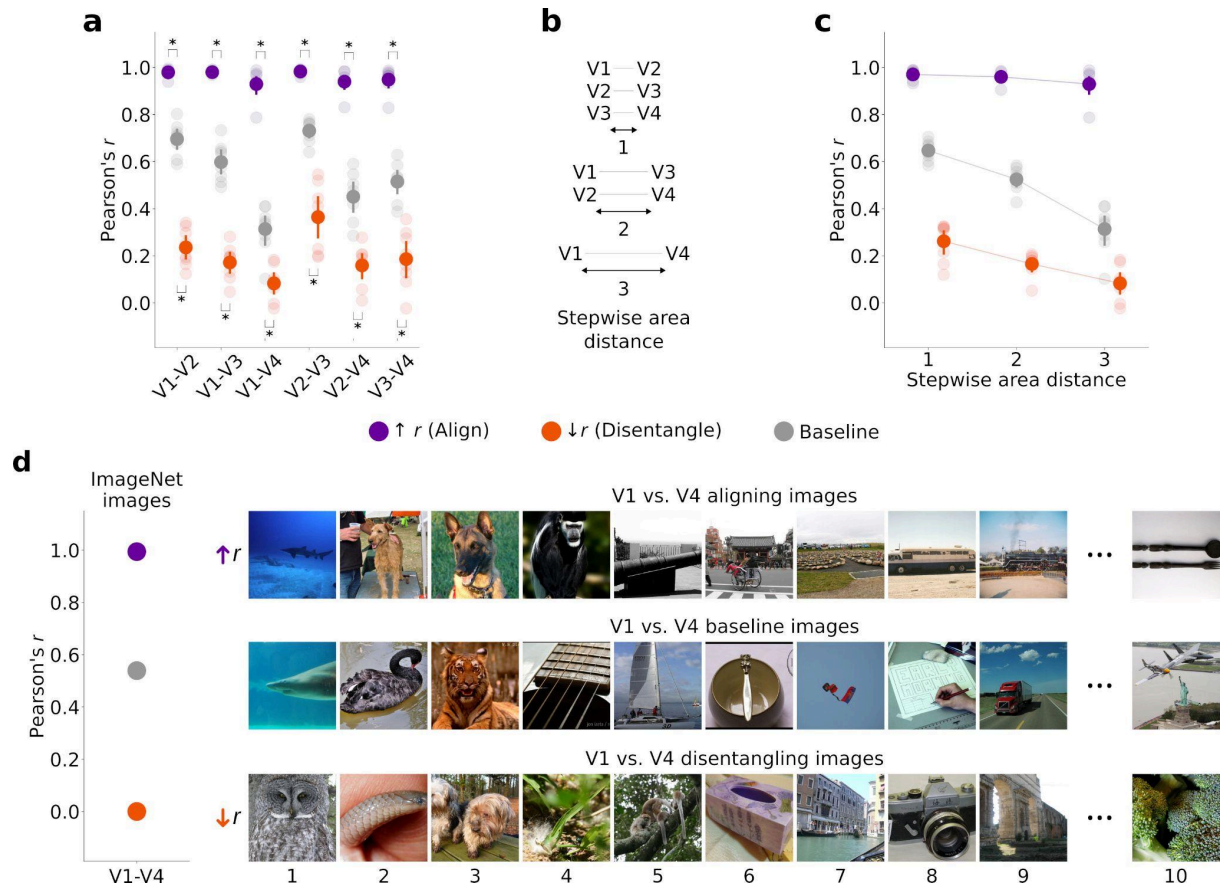


**Supplementary Figure 11 | Multivariate RNC algorithm.** Multivariate RNC searches for images leading to aligned or disentangled in silico multivariate fMRI responses of two visual brain areas. Random images batches from the 73,000 NSD images are fed to the trained encoding models of two areas, and the resulting in silico fMRI responses are transformed into representational similarity matrices (RSMs)<sup>9</sup>, yielding one RSM for each image batch and area. The RSMs of the two areas are then compared through RSA (i.e., Pearson's correlation), obtaining one RSA correlation score ( $r$ ) for each image batch, and the correlation scores ranked. To align the two areas, the image batches with highest correlation scores (i.e., containing images most similarly represented by the two areas) undergo a genetic optimization (which involves keeping these image batches, creating mutated versions of them, and adding random image batches), resulting in new image batches likely to better align the two areas<sup>7,8,10,11</sup>. Finally, these new image batches are once again fed to the encoding models, and the same steps are repeated over a new generation. To disentangle the two areas the image batches with lowest absolute correlation scores (i.e., containing images most differently represented by the two areas) are instead genetically optimized, resulting in new image batches likely to better disentangle the two areas. After several genetic optimization generations, this results in an image batch that well controls neural responses following one of the two multivariate RNC neural control conditions. The controlling images from the ranked correlation vector lead both areas to have aligned multivariate responses (i.e., images leading to high RSA correlation scores for the two areas), whereas the controlling images from the absolute ranked correlation vector lead both areas to have disentangled multivariate responses (i.e., images leading to low absolute RSA correlation scores for the two areas). The image batches from the two neural control conditions are optimized independently of each other.

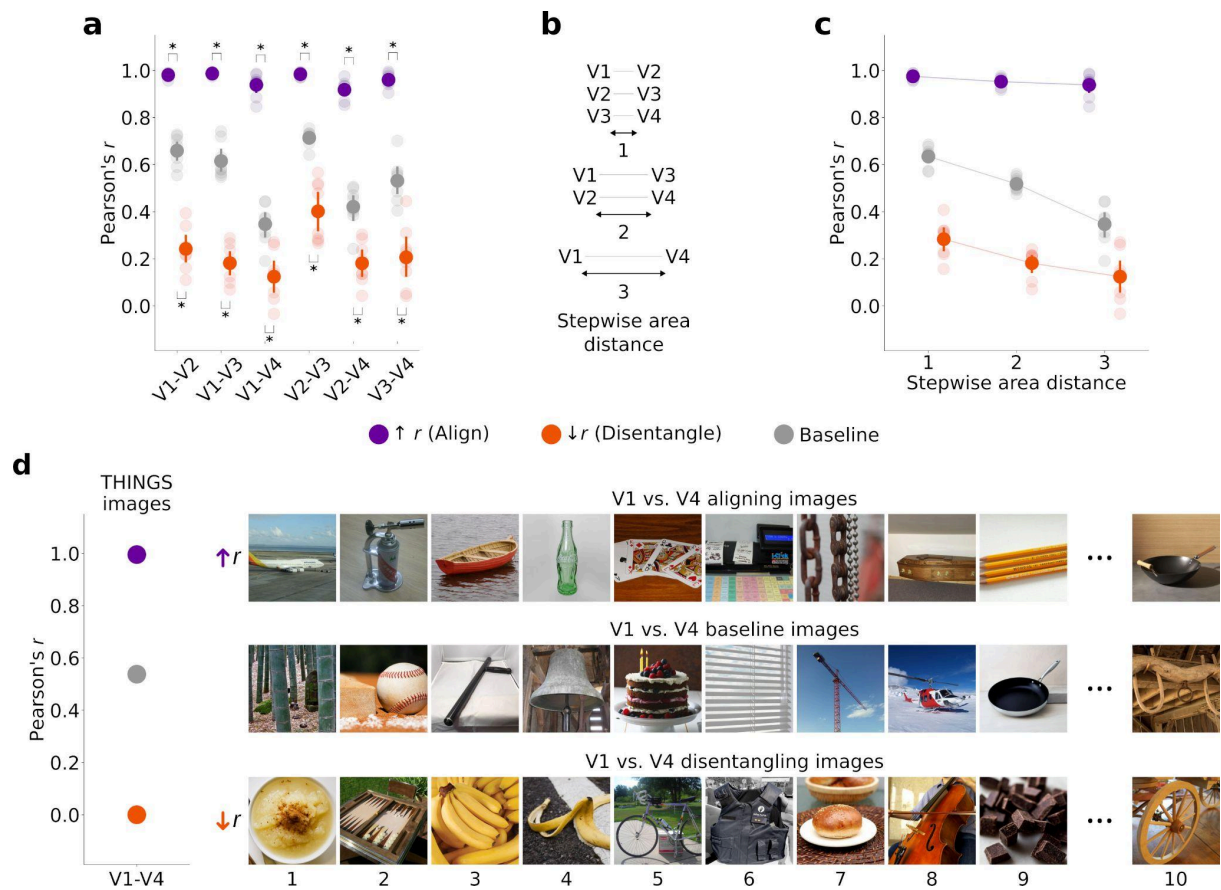




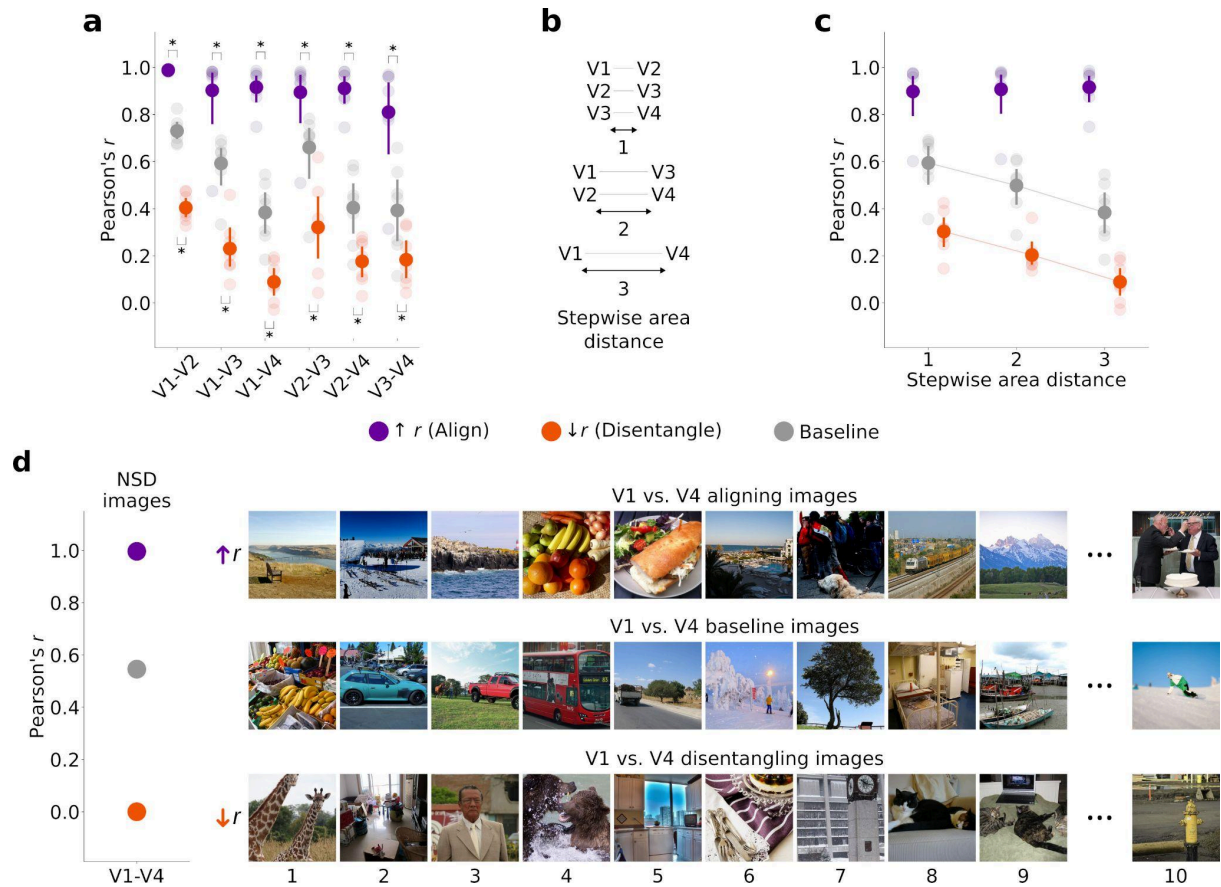
**Supplementary Figure 12 | Multivariate RNC optimization curves.** Optimization curves of multivariate RNC applied on the in silico fMRI responses for the 73,000 NSD images. Each row corresponds to a different pairwise comparison of areas, and each column to a different subject. The train curves indicate the neural control condition scores for the subject-average RSMs on which multivariate RNC was applied, and the test curves indicate the neural control condition scores for the remaining subject on which the multivariate RNC solutions were cross-validated.



**Supplementary Figure 13 | Results of multivariate RNC applied on the in silico fMRI responses for the 50,000 ImageNet images, generated through encoding models trained on NSD. a,** Multivariate RNC quantitative results (RSA scores). **b,** Stepwise distance between areas. **c,** Multivariate RNC RSA scores, averaged across pairwise comparisons of areas with same stepwise distance. **d,** Controlling and baseline images for the V1 vs. V4 comparison.

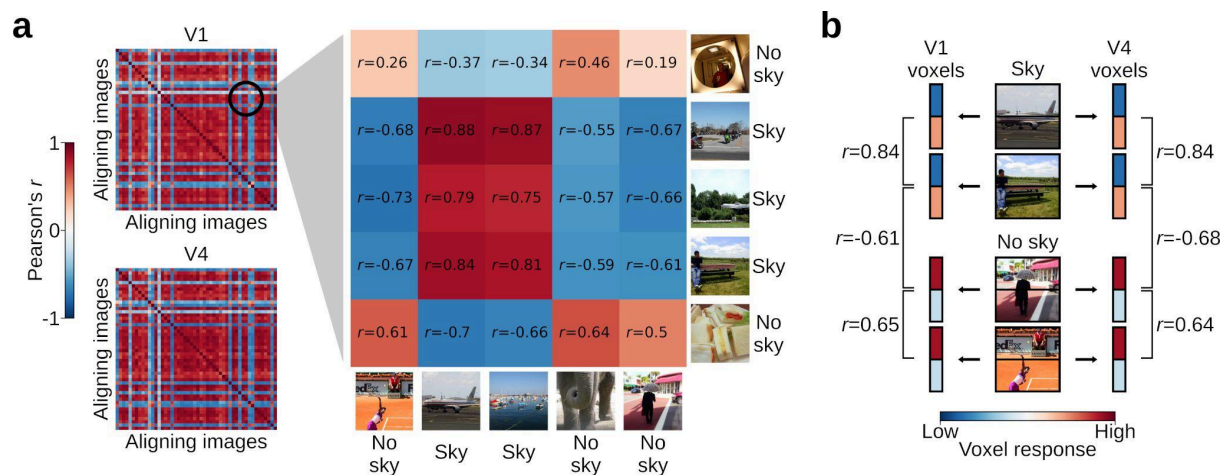


**Supplementary Figure 14 | Results of multivariate RNC applied on the in silico fMRI responses for the 26,107 THINGS images, generated through encoding models trained on NSD. a,** Multivariate RNC quantitative results (RSA scores). **b,** Stepwise distance between areas. **c,** Multivariate RNC RSA scores, averaged across pairwise comparisons of areas with same stepwise distance. **d,** Controlling and baseline images for the V1 vs. V4 comparison.

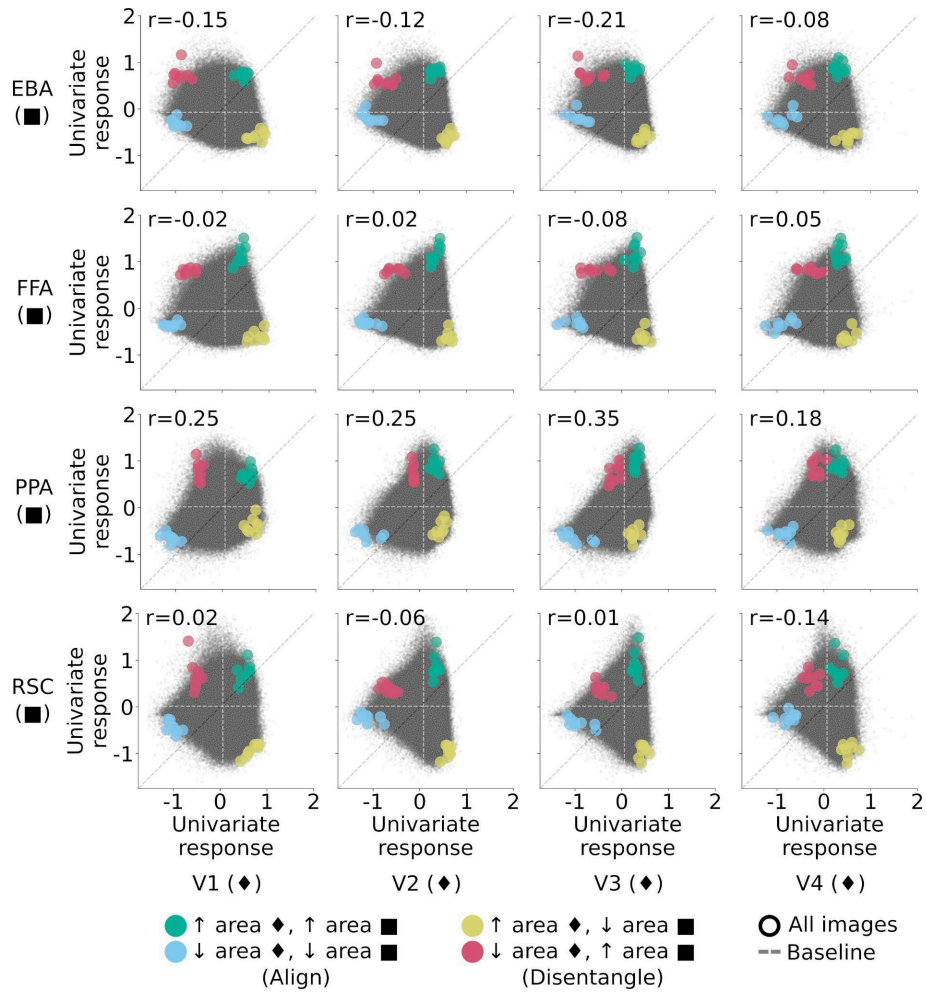


**Supplementary Figure 15 | Results of multivariate RNC applied on the in silico fMRI responses for the 73,000 NSD images, generated through encoding models trained on the Visual Illusion Reconstruction dataset. a**, Multivariate RNC quantitative results (RSA scores). **b**, Stepwise distance between areas. **c**, Multivariate RNC RSA scores, averaged across pairwise comparisons of areas with same stepwise distance. **d**, Controlling and baseline images for the V1 vs. V4 comparison.

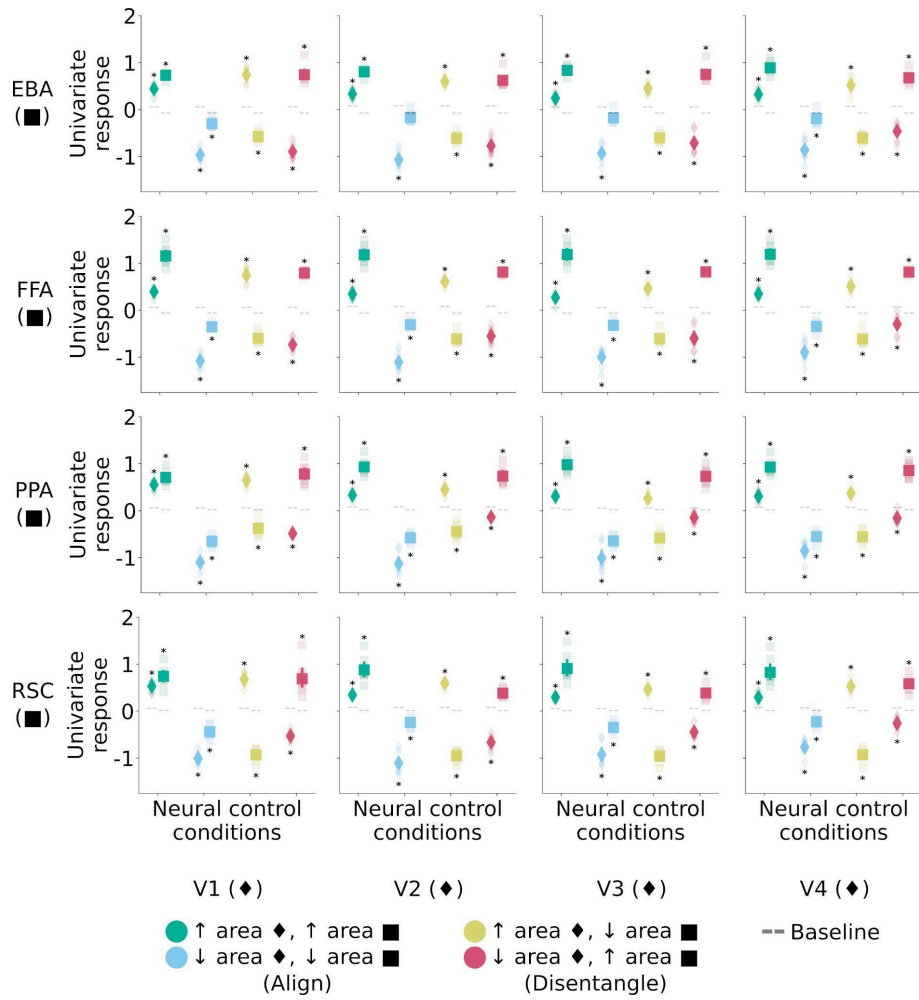




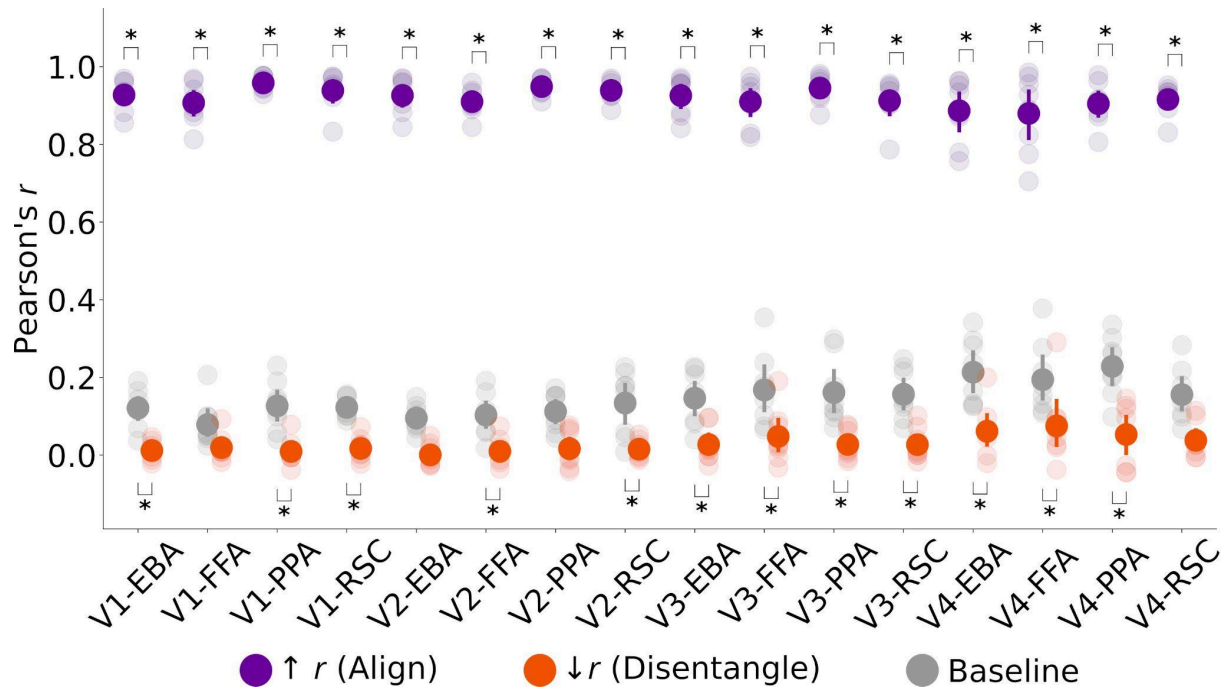
**Supplementary Figure 16 | Relationship between multivariate RNC controlling images, fMRI responses, and RSM entries. a, V1 and V4 subject-average RSMs for the multivariate RNC aligning images. b, Relationship between images with and without the sky on their upper half, and fMRI responses for voxels tuned to the higher and lower portion of the visual field. Due to retinotopy, uniform regions on a spatially constrained portion of the image led to suppressed responses for voxels tuned to the corresponding portion of the visual field. Thus, the response of voxels tuned to the upper portion of the visual field were consistently suppressed by images including the sky on their upper half, whereas the same images drove the response of voxels tuned to the lower portion of the visual field (since the lower portion of these images includes non-uniform regions such as objects) (Main Figure 5d). The opposite pattern was observed for images not including the sky (Main Figure 5d). This led to highly positive correlations (and corresponding RSM entries) when correlating the voxel responses for two sky images, or for two no sky images, and to highly negative correlations when correlating the voxel responses for a sky image and a no sky image (Main Figure 5c).**



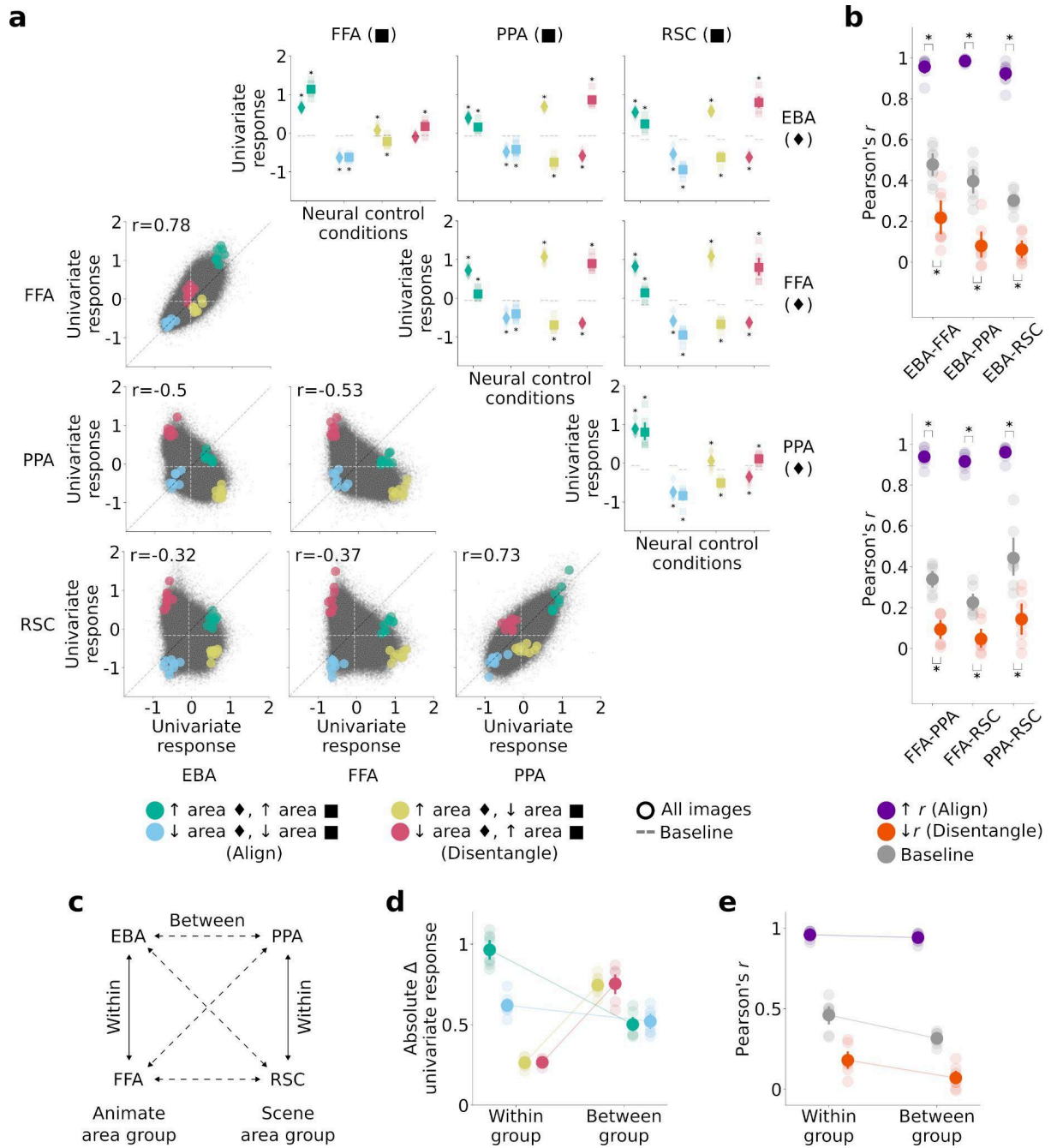
**Supplementary Figure 17 | Univariate RNC results for interactions between early-, mid-, and high-level visual areas.** Univariate response image manifolds. Colored dots indicate in silico univariate fMRI responses averaged across the controlling images of each neural control condition, and small black points indicate in silico univariate fMRI responses of all subjects for all 73,000 NSD images. Vertical and horizontal dashed lines indicate subject-average univariate response baseline for each area.



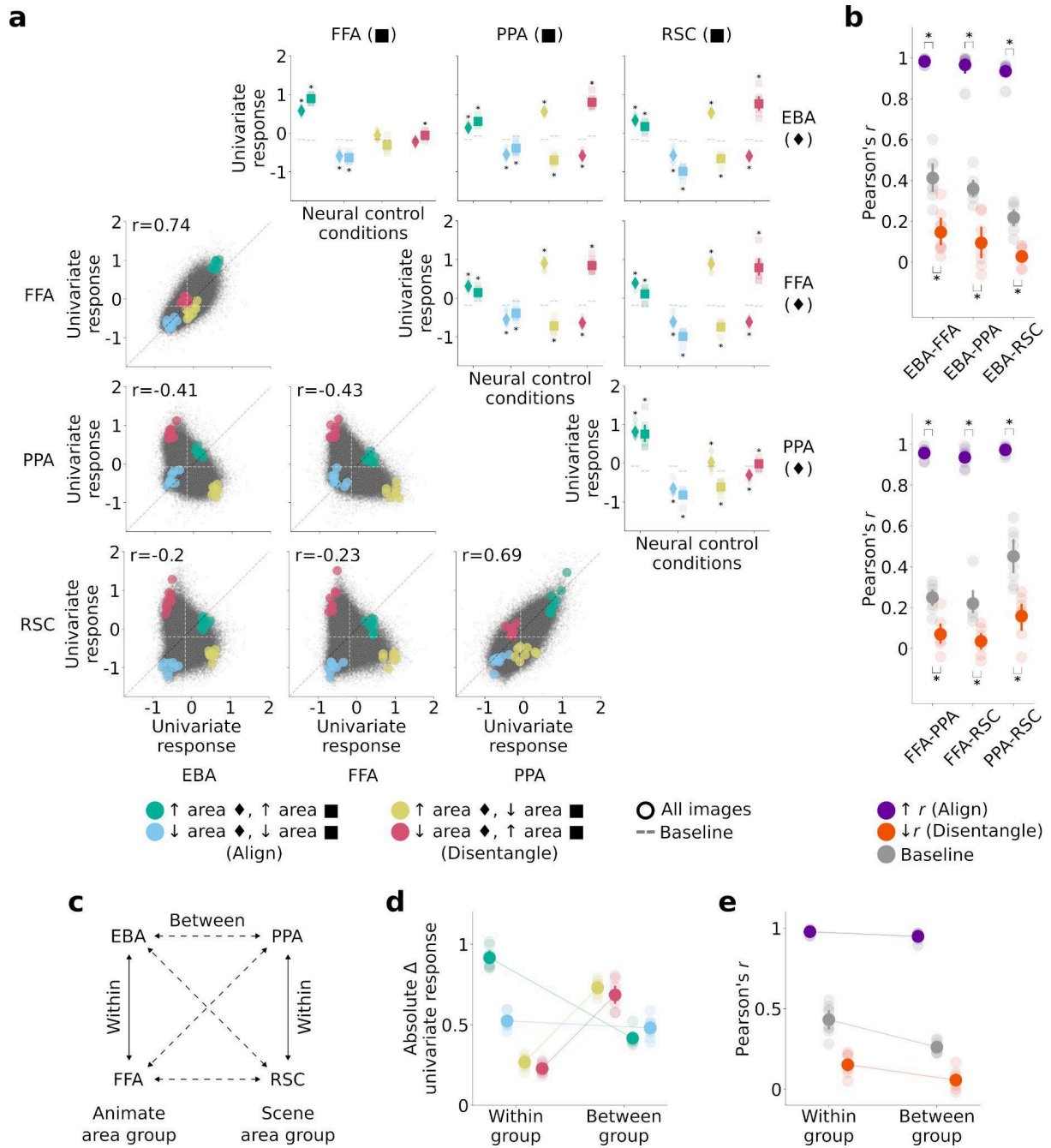
**Supplementary Figure 18 | Univariate RNC results for interactions between early-, mid-, and high-level visual areas.** Univariate responses for the controlling images against the baseline. Diamonds and squares indicate the univariate responses of the areas indexed by the rows and columns of the results matrix, respectively.



**Supplementary Figure 19 | Multivariate RNC results for interactions between early-, mid-, and high-level visual areas.** Multivariate RNC results, consisting of RSA scores (Pearson's  $r$ ) for each pairwise comparison of areas.

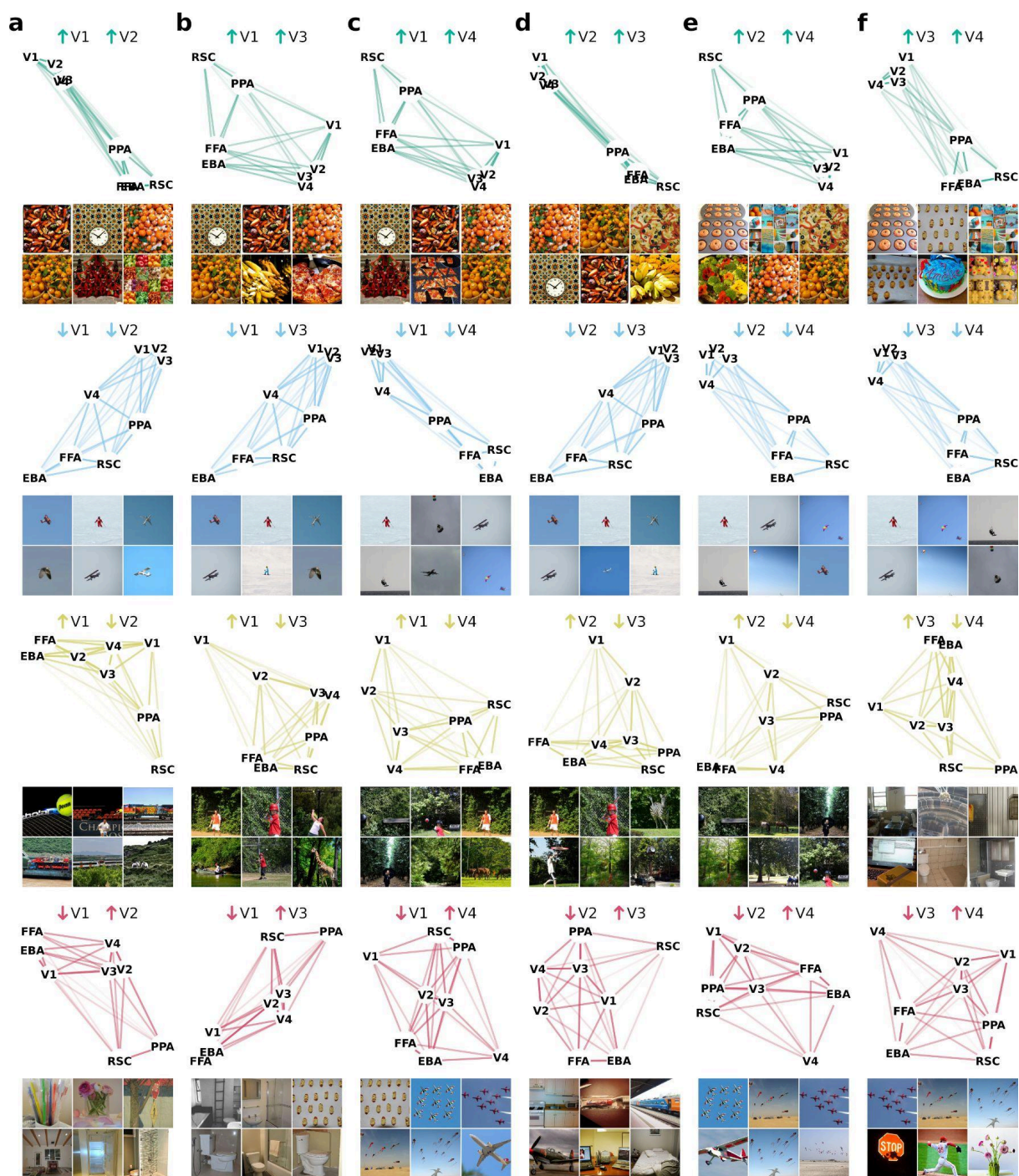


**Supplementary Figure 20 | Results of RNC applied on the in silico fMRI responses of high-level visual areas for the 50,000 ImageNet images, generated through encoding models trained on NSD.** **a**, Univariate RNC quantitative results (univariate response magnitudes), embedded in a four-by-four matrix **b**, Multivariate RNC quantitative results (RSA scores) **c**, Categorical selectivity groups. Solid and dashed lines represent within- and between- group area comparisons, respectively. **d**, Absolute difference between controlling and baseline image univariate responses, averaged across within- or between-group area comparisons. **e**, Multivariate RNC RSA scores, averaged across within- or between-group area comparisons.



**Supplementary Figure 21 | Results of RNC applied on the in silico fMRI responses of high-level visual areas for the 26,107 THINGS images, generated through encoding models trained on NSD.** **a**, Univariate RNC quantitative results (univariate response magnitudes), embedded in a four-by-four matrix **b**, Multivariate RNC quantitative results (RSA scores) **c**, Categorical selectivity groups. Solid and dashed lines represent within- and between- group area comparisons, respectively. **d**, Absolute difference between controlling and baseline image univariate responses, averaged across within- or between-group area comparisons. **e**, Multivariate RNC RSA scores, averaged across within- or between-group area comparisons.



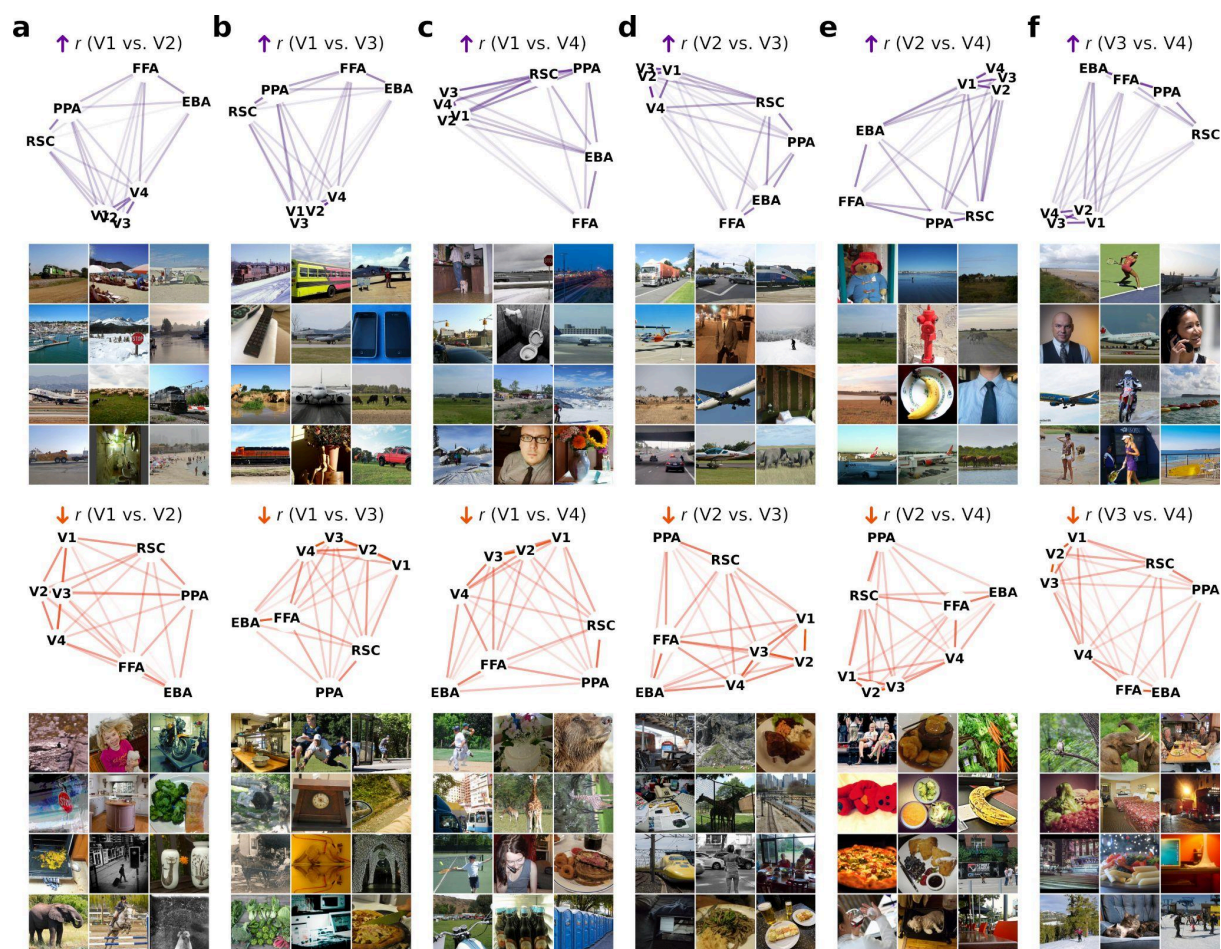


**Supplementary Figure 22 | Multidimensional scaling (MDS) embeddings of the in silico univariate fMRI responses for controlling images found by applying univariate RNC on early- and mid-level visual areas.** Six exemplar controlling images are shown for each control condition (all images come from the 73,000 NSD images). Each panel reflects MDS results and controlling images for a different pairwise comparison of areas. **a**, V1 vs. V2 comparison. **b**, V1 vs. V3 comparison. **c**, V1 vs. V4 comparison. **d**, V2 vs. V3 comparison. **e**, V2 vs. V4 comparison. **f**, V3 vs. V4 comparison.

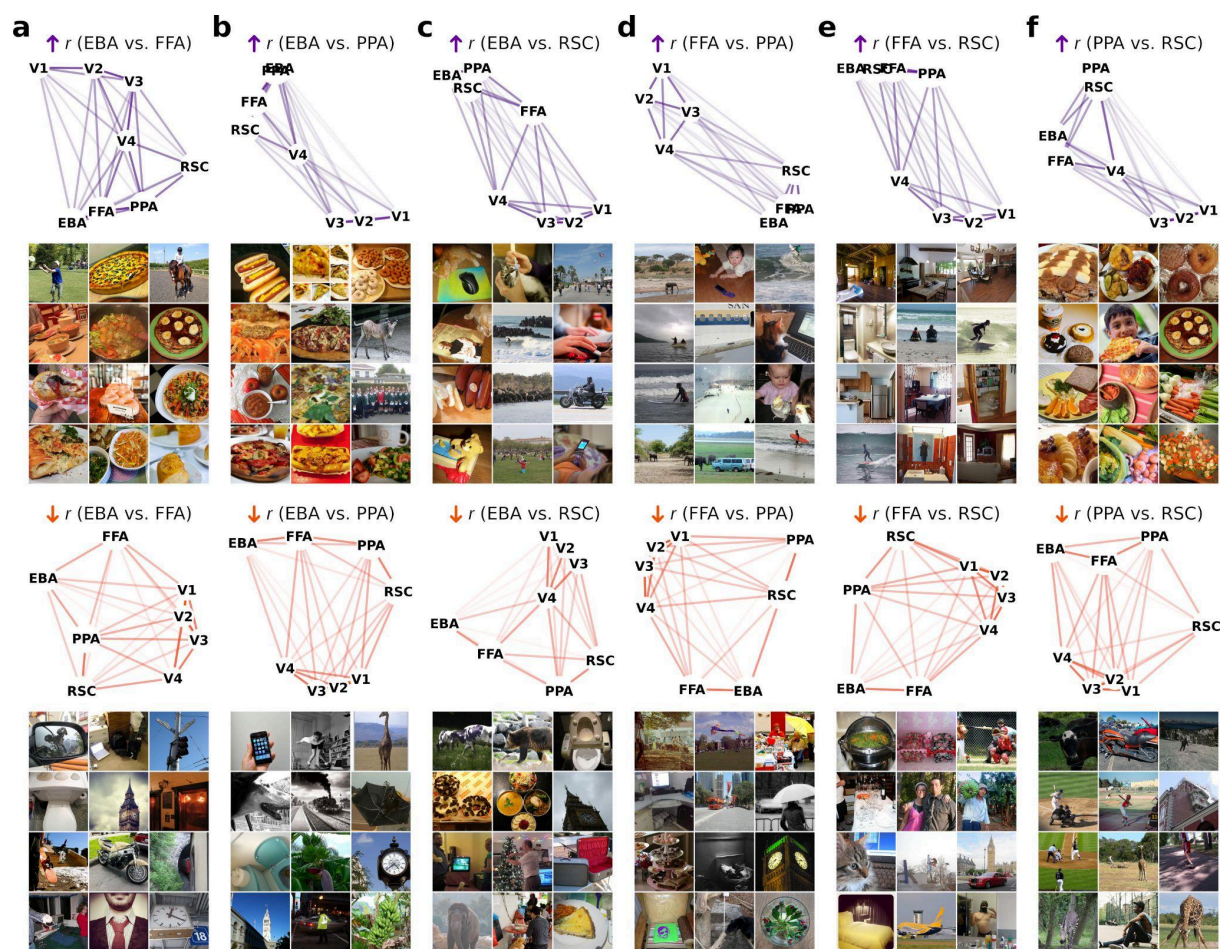


**Supplementary Figure 23 | Multidimensional scaling (MDS) embeddings of the in silico univariate fMRI responses for controlling images found by applying univariate RNC on high-level visual areas.** Six exemplar controlling images are shown for each control condition (all images come from the 73,000 NSD images). Each panel reflects MDS results and controlling images for a different pairwise comparison of areas. **a**, EBA vs. FFA comparison. **b**, EBA vs. PPA comparison. **c**, EBA vs. RSC comparison. **d**, FFA vs. PPA comparison. **e**, FFA vs. RSC comparison. **f**, PPA vs. RSC comparison.



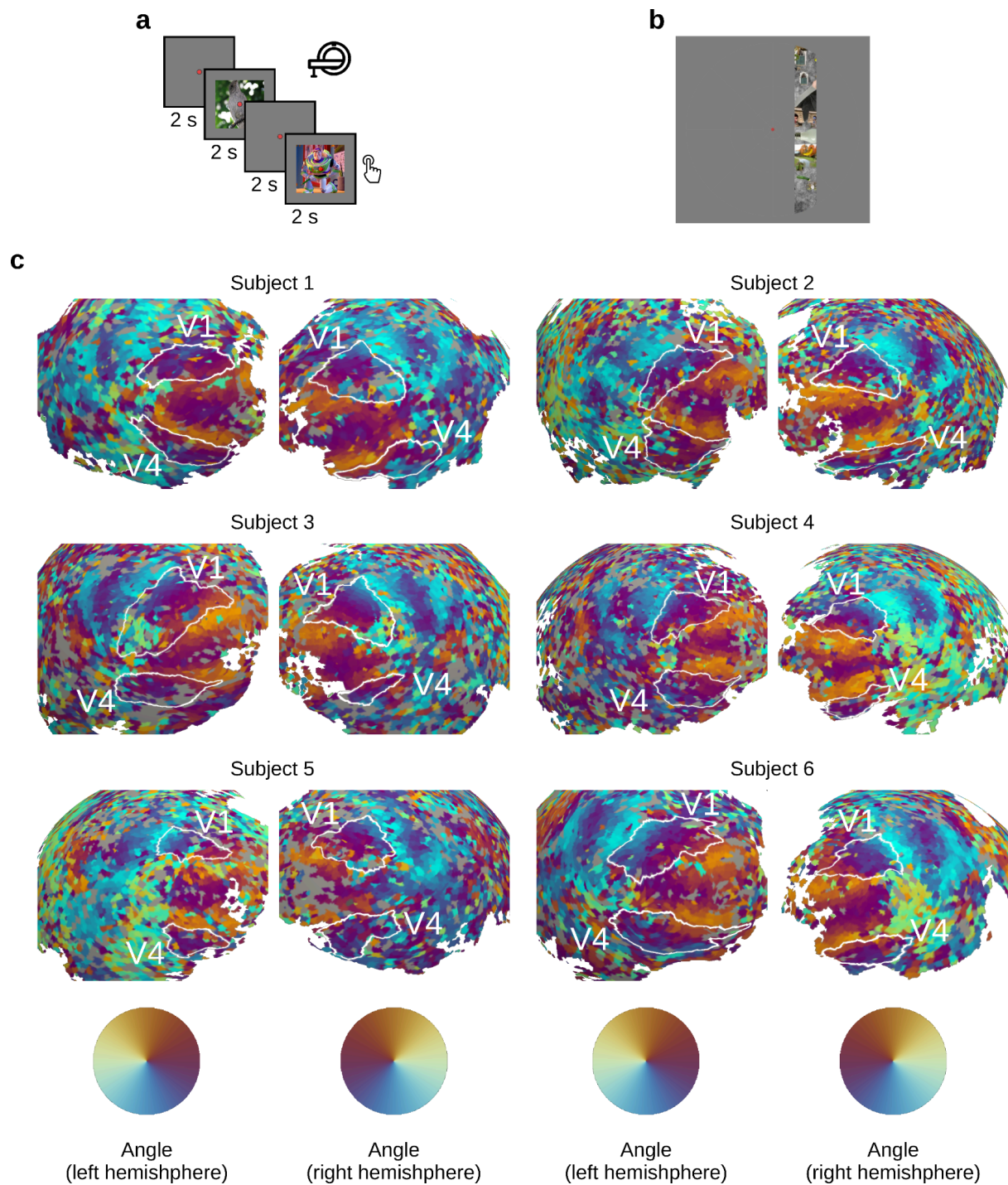


**Supplementary Figure 24 | Multidimensional scaling (MDS) embeddings of the in silico multivariate fMRI responses for controlling images found by applying multivariate RNC on early- and mid-level visual areas.** Twelve exemplar controlling images are shown for each control condition (all images come from the 73,000 NSD images). Each panel reflects MDS results and controlling images for a different pairwise comparison of areas. **a**, V1 vs. V2 comparison. **b**, V1 vs. V3 comparison. **c**, V1 vs. V4 comparison. **d**, V2 vs. V3 comparison. **e**, V2 vs. V4 comparison. **f**, V3 vs. V4 comparison.



**Supplementary Figure 25 | Multidimensional scaling (MDS) embeddings of the in silico multivariate fMRI responses for controlling images found by applying multivariate RNC on high-level visual areas.** Twelve exemplar controlling images are shown for each control condition (all images come from the 73,000 NSD images). Each panel reflects MDS results and controlling images for a different pairwise comparison of areas. **a**, EBA vs. FFA comparison. **b**, EBA vs. PPA comparison. **c**, EBA vs. RSC comparison. **d**, FFA vs. PPA comparison. **e**, FFA vs. RSC comparison. **f**, PPA vs. RSC comparison.





**Supplementary Figure 26 | In vivo fMRI experiments and polar angle maps.** **a**, Experimental design. We presented the univariate and multivariate RNC controlling and baseline images during a target detection task, where we asked subjects to press a button whenever an image with Buzz Lightyear appeared on the screen. Each image was presented for two seconds, followed by two seconds of inter-stimulus interval. Subjects were asked to fixate a central red dot during the entire experiment. fMRI responses were collected during image presentation. **b**, Screenshot of the pRF experiment used to delineate areas V1 and V4. **c**, Polar angle maps and V1/V4 delineations. Results are shown on FreeSurfer's sphere surface.

	V1	V2	V3	V4
<b>Subject 1</b>	813 / 1,350 (60 %)	656 / 1,433 (46 %)	486 / 1,187 (41 %)	176 / 687 (26 %)
<b>Subject 2</b>	598 / 1,102 (54 %)	407 / 1,075 (38 %)	448 / 1,097 (41 %)	239 / 483 (49 %)
<b>Subject 3</b>	553 / 1,254 (44 %)	366 / 1,141 (32 %)	152 / 928 (16 %)	61 / 426 (14 %)
<b>Subject 4</b>	340 / 877 (39 %)	285 / 863 (33 %)	141 / 808 (17 %)	40 / 475 (8 %)
<b>Subject 5</b>	529 / 1,113 (48 %)	424 / 1,081 (39 %)	259 / 925 (28 %)	154 / 542 (28 %)
<b>Subject 6</b>	484 / 1,127 (43 %)	381 / 1,180 (32 %)	205 / 1,201 (17 %)	50 / 477 (10 %)
<b>Subject 7</b>	273 / 1,142 (24 %)	174 / 986 (18 %)	86 / 726 (12 %)	48 / 397 (12 %)
<b>Subject 8</b>	234 / 1,074 (22 %)	168 / 1,033 (16 %)	68 / 889 (7 %)	60 / 495 (12 %)

**Supplementary Table 1 | Early and mid-level visual areas' retained voxels for in silico fMRI responses from encoding models trained on NSD.** Each cell indicates the amount of retained voxels (i.e., voxels with noise ceiling signal-to-noise ratio (ncsnr) scores above 0.5) out of the total voxels, for a given subject and area.

	EBA	FFA	PPA	RSC
<b>Subject 1</b>	1,145 / 2,971 (39 %)	164 / 794 (21 %)	158 / 1,033 (15 %)	87 / 566 (15 %)
<b>Subject 2</b>	1,036 / 3,439 (30 %)	230 / 869 (26 %)	271 / 994 (27 %)	244 / 813 (30 %)
<b>Subject 3</b>	831 / 3,518 (24 %)	205 / 1,093 (19 %)	220 / 1,269 (17 %)	20 / 838 (2 %)
<b>Subject 4</b>	730 / 3,288 (22 %)	163 / 942 (17 %)	141 / 960 (15 %)	59 / 813 (7 %)
<b>Subject 5</b>	1,587 / 4,587 (35 %)	220 / 907 (24 %)	444 / 1,221 (36 %)	77 / 771 (10 %)
<b>Subject 6</b>	1,029 / 4,126 (25 %)	156 / 826 (19 %)	287 / 1,229 (23 %)	27 / 845 (3 %)
<b>Subject 7</b>	521 / 3,062 (17 %)	47 / 484 (10 %)	61 / 912 (7 %)	18 / 694 (3 %)
<b>Subject 8</b>	200 / 3,184 (6 %)	116 / 1,204 (10 %)	88 / 961 (9 %)	13 / 799 (2 %)

**Supplementary Table 2 | High-level visual areas' retained voxels for in silico fMRI responses from encoding models trained on NSD.** Each cell indicates the amount of retained voxels (i.e., voxels with noise ceiling signal-to-noise ratio (ncsnr) scores above 0.5) out of the total voxels, for a given subject and area.

	V1	V2	V3	V4
<b>Subject 1</b>	419 / 2,444 (17 %)	444 / 3,018 (15 %)	326 / 2,556 (13 %)	20 / 899 (2 %)
<b>Subject 2</b>	427 / 2,850 (15 %)	343 / 2,927 (12 %)	257 / 3,120 (8 %)	65 / 1,089 (6 %)
<b>Subject 3</b>	232 / 2,045 (11 %)	185 / 2,536 (7 %)	130 / 2,763 (5 %)	16 / 1,916 (1 %)
<b>Subject 4</b>	80 / 2,637 (3 %)	38 / 2,921 (1 %)	17 / 2,336 (1 %)	12 / 1,552 (1 %)
<b>Subject 5</b>	144 / 2,210 (7 %)	74 / 2,032 (4 %)	53 / 2,222 (2 %)	40 / 1,971 (2 %)
<b>Subject 6</b>	608 / 2,614 (23 %)	640 / 2,909 (22 %)	588 / 3,023 (19 %)	139 / 1,338 (10 %)
<b>Subject 7</b>	609 / 1,892 (32 %)	701 / 2,113 (33 %)	635 / 1,930 (33 %)	241 / 986 (24 %)

**Supplementary Table 3 | Early and mid-level visual areas' retained voxels for in silico fMRI responses from encoding models trained on the Visual Illusion Reconstruction (VIR) dataset.** Each cell indicates the amount of retained voxels (i.e., voxels with noise ceiling signal-to-noise ratio (ncsnr) scores above 0.5) out of the total voxels, for a given subject and area. Because area V4 of VIR subject 4 did not have voxels with ncsnr above 0.5, for this subject and area we instead lowered the ncsnr threshold to 0.4.

	V1	V4
<b>Subject 1</b>	35 / 382 (9 %)	25 / 323 (8 %)
<b>Subject 2</b>	225 / 487 (46 %)	173 / 383 (45 %)
<b>Subject 3</b>	283 / 647 (44 %)	125 / 284 (44 %)
<b>Subject 4</b>	211 / 425 (50 %)	96 / 289 (33 %)
<b>Subject 5</b>	157 / 389 (40 %)	66 / 286 (23 %)
<b>Subject 6</b>	262 / 428 (61 %)	167 / 375 (45 %)

**Supplementary Table 4 | In vivo fMRI retained voxels for the univariate RNC experiment.** Each cell indicates the amount of retained voxels (i.e., voxels with noise ceiling signal-to-noise ratio (ncsnr) scores above 0.4) out of the total voxels, for a given subject and area.

	V1	V4
<b>Subject 1</b>	86 / 382 (23 %)	55 / 323 (17 %)
<b>Subject 2</b>	190 / 487 (39 %)	101 / 383 (26 %)
<b>Subject 3</b>	242 / 647 (37 %)	67 / 284 (24 %)
<b>Subject 4</b>	109 / 425 (26 %)	24 / 289 (8 %)
<b>Subject 5</b>	105 / 389 (27 %)	30 / 286 (10 %)
<b>Subject 6</b>	270 / 428 (63 %)	130 / 375 (35 %)

**Supplementary Table 5 | In vivo fMRI retained voxels for the multivariate RNC experiment.** Each cell indicates the amount of retained voxels (i.e., voxels with noise ceiling signal-to-noise ratio (ncsnr) scores above 0.4) out of the total voxels, for a given subject and area.



# References

1. Allen, E. J. *et al.* A massive 7T fMRI dataset to bridge cognitive neuroscience and artificial intelligence. *Nat. Neurosci.* **25**, 116–126 (2022).
2. Wu, M. C.-K., David, S. V. & Gallant, J. L. Complete Functional Characterization Of Sensory Neurons By System Identification. *Annu. Rev. Neurosci.* **29**, 477–505 (2006).
3. Gu, Z. *et al.* NeuroGen: Activation optimized image synthesis for discovery neuroscience. *NeuroImage* **247**, 118812 (2022).
4. Gifford, A. T., Cichy, R. M., Naselaris, T. & Kay, K. A 7T fMRI dataset of synthetic images for out-of-distribution modeling of vision. Preprint at <https://doi.org/10.48550/ARXIV.2503.06286> (2025).
5. Cheng, F. L. *et al.* Reconstructing visual illusory experiences from human brain activity. *Sci. Adv.* **9**, eadj3906 (2023).
6. Dosovitskiy, A. & Brox, T. Generating Images with Perceptual Similarity Metrics based on Deep Networks. in *Advances in Neural Information Processing Systems* vol. 29 (Curran Associates, Inc., 2016).
7. Xiao, W. & Kreiman, G. XDream: Finding preferred stimuli for visual neurons using generative networks and gradient-free optimization. *PLOS Comput. Biol.* **16**, e1007973 (2020).
8. Ponce, C. R. *et al.* Evolving Images for Visual Neurons Using a Deep Generative Network Reveals Coding Principles and Neuronal Preferences. *Cell* **177**, 999–1009.e10 (2019).
9. Kriegeskorte, N., Mur, M. & Bandettini, P. A. Representational similarity analysis - connecting the branches of systems neuroscience. *Front. Syst. Neurosci.* **2**, (2008).
10. Yamane, Y., Carlson, E. T., Bowman, K. C., Wang, Z. & Connor, C. E. A neural code for three-dimensional object shape in macaque inferotemporal cortex. *Nat. Neurosci.* **11**, 1352–1360 (2008).
11. Vaziri, S., Carlson, E. T., Wang, Z. & Connor, C. E. A Channel for 3D Environmental Shape in Anterior Inferotemporal Cortex. *Neuron* **84**, 55–62 (2014).